Stability Studies of Inviscid Shallow Water Flows on a Sphere

A Thesis

Submitted to the
Tata Institute of Fundamental Research, Mumbai
Subject Board of Physics
for the degree of Doctor of Philosophy

by

Mukesh Singh Raghav

International Centre for Theoretical Sciences
Tata Institute of Fundamental Research

Final Version Submitted in April, 2026

DECLARATION

This thesis is a presentation of my original research work. Wherever contributions of others are involved, every effort is made to indicate this clearly, with due reference to the literature, and acknowledgment of collaborative research and discussions.

The work was done under the guidance of Professor Amit Apte until 15/09/2021 and then Professor Rama Govindarajan, at the International Centre for Theoretical Sciences Tata Institute of Fundamental Research, Bengaluru. Prof. Amit Apte served as co-supervisor.

Mukesh Raghav
Date: March 31, 2026

In my capacity as supervisor of the candidate's thesis, I certify that the above statements are true to the best of my knowledge.

Prof. Rama Govindarajan
Date: March 31, 2026

Acknowledgments

First and foremost, I express my deepest gratitude to my advisors, Prof. Rama Govindarajan and Prof. Amit Apte, for their constant encouragement and support throughout my research. I am profoundly grateful for their remarkable patience and for the intellectual freedom they provided. Beyond academic mentorship, they consistently stood up for me both personally and professionally whenever I needed their help, for which I remain deeply thankful.

I sincerely thank my collaborator, Sharath Jose, whose contributions have been invaluable at every stage of this work. From shaping ideas to teaching me tools, numerical implementation and writing, his involvement has been indispensable. He proved to be a major source of support during my periods of mental block, always motivating me to persevere and complete what I had started.

I would like to thank Joy Monteiro and Suhas for several insightful and stimulating discussions that enriched my understanding of the subject. I am also grateful to Prof. Jai Sukhatme for his crucial insights and for sharing codes that formed an important part of my analysis.

I am thankful to my friends Rahul, Pushkal, Sumith, Chandan, and Ganga for making my stay at ICTS both enjoyable and memorable. I am thankful to Mridul and Akarshit for long conversations which were helpful during my tough days.

The administrative staff at ICTS deserve special appreciation for their exceptional efficiency and helpfulness. I thank Jeeva and Madhulika for promptly clarifying a wide range of administrative queries throughout my stay. Irshad and Prashant were always there to resolve numerous IT-related issues that I faced. I am thankful to Basavaraj for his incredible support in any transport related request. I also acknowledge the cleaning, security, sports complex, and canteen staff at ICTS, whose dedicated service made everyday life comfortable and seamless.

My interest in physics developed from the inspiring teachings of Mr. Nitin Vijay during my IIT-JEE preparation, and I gratefully acknowledge his influence. I also thank Prof. Naseer Iqbal for inviting me to the University of Kashmir and

introducing me to inspiring people in academia.

Finally, I express my deepest gratitude to my family for their unconditional love and support. My father has always encouraged me to dream big and work hard, my mother has celebrated even the smallest milestones with immense pride and joy, and my sisters, particularly Meenakshi, has been a constant, silent source of strength. I dedicate this thesis to them. I also dedicate this thesis to my wife, Sakshi, for her infinite affection, understanding, and unwavering support. She has been a constant source of motivation and encouragement, while always providing honest and thoughtful criticism throughout this journey.

Publications

1. MS. Raghav, S. Jose, A. Apte, R. Govindarajan *Effects of equatorially-confined shear flow on MRG and Rossby waves*, *Dynam. Atmos. Oceans* **100** (2022) 101331.

   MS. Raghav, S. Jose, A. Apte, R. Govindarajan. Corrigendum to *Effects of equatorially-confined shear flow on MRG and Rossby waves*, *Dynam. Atmos. Oceans* (2024) 101499.

2. MS. Raghav, S. Jose, A. Apte, R. Govindarajan *Non-normal growth in inviscid Shallow Water equations in the absence of mean shear flow*, Manuscript in preparation, to be submitted soon.

Contents

0 Abstract **1**

1 Introduction **5**

1.1 Motivation 5

1.2 Organisation of thesis and summary of results 11

2 Modal Analysis **15**

2.1 Introduction 15

2.2 Problem formulation 18

2.2.1 Governing equations 18

2.2.2 Base Flow 20

2.2.3 Linearised spherical and β-plane systems 22

2.3 Weak Shear: neutral waves 24

2.3.1 Spectra 24

2.3.2 Eigenfunctions 27

2.4 Strong Shear 33

2.5 Effects of varying equivalent depth H_0 40

2.6 Stability analysis of Mexican hat profiles 42

2.7 Summary and discussion 44

3 Non-modal Analysis **47**

3.1 Introduction 47

3.2 Optimisation procedure 50

3.3 The eigenfunctions 52

3.4 Perturbations comprising two modes 53

3.5 Perturbations constructed from more than two modes 60

3.6 Conclusion 65

4 Nonlinear Analysis **67**
4.1 Description of the system and framework 67
4.2 Nonlinear Evolution of optimal initial conditions 68
4.3 Summary and Conclusion 73

5 Conclusion **75**
5.1 Limitations and Future directions 77

A Eigenvalue analysis - Numerical Method and Validation **79**

B Perturbation zonal velocity and geopotential **83**
B.0.1 Spherical coordinate system 83
B.0.2 β-plane system 84

C Nonlinear analysis - Numerical Method and Validation **85**

Bibliography **89**

Chapter 0

Abstract

Understanding the dynamics of equatorial waves is central to studying tropical variability and the dynamical processes governing large-scale atmospheric flow. While the rotating shallow water equations (RSWE) provide a canonical framework for studying these processes, much of the analysis in the tropics relies on the equatorial β-plane approximation under which, the dynamics near the equator is assumed to be well described. This thesis revisits that assumption by systematically comparing the stability and transient behaviour of equatorial waves in RSWE under the β-plane and full spherical system.

Two complementary problems are addressed in this thesis. The first part focuses on the effects of equatorially confined zonal shear flows on the modal characteristics of tropical waves under the β-plane approximation and on the full sphere. In this modal analysis, mean flows representing equatorial easterlies (EE) and westerlies (EW) are modelled using Gaussian jets restricted to small latitudes. Even in this equatorially confined setting, where the β-plane approximation is traditionally assumed to be reliable, substantial differences emerge between the β-plane and spherical systems. At low Froude number, mixed Rossby-gravity (MRG) and Rossby modes show the strongest sensitivity to shear, particularly at higher zonal wavenumbers. These modes undergo significant changes in phase speed and meridional trapping. The disturbances are more confined in EE than in EW. The relative confinement between the β-plane and sphere is wavenumber-dependent. While the β-plane predicts stronger equatorial trapping at small wavenumbers, the modes on sphere are found to be more trapped at larger wavenumbers. At high wavenumber, waves in EE become nearly non-dispersive with constant phase speed, whereas in EW the phase speeds of successive meridional modes cluster closely together. These modifications alter the structure of eigenfunctions, including the splitting of the

classical equatorial vortex associated with even meridional mode numbers into two off-equatorial vortices at sufficiently large wavenumber. Such structural transitions may be relevant for interpreting observed mesoscale Rossby disturbances in westerly flow. When the mean flow strength is increased, further discrepancies between the β-plane and spherical systems arise. The β-plane dispersion curves develop additional branches absent from the spherical spectrum, raising concerns about the physical validity of these modes. More critically, the β-plane system becomes unstable for both EE and EW, supporting exponentially growing disturbances with propagation directions tied to the background flow. In sharp contrast, the full spherical system remains neutrally stable for all configurations considered. The instabilities on the β-plane occur primarily at synoptic scales ($\lambda \sim 2500$,km), scales that are often but inappropriately analysed using this approximation. These results demonstrate that the spherical geometry is essential for correctly assessing stability, even when the mean flow is confined very close to the equator.

The second part of the thesis investigates non-normal growth in the zero-mean-flow RSWE. On the β-plane, the linearised operator is normal, eliminating any possibility of transient amplification. This reveals a fundamental limitation of the approximation that persists even in the absence of shear. On the sphere, however, the governing operator is non-normal, allowing perturbations to experience significant finite-time growth despite all eigenmodes being neutrally stable. The Lamb parameter, which depends on the equivalent depth of the shallow layer, controls the degree of non-normality and provides an upper bound on the attainable growth. Optimal perturbations are constructed using singular value decomposition from linear combinations of Kelvin, MRG, Rossby, eastward inertio-gravity (EIG) and westward inertio-gravity (WIG) eigenmodes. At high wavenumber, interactions between counter-propagating modes, particularly EIG-WIG pairs are sufficient to reproduce the dominant transient amplification. At lower wavenumbers, additional modes are needed to capture the dynamics, with four-mode perturbations producing growth comparable to that seen at large wavenumbers. In all cases, the initial perturbations exhibit weak geopotential anomalies, but the subsequent amplification is dominated by the rapid growth of the geopotential field, closely tied to the underlying non-normal growth.

The thesis further examines the nonlinear evolution of optimal initial conditions

identified in the non-modal analysis, in order to assess the robustness of non-normal growth at finite amplitude. For sufficiently small but finite perturbation amplitudes, the early-time evolution of the perturbations closely follows linear predictions. As the perturbation amplitude increases, nonlinear interactions progressively alter the dynamics. The duration over which linear theory remains valid shortens, the maximum achievable gain is reduced relative to the linear case, and the periodic oscillations in perturbation growth weaken over time. Additionally, compared to the linear case, both the geopotential and associated circulation extend to larger latitudes.

The thesis demonstrates that spherical geometry alone generates substantial non-modal amplification, independent of shear, and that this behaviour cannot be captured by the β-plane approximation. Additionally, the nonlinear interactions are shown to regulate the transient amplification initiated by non-normality in the linear regime. Combined with the modal analysis, these results highlight the need to employ the full spherical system in studying both the stability properties and the transient growth of equatorial waves.

Chapter 1

Introduction

1.1 Motivation

Geophysical flows, such as atmospheric and oceanic circulation are intrinsically complex, multiscale, and high-dimensional forming some of the most intricate dynamical systems encountered in nature. Owing to the interplay between rotation, stratification, and forcing, these flows present an enormous hierarchy of a wide range of interacting motions evolving across diverse spatio-temporal scales. These scales range from slowly varying planetary waves spanning the globe over seasons and years, to mesoscale and synoptic disturbances spanning hundreds of kilometers over days, down to convective and turbulent processes active on kilometer and sub-kilometer scales evolving within hours or minutes [1, 2]. Crucially, many of these processes are nonlinear having small perturbations growing and interacting across different scales. Such multiscale coupling renders these systems highly sensitive to initial conditions with small scale perturbations cascading across scales [3] The small scale processes are often unresolved and the parametrization of these subgrid-scale processes leads to model error and uncertainty, limiting the horizon of predictability [4]

Within the rich tapestry of geophysical motion, the tropics play a particularly vital role in the dynamics of the global atmosphere and oceans. The tropics receive the bulk of incoming solar radiation, making them the primary energy source for the global circulation. Convection in this region drives large-scale overturning circulations such as the Hadley and Walker cells, which act as conduits for the redistribution of heat and momentum across latitudes [1]. Perturbations in tropical convection can organize into planetary-scale disturbances, modulating circulation far beyond their region of origin. Variability in tropical regions exerts profound influence on both local and global scales, affecting the onset, strength and seasonal cycle

of monsoonal circulations, interannual oscillations such as the El Niño–Southern Oscillation (ENSO) which are a coupled ocean–atmosphere phenomenon characterized by irregular warm (El Niño) and cool (La Niña) phases in the equatorial Pacific, and intraseasonal modes such as the Madden–Julian Oscillation (MJO) [5]. Disturbances in the tropics excite teleconnections that frequently project onto extratropical circulations, modulating storm tracks, jet streams, and even midlatitude predictability [6]. Hence, an improved dynamical understanding of tropical variability is crucial for enhanced climate and weather prediction.

A defining characteristic of atmospheric and oceanic processes is the enormous disparity between their lateral and radial scales. In the atmosphere, the vertical (or radial) extent of dynamically active layers is comparatively shallow—on the order of $10 - 15$ km for the troposphere, with the bulk of deep convection typically confined to the lowest $5 - 10$ km [2]. By contrast, the horizontal (lateral) scales of tropical circulations can span thousands of kilometers, as exemplified by planetary-scale equatorial waves, MJO, the Walker circulation, and monsoon systems [1]. A similar scale disparity is observed in the ocean, where the mixed layer and thermocline extend only a few hundred meters vertically, yet horizontal phenomena such as the equatorial currents and ENSO-related sea surface temperature anomalies extend across the entire Pacific basin [7]. In the tropics, this disparity has profound consequences for predictability and modeling. The confinement of convective heating to a thin vertical column can generate large-scale horizontal responses in the form of equatorial waves, teleconnections, or monsoonal circulations [8, 9]. This lateral–radial disparity allows the geophysical flows to be approximately treated as a shallow layer, licensing elimination of certain spatial and temporal scales from the governing equations. Such asymptotic reductions of the primitive equations lead naturally to the construction of quasi two-dimensional models, where vertical structure is either parameterized or projected onto a limited set of modes, while the primary dynamics unfold in the horizontal plane [1]. These reduced models render the analysis more tractable providing a scope for analytical or semi-analytical treatments of such complex dynamical phenomena.

At the heart of these simplifications is the shallow water approximation, where a single homogeneous shallow layer of fluid subject to rotation is assumed to be in a state of hydrostatic balance, with constant density across the layer depth. In-

corporating this approximation, Rotating Shallow Water Equations(RSWE) are the canonical representative of such reduced models, which allow for a consideration of the effects of rotation in a simple framework without the complicating effects of stratification. These equations capture the essential balance between pressure gradient and Coriolis forces i.e. geostrophic balance, which is observed in large-scale, extratropical circulation of the atmosphere [1]. Additionally large-scale geophysical structures are primarily shaped by the distribution and rearrangement of Potential Vorticity, which is conserved in these equations. As a result, though idealized, these equations are capable of reproducing a wide array of flow phenomena of immediate relevance to the tropics. The RSWE have historically been studied on a tangential plane at a particular latitude under the f-plane or β-plane approximations. On the f-plane, length scale of interest are such that the Coriolis parameter can be assumed constant by ignoring its variations with latitude. On the β-plane, the linear variation of f with latitude is retained to capture the curvature of the Earth [2]. These approximations permit local studies of geophysical flows, facilitating insights into midlatitude and equatorial dynamics. A landmark advance came with the seminal work of Matsuno [8] on the equatorial β-plane where the Coriolis parameter is expanded about the equator. He showed that this geometry supports a set of wave solutions to the linearized RSWE, providing the first systematic classification of these modes, including Kelvin waves, Rossby waves, mixed Rossby–gravity (MRG) waves, and eastward and westward inertio-gravity (EIG, WIG) waves. It was shown that the low frequency waves are equatorially trapped such that these waves have appreciable amplitude only in the narrow belt along the equator. More formally, Lindzen [10] derived the shallow water equations on β-plane from the primitive equations on the sphere and obtained general solution of the system under equatorial and midlatitude β-plane. Their analysis interpreted equivalent depth as a measure of the vertical propagation characteristics of the modes and provided their approximate expressions. The vertical structure, and its relationship to horizontal structure was clearly explained in their study. Subsequent observations established the presence of these waves in the atmosphere and the ocean [11–16]. These equatorial waves are known to have notable effects on the dynamics of the atmosphere and the ocean [1, 17]. For instance, the modification of the zonally symmetric flow in the stratosphere is intimately linked to the MRG wave [18]. Further, Kelvin waves

are known to generate an upward flux of westerly momentum, accounting for westerly acceleration associated with the quasi-biennial oscillation (QBO) [13] which is a downward-propagating signal of alternating easterly and westerly zonal winds in the equatorial stratosphere. In addition to revealing the natural modes of variability supported by the tropical atmosphere, these solutions provided explicit dispersion relations and meridional structures, making them directly comparable with observations. Most notably, in the global space–time spectrum of tropical variability identifying the dominant spectral peaks of equatorial waves in the real atmosphere, Wheeler & Kiladis [19] confirmed the presence of equatorial wave signals demonstrating a remarkable agreement with Matsuno's solutions. Their success highlighted the power of simplified quasi-two-dimensional theories to capture essential aspects of tropical variability and guide both theoretical and observational advances in the field.

Apart from approximating the sphere by a β-plane, another key idealisation in Matsuno's formulation is the absence of a background mean flow. Rarely quiescent, the tropical atmosphere is dominated by the robust zonal flows such as easterly trade winds or westerly wind bursts associated with ENSO, and the alternating jets of the stratospheric QBO. These flows conspire to create background currents with significant vertical and meridional shear. Waves propagating through such sheared environments experience a rich suite of modifications. There have been numerous modelling and observational studies that explored the role of background circulation and wind shear in modulating the equatorial waves [20–26]. Background shear induces Doppler shifting of wave frequencies which alters their phase speed and dispersion properties modulating the characteristics of wave propagation [27, 28]. Critical layers can exist in the presence of mean flow, where the phase speed matches the background flow velocity and disturbance energy is absorbed [29]. More recently, Maho et al. [25, 26] studied the interaction between off-equatorial jet and spherical MRG waves and their role in scale selection. Mean shear flow can cause the accumulation of wave energy in specific latitude bands which facilitates the transfer of momentum to higher latitudes, modifying the equatorial trapping, which is the degree to which equatorially waves are confined in latitude and changing their ability to communicate with the extratropics [30–34]. Additionally, under certain favorable configurations, background shear can destabilize modes, giving rise to barotropic

or baroclinic instabilities that convert mean kinetic or available potential energy into organized wave disturbances [35, 36]. While capturing the Doppler shifting, instability, and critical level absorption, the latitude-dependent structure of zonal flows was ignored in these studies. As a result of this, they could not properly address the modulation of equatorial trapping of the waves in the presence of realistic shear profiles. Zhang & Webster [37] provided the first systematic treatment of the effects of shear flow on the full spectrum of equatorially trapped modes within a consistent framework of RSWE on equatorial β-plane. They demonstrated that shear fundamentally alters equatorial trapping, allowing energy leakage to higher latitudes or enhanced trapping depending on the flow configuration. They studied the case of a mid-latitude jet in addition to equatorial easterly (EE) or westerly (EW) jets. While having realistic meridional structure, these profiles extend well beyond the equatorial region. This brings the use of β-plane approximation in their study into question. Additionaly their analysis was performed for a limited range of small wavenumbers.

While the β-plane approximation often yields good insights by isolating the leading-order dynamics, it must be appreciated that the spherical geometry of the Earth can introduce added complexities to the dynamics. Building on the earliest demonstration of solution of Laplace Tidal equations in terms of Hough functions [38], Longuet-Higgins [39] carried out the first complete and rigorous classification of the eigenfunctions of these equations on sphere. The equatorial modes such as Kelvin, Rossby, inertia–gravity, and mixed Rossby–gravity were highlighted to be the part of a global discrete spectrum of bounded and orthogonal Hough modes. Subsequent studies recognised the influence of sphericity on equatorial disturbances and devised normal mode initialization techniques exploiting such waves [40, 41]. Castanheira et al. [42] and Zagar et al. [43] recognised the importance of spherical waves and devised spherical harmonics (as opposed to cylindrical parabolic function proposed by Yang et al. [28]) to identify the equatorial waves. More recently, Paldor *et al.* [44] demonstrated the critical dependence of the character of shallow water wave solutions on the rotation regime. In the weak-rotation limit, the spherical solutions are found to be accurate across a broad range of zonal wavenumbers (k), whereas in the strong-rotation limit, the solutions remain robust only for small k. Importantly, the Kelvin wave, appearing as a distinct non-dispersive solution in

the β-plane framework is found to be embedded in the broader spherical spectrum as the lowest-order eastward-propagating inertio-gravity (EIG) mode [45]. Further, Paldor *et al.* [46] investigated the stability of equatorial jets within the full shallow water equations on the sphere in contrast with commonly used approximate theories such non-divergent (ND) and quasi-geostrophic (QG) frameworks. The full shallow water equations consistently predict smaller growth rates compared to the growth captured in approximate models emphasizing the importance of retaining the full dynamical complexity of the system. However, the jets considered for their analysis were particularly strong with speeds substantially larger than those typically observed in the Earth's tropical atmosphere. This raises the question of behaviour of instabilities in weaker shear flows which represent the observed tropical variability more suitably. Additionally, being primarily focused on the growth rates of unstable modes, the spatial structures of perturbations was not investigated.

Another important perspective in the study of equatorial wave dynamics arises from the theory of non-normal operators. The classical Matsuno formulation, based on a resting basic state, leads to a normal operator which admits a complete set of orthogonal modes. In this case, growth of disturbances is associated solely with the presence of unstable eigenfunctions. Departures from this idealised setting fundamentally change the properties of governing operator. In the presence of mean shear flows or spherical geometry, the linear shallow-water operator becomes non-normal whose eigenfunctions are no longer mutually orthogonal. As a result, even when all the eigenfuncations are individually stable, certain linear combinations of these modes can constructively interfere to produce substantial transient growth over finite timescales [47–49]. This transient growth can be of significance to equatorial dynamics if it occurs on timescales comparable to tropical variability. In such cases, modal analysis alone no longer captures the full range of possible dynamical behaviour, and non-modal tools are essential for understanding transient growth, interference between modes, and the amplification of small disturbances.

The central objective of such analyses is to identify the optimal initial perturbations or Singular vectors (SVs), which maximize energy amplification in a given norm over a finite optimization horizon. SVs have proved to be crucial in atmospheric predictability studies, forecast error estimation and identification of direction of initial uncertainty leading to largest forecast uncertainty [50]. Beyond these, non-modal

perturbations are capable of extracting energy from mean flow which may be projected on modal disturbances facilitating the excitation of persistent normal modes [51]. The non-modal waves were observed to exhibit growth rate and structures remarkably consistent with observed precursors to cyclogenesis [52]. Most studies of non-modal growth in the atmosphere have been carried out within the quasi-geostrophic (QG) framework. The QG framework is a reduced dynamical model obtained by expanding the primitive equations in small Rossby number, yielding a system that filters inertia–gravity waves and captures the slow, balanced evolution of large-scale rotational flow [1]. The QG approximation, while extremely useful for midlatitude dynamics, suppresses gravity-wave dynamics by assuming weak divergence, thereby excluding much of the rich equatorial variability captured by the rotating shallow water equations (RSWE). Despite its central role in identifying the major atmospheric wave types, the β-plane approximation has known limitations in modal analysis, where its neglect of spherical geometry can lead to discrepancies in the structure and dispersion of equatorial modes. Compounding to that, the governing operator on β-plane, linearized about a state of zero mean flow is normal suggesting that all perturbation growth is entirely dictated by the eigenvalue spectrum [8]. In contrast, the corresponding operator on the full sphere is non-normal, allowing substantial transient amplification of certain linear combinations of otherwise spectrally stable modes. This highlights that absence of non-normal growth under the β-plane approximation is not a fundamental property of equatorial waves, but rather an artifact of the approximation. However, the sphere provides a natural setting for finite-time growth phenomena, revealing mechanisms of energy amplification that are entirely inaccessible to β-plane dynamics. This further strengthens the importance of using the full spherical framework when studying equatorial dynamics and wave–shear interactions.

1.2 Organisation of thesis and summary of results

These limitations underscore that the systematic influence of shear on the fundamental modal properties of equatorial waves—such as their eigenfrequencies, dispersion characteristics, and the spatial confinement near the equator (equatorial trapping)—has not been fully characterized. As a result, a comprehensive under-

standing of the effects of shear on equatorial waves remains elusive. Additionally, the applicability of the β-plane approximation to the rotating shallow water equations (RSWE) in the presence of shear has not been rigorously assessed. While the β-plane provides a tractable local framework, it misses global effects associated with spherical geometry, particularly for low-frequency modes like Rossby and MRG waves that are majorly influenced by curvature and extratropical latitudes. Motivated by these gaps, we set out to systematically explore the role of equatorially confined shear flows on the properties of individual eigenmodes describing equatorial waves (modal analysis) in chapter 2 of present thesis. In particular, we contrast the behavior of eigenfrequencies and the meridional trapping of wave modes under equatorial easterly (EE) and equatorial westerly (EW) shear profiles with Gaussian profiles highly confined to small latitudes, examining both the β-plane and the full spherical system across a wide range of zonal wavenumbers. These shear configurations are routinely observed in the tropical atmosphere. Equatorial easterly shear is a defining feature of the QBO in the lower stratosphere, where it strongly modulates wave propagation and momentum fluxes. Conversely, equatorial westerly shear arises during westerly wind bursts associated with the MJO and ENSO onset phases, where it influences the excitation and propagation of Kelvin waves and eastward inertio-gravity modes. By analyzing both EE and EW configurations, it is investigated how the direction and magnitude of shear selectively modify different branches of the equatorial wave spectrum. The main results are as follows:

- Slowly propagating MRG and ER modes are most affected in the presence of mean shear. With shear, the deviations in both the meridional span of the modes as well as their frequency are significant at large wavenumber (k).

- Both the long and short waves tend to become non-dispersive in EE and travel faster than in the zero mean flow case. In EW, frequency of modes for successive meridional number (n, defined in chapter 2) approach close to each other and travel with a smaller phase speed. The difference in frequency as obtained in the β-plane approximation and on the sphere is insignificant.

- Compared to zero mean flow, the short waves are more equatorially trapped in EE than in EW, i.e., their amplitudes become more strongly confined in EE than EW to a narrower latitudinal region around the equator. At large k,

contrary to the expectation of better agreement between β-plane and sphere, waves are found to be more trapped on the sphere than predicted by the β-plane approximation.

- In the presence of strong shear, the phase speeds are significantly larger in the β-plane system for all families of waves. Under the β-plane approximation, exponentially unstable modes can be excited, having negative (positive) phase speed in EE (EW). Strikingly, this flow is always neutrally stable with the full spherical system.

In chapter 3, the non-normal growth of perturbations to the zero mean shear equilibrium state of RSWE is explored. The non-normal behaviour of the system under the β-plane approximation is contrasted against that on the full sphere. The perturba tions are constructed by solving a finite-time optimisation problem in which the initial condition that yields the maximum possible growth of perturbation energy over a prescribed time interval is identified using singular value decomposition (SVD) method. These optimal initial conditions are represented as linear combinations of the eigenfunctions of the linearised spherical operator, including EIG, WIG, Kelvin, MRG, and Rossby modes.

Upon examining the perturbations comprising any two modes, we find those involving counter propagating modes experience significant non-normal growth. At mesoscales ($k \gtrsim 30$), which correspond to horizontal length scales of a few hundred kilometres on earth, 2-mode case sufficiently captures the significant non-normal growth and introducing more modes in the perturbation does not lead to any further increase in optimal gain or alter the temporal structure of the growth. On the other hand, at planetary to synoptic scales ($k \lesssim 20$), the 2-mode case predicts relatively moderate growth. Constructing non-modal perturbations using a greater number of modes (4 modes) leads to a higher growth, comparable to what is seen at higher k.

In chapter 4, a preliminary nonlinear analysis is presented investigating the nonlinear time evolution of the optimal perturbations obtained from the non-modal framework. It is aimed to evaluate how non-normal amplification persists at finite amplitudes. When the initial perturbations are small but nonzero, their short-time behaviour remains in close agreement with linear theory. As the amplitude is in-

creased, the time interval over which linear dynamics provide an accurate description becomes shorter accompanied by weakening of peak energy amplification relative to that observed in linear regime. Moreover, in contrast to the linear regime, the resulting geopotential and circulation fields exhibit a broader meridional extent, reaching higher latitudes.

Chapter 2

Modal Analysis

The work presented in this chapter has been published in *Dynamics of Atmospheres and Oceans* article [53] alongwith the corrigendum [54].

The development of the framework used in this chapter benefited substantially from discussions and guidance provided by Sharath Jose. He introduced the references that informed the construction of latitudinal grids with enhanced resolution near the equator, both on the β-plane and the sphere. In addition, he supplied a diagnostic routine to determine the number of sign changes of a field along the meridional direction-a key tool that enabled reliable identification and labelling of the modal indices (n_u,n_v, n_h), which was essential for interpreting structural changes in the eigenfunctions in the presence of shear. He further recognised the link between the zeros of the height and zonal velocity fields and the extrema of the meridional velocity, and proposed quantitative measures used in this chapter, including the localisation metrics and the definition of frequency change. These contributions informed both the interpretation and the computational procedures employed in the results.

2.1 Introduction

The theory of equatorial waves is crucial for an understanding of equatorial dynamics in geophysical systems [10, 55, 56]. In a seminal work, Matsuno [8] derived analytical solutions to the rotating shallow water equations (RSWE) on an equatorial β-plane linearised about a steady state with zero flow. Matsuno's analysis identified different families of waves – eastward inertio-gravity (EIG), westward inertio-gravity (WIG), mixed Rossby gravity (MRG), Rossby and Kelvin waves. Subsequent observations established the presence of these waves in the atmosphere and the ocean [11–14, 16].

These equatorial waves are known to have notable effects on the dynamics of the atmosphere and the ocean [1, 17]. For instance, the modification of the zonally symmetric flow in the stratosphere is intimately linked to the MRG wave [18]. Further, Kelvin waves are known to generate an upward flux of westerly momentum, accounting for westerly acceleration associated with the QBO [13]. Despite the agreement of the prominent peaks in the space-time spectrum of the tropical cloudiness [19] and the rainfall [57], calculated over the equatorial band (15S-15N), with theoretically calculated dispersion curves, there were some important limitations in Matsuno's theory of equatorial waves.

The Matsuno theory is based on zero mean flow, but meridionally averaged climatological zonal flow shows significant variation with latitude and presence of longitudinal shear. Thus a natural question is to understand how the equatorial waves are modified in the presence of such shear flows - this is one of main aims of the present study. We first review some of the main results of previous studies in this direction. Beyond the primary effects of Doppler shifting [28], mean flow is shown to have non-trivial effects on the properties of equatorial waves and vice versa [58, 59]. Critical layers, where the phase speed equals the mean flow velocity and disturbance energy is absorbed, can exist [60]. The longitudinal variation of the mean flow can result in regions where wave energy can be accumulated or depleted; here, wave trains extending beyond the equatorial regions can allow for energy exchange with higher latitudes [30]. MRG and Rossby modes show a higher degree of trapping in the presence of equatorial easterly than in a westerly mean flow [37].

While the β-plane approximation often yields good insights, it must be appreciated that the dynamics on the sphere can assume greater complexity [38]. In a landmark work, [39] described in great detail the numerically computed eigenfunctions on the sphere for the complete range of ϵ (a parameter characterising rotation that we define in section 2.2.1), and further discussed the asymptotic forms of these eigenfunctions in various limits of ϵ that revealed interesting properties of gravity, planetary and Kelvin waves. Recent work [44] showed the solutions in the weak rotation regime to be suitable for most wavenumbers while the solutions in the strong rotation regime seem to work well for only small wavenumbers. The Kelvin mode, which was identified as a distinct mode in the β-plane configuration, was found to be the lowest order EIG mode in the spherical system [45]. In the presence of strong

polar and equatorial jets, [46] found the shallow layer depth to be a crucial factor for the growth rates of modal instabilities.

The following two comprehensive studies of stability of RSWE with a longitudinal shear flow are most relevant to the present chapter: [37] using the β-plane approximation, and [46] using the full spherical system. [37] studied the case of a mid-latitude jet in addition to equatorial easterly (EE) or westerly (EW) jets. These profiles have features of a realistic flow, but they extend beyond the equatorial region. So in principle, such flows should be studied in a complete spherical system rather than under the β-plane approximation. Also, this early study was restricted to small wavenumbers. As will be apparent in our study, the effects of shear flow are significant for large wavenumbers, which is one of the main contributions of our work.

[46] studied the stability of equatorial jets in the spherical system. Their motivation was to compare the instabilities obtained from approximate theories – non-divergent (ND) and quasi-geostrophic (QG) – to those from the full shallow water equations. They showed that the full equations consistently predict smaller disturbance growth rates. We note that their flow speeds were very large, whereas we study weaker shears which occur more commonly in the atmosphere. We note further that their work was primarily interested in the growth rates of unstable modes, and did not examine the spatial structure of the perturbations, which is another major contribution of the present chapter.

With this background in mind, we now review the salient features and main results of this chapter. We study how a mean flow with shear modifies the spatial structures of the waves. Our study is on a Gaussian mean flow profile restricted to small latitudes. We show (section 2.3) that especially for large zonal wavenumbers, the spatial structure of the disturbance modes as well as the dispersion relation are both significantly different from the case of zero mean flow. Another objective of the present study is to ask whether the β-plane system can provide a qualitatively reasonable approximation, at least for a mean flow that is confined very close to the equator. We show, surprisingly, that this is not the case. In fact, the β-plane approximation shows branches of exponentially growing perturbations whereas there are no instabilities for the full spherical system. Moreover, the disturbance eigenmodes are not confined to small latitudes. Both these results (section 2.4) bring into

question the suitability of the β-plane approximation.

The layout of the chapter is as follows. The basic equations in the β-plane and the spherical system with relevant approximations, the details of the mean flow whose stability is studied and the numerical method used to get the stability results are presented in section 2.2. In section 2.3, the effects of weak mean shear flow on the propagation and the structure of neutral waves are discussed. Section 2.4 considers the regime where the β-plane system yields unstable modes. Finally, the results are summarised and their implications are discussed in section 2.7.

2.2 Problem formulation

2.2.1 Governing equations

The atmosphere and the ocean are predominantly in a state of hydrostatic balance with the spatial scales in the horizontal direction being significantly larger than those in the radial direction. The rotating shallow water equations (RSWE) on a sphere, introduced in section 2.2.1, are thus a natural framework in which a wide range of geophysical phenomena are studied [1]. Depending on the region of interest, these equations could be simplified using a planar approximation, such as the f-plane or the β-plane. The latter, where the Coriolis force is approximated as varying linearly with the latitude, are introduced in section 2.2.1 and are often used to study equatorial dynamics. The spherical and β-plane RWSE linearised around a zonally averaged mean flow, as specified in section 2.2.2, are obtained in section 2.2.3.

Throughout the thesis, H_0 indicates the equivalent depth, which is related to the measure of the static stability(N^2) and the wavelength of vertical modes of atmosphere (eq. 14 in [55]). It thus provides a link between the horizontal and the vertical dynamics. While the mean depth of the shallow layer seems like a natural physical choice for the mean height field, the corresponding gravity wave speed is much larger than that observed in the atmosphere. For most of our analysis, we choose $H_0 = 100$ m for our study, which lies between the shallower depth ($\sim$12–50 m) displayed by convectively coupled equatorial waves (CCEW) and a larger depth of $\sim$200 m corresponding to the peak projection response of deep convective heating [19, 61, 62]. In 2.5, we also show some additional results with different values of H_0. By studying different for different values of H_0, we analyse the behaviour of

system in different range of vertical wavelengths of atmosphere (refer to table 1 in [55] for details).

Equations in the spherical system

In the spherical coordinates, RSWE take the following form [63]:

$$\frac{\partial u_s^*}{\partial t^*} = 2\Omega \sin\theta v_s^* - \frac{u_s^*}{R\cos\theta}\frac{\partial u_s^*}{\partial \phi} - \frac{v_s^*}{R}\frac{\partial u_s^*}{\partial \theta} + \frac{v_s^* u_s^* \tan\theta}{R} - \frac{g}{R\cos\theta}\frac{\partial h_s^*}{\partial \phi} , \tag{2.1a}$$

$$\frac{\partial v_s^*}{\partial t^*} = -2\Omega \sin\theta u_s^* - \frac{u_s^*}{R\cos\theta}\frac{\partial v_s^*}{\partial \phi} - \frac{v_s^*}{R}\frac{\partial v_s^*}{\partial \theta} - \frac{u_s^{*2}\tan\theta}{R} - \frac{g}{R}\frac{\partial h_s^*}{\partial \theta} , \tag{2.1b}$$

$$\frac{\partial h_s^*}{\partial t^*} = -\frac{u_s^*}{R\cos\theta}\frac{\partial h_s^*}{\partial \phi} - \frac{v_s^*}{R}\frac{\partial h_s^*}{\partial \theta} - \frac{h_s^*}{R\cos\theta}\left(\frac{\partial u_s^*}{\partial \phi} + \frac{\partial}{\partial \theta}(v_s^*\cos\theta)\right) . \tag{2.1c}$$

Here, u_s^* and v_s^* are the dimensional zonal and meridional velocity components respectively and h_s^* is the height of the shallow layer. $\Omega = 2\pi/86400$ s^{-1} and $R = 6371.22$ km are the angular speed and the radius of the earth respectively, $g = 9.8$ m/s is the acceleration due to gravity, $\theta \in [-\pi/2, \pi/2]$ is the latitude, and $\phi \in [0, 2\pi]$ is the longitude. Defining the timescale $T_s \equiv 1/(2\Omega)$, the non-dimensional variables in spherical coordinates are defined as

$$(u_s, v_s) = \frac{T_s}{R}(u_s^*, v_s^*) , \quad h_s = \frac{h_s^*}{H_0}, \quad t_s = \frac{t^*}{T_s} . \tag{2.2}$$

The resulting non-dimensional system of equations have the same form as equation (2.1) (formally with $R = 1$, $2\Omega = 1$, and $g = 1/\epsilon$) with a single non-dimensional number, the Lamb parameter

$$\epsilon \equiv \frac{(2\Omega R)^2}{gH_0} . \tag{2.3}$$

With $H_0 = 100$ m, note that $\epsilon = 880.44$. In oceans, the typical equivalent depths are relatively smaller, which results in even larger values of ϵ.

Equations in the equatorial β-plane

The RSWE on the equatorial β-plane take the following form [1]:

$$\frac{\partial u_\beta^*}{\partial t^*} + u_\beta^* \frac{\partial u_\beta^*}{\partial x^*} + v_\beta^* \frac{\partial u_\beta^*}{\partial y^*} - \beta y^* v_\beta^* = -g \frac{\partial h_\beta^*}{\partial x^*} \ , \tag{2.4a}$$

$$\frac{\partial v_\beta^*}{\partial t^*} + u_\beta^* \frac{\partial v_\beta^*}{\partial x^*} + v_\beta^* \frac{\partial v_\beta^*}{\partial y^*} + \beta y^* u_\beta^* = -g \frac{\partial h_\beta^*}{\partial y^*} \ , \tag{2.4b}$$

$$\frac{\partial h_\beta^*}{\partial t^*} + u_\beta^* \frac{\partial h_\beta^*}{\partial x^*} + v_\beta^* \frac{\partial h_\beta^*}{\partial y^*} + h_\beta^* \left(\frac{\partial u_\beta^*}{\partial x^*} + \frac{\partial v_\beta^*}{\partial y^*} \right) = 0 \ , \tag{2.4c}$$

where $\beta = 2\Omega/R$ is the Coriolis parameter. We define the following reference time and length scales:

$$T_\beta \equiv \beta^{-1/2} (gH_0)^{-1/4}, \quad L_\beta \equiv \beta^{-1/2} (gH_0)^{1/4} \ . \tag{2.5}$$

L_β, known as the Rossby radius of deformation, is the fundamental length scale used in equatorial dynamics and signifies the length scale at which the rotational effects become comparable to the effects due to gravity waves [1]. The gravity wave speed $\sqrt{gH_0} = L_\beta / T_\beta$ is selected as the reference velocity scale. We can then move to a non-dimensional system with

$$(u_\beta, v_\beta) = \frac{1}{\sqrt{gH_0}} (u_\beta^*, v_\beta^*), \quad h_\beta = \frac{h_\beta^*}{H_0}, \quad t_\beta = \frac{t^*}{T_\beta}, \quad x = \frac{x^*}{L_\beta}, \quad y = \frac{y^*}{L_\beta} \ . \tag{2.6}$$

The non-dimensional β-plane RSWE take the same form as equation (2.4) (formally with $\beta = 1$, $g = 1$) with no non-dimensional parameters appearing in the equations themselves.

2.2.2 Base Flow

From climatologically averaged data, it is seen that the zonal mean flow is considerably stronger than the meridional flow [64]. Therefore, a significant number of studies have focused on the dynamics associated with purely zonal mean flows. In this study, we principally consider the stability of equatorial easterly (EE) and equatorial westerly (EW) flows (see figure 2.1) with Gaussian profiles. To show that the results are of a more generic nature, we also briefly discuss results for a mean

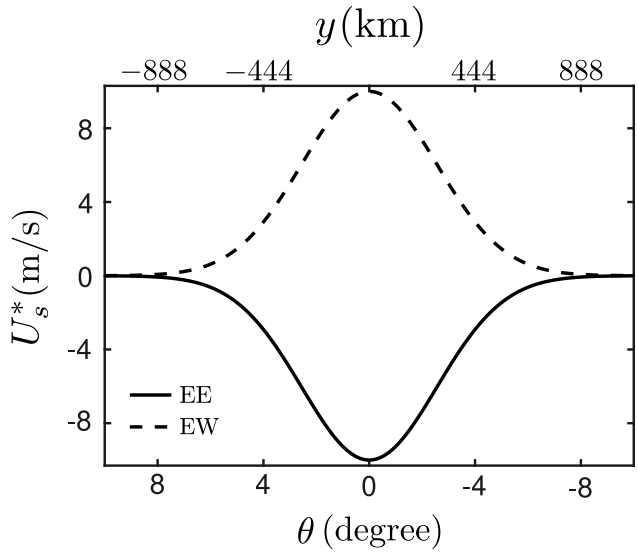

Figure 2.1: Profiles of equatorial easterly (EE) and equatorial westerly (EW) Gaussian mean flow $U_s^*(\theta)$, shown here for $\sigma_\theta = 0.0628$ rad (3.6°), $|U_0| = 10$ m/s, which corresponds to $|Ro| = 0.011$, i.e., $|Fr| = 0.32$.

flow with a Mexican hat profile in 2.6.

In nondimensional form, the base flow in the spherical system is chosen to be

$$U_s = Ro \exp\left(-\frac{\theta^2}{\sigma_\theta^2}\right) \ , \quad V_s = 0 \ , \tag{2.7}$$

where U_s and V_s are mean zonal and meridional velocity, respectively with negative or positive Ro being the EE and EW cases respectively. σ_θ sets the latitudinal span of the mean flow. The Rossby number Ro characterises the strength of the mean flow and it is related to the dimensional equatorial speed by

$$Ro = \frac{U_0}{2\Omega R} \ . \tag{2.8}$$

For the above flow, the depth of the shallow layer varies $\mathcal{H}_s(\theta) = 1 + H_s(\theta)$ in non-dimensional form. Note that H_s is the variation in the depth of the shallow layer that comes about due to the presence of a mean shear flow. In other words, $H_s = 0$ when $U_s = 0$. H_s is obtained by solving the geostrophic relation in spherical

coordinates:

$$\frac{\mathrm{d}H_s}{\mathrm{d}\theta} = -\epsilon(\sin\theta U_s + \tan\theta U_s^2) \ . \tag{2.9}$$

For the β-plane configuration, the same Gaussian (EE and EW) profiles are used for the mean flow. The distance along a fixed longitude is converted to planar distance in the β-plane as $y^* = R\theta$, which in the non-dimensional form is $y = R\theta/L_\beta$. The required non-dimensional base flow profile is then obtained using the velocity and length scales defined for the β-plane. Thus we get the mean velocity $U_\beta = Fr\ \exp(-y^2/\sigma_y^2)$, where $\sigma_y = R\sigma_\theta/L_\beta$ and the Froude number is defined by

$$Fr = Ro\sqrt{\epsilon} = \frac{U_0}{\sqrt{gH_0}} \ . \tag{2.10}$$

As with the spherical system, the depth of the shallow layer will vary as $\mathcal{H}_\beta(y) = 1 + H_\beta(y)$ in the non-dimensional form. Here, H_β is the variation of the shallow layer depth when there exists a mean flow ($Fr \neq 0$). H_β is obtained by solving

$$\frac{\mathrm{d}H_\beta}{\mathrm{d}y} = -yU_\beta \ . \tag{2.11}$$

For the base flow under consideration, $\mathcal{H}_\beta \approx 1$ (or equivalently, $\mathcal{H}_s \approx 1$). Zhang & Webster [37] and Bennett & Young [60] considered the variation of H_β in the advection term but neglected it in the flux term in the geopotential equation. However, for all of our calculations, we do not make apriori any such assumption and incorporate the variations of the mean equivalent depth due to the background shear flow in all the terms where they appear.

Throughout this chapter, we use $\sigma_y = 400$ km and correspondingly, $\sigma_\theta = 0.0628$ rad (3.6°).

2.2.3 Linearised spherical and β-plane systems

For linear stability analysis, we are interested in the asymptotic long-time evolution of perturbations to the base flow. The equations governing the perturbation evolution are rendered linear after neglecting terms that are quadratic in the perturbation quantities. In the spherical system, we invoke an ansatz where the perturbation

quantities assume the form $f_s'(\phi,\theta,t_s) = \tilde{f}_s(\theta)\exp(ik\phi - i\omega_s t_s)$ with k and ω_s being the zonal wavenumber and complex frequency respectively. The resulting eigenvalue problem is

$$-i\omega_s\tilde{\mathbf{q}}_\mathbf{s} = \mathbf{M}_\mathbf{s}\tilde{\mathbf{q}}_\mathbf{s}\ , \tag{2.12}$$

$$\text{where } \tilde{\mathbf{q}}_\mathbf{s} = \begin{bmatrix} \tilde{u}_s \\ \tilde{v}_s \\ \tilde{h}_s \end{bmatrix} \text{ and } \mathbf{M}_s = \begin{bmatrix} M_{uu} & M_{uv} & M_{uh} \\ M_{vu} & M_{vv} & M_{vh} \\ M_{hu} & M_{hv} & M_{hh} \end{bmatrix}\ . \tag{2.13}$$

The different operators in $\mathbf{M}_s$ are given below:

$$\left.\begin{aligned} &M_{uu} = M_{vv} = M_{hh} = \frac{-ikU_s}{\cos\theta}\ , \\ &M_{uv} = \sin\theta - D_\theta U_s + U_s\tan\theta \equiv \Omega_{as}\ , \quad M_{uh} = \frac{-ik}{\epsilon\cos\theta}\ , \\ &M_{vu} = -\sin\theta - 2U_s\tan\theta\ , \quad M_{vh} = -\frac{1}{\epsilon}D_\theta\ , \\ &M_{hu} = \frac{-ik\mathcal{H}_s}{\cos\theta}\ , \quad M_{hv} = \mathcal{H}_s\left(\tan\theta - D_\theta\right) - D_\theta\mathcal{H}_s\ . \end{aligned}\right\} \tag{2.14}$$

In the above, $D_\theta = \mathrm{d}/\mathrm{d}\theta$ and Ω_{as} is the absolute vorticity of the base flow. We impose homogeneous Dirichlet boundary conditions for the different components of the eigenfunction $\tilde{\mathbf{q}}_\mathbf{s}$; $\tilde{u}_s\left(\pm\pi/2\right) = \tilde{v}_s\left(\pm\pi/2\right) = \tilde{h}_s\left(\pm\pi/2\right) = 0$.

For the β-plane system, we again consider perturbations of the normal-mode form $f_\beta(x,y,t_\beta) = \tilde{f}_\beta(y)\exp(ik_\beta x - i\omega_\beta t_\beta)$ with k_β and ω_β being the non-dimensional zonal wavenumber and complex frequency respectively. With this ansatz, the resulting eigenvalue problem is:

$$-i\omega_\beta\tilde{\mathbf{q}}_\beta = \mathbf{M}_\beta\tilde{\mathbf{q}}_\beta\ , \tag{2.15}$$

$$\text{where } \tilde{\mathbf{q}}_\beta = \begin{bmatrix} \tilde{u}_\beta \\ \tilde{v}_\beta \\ \tilde{h}_\beta \end{bmatrix} \text{ and } \mathbf{M}_\beta = \begin{bmatrix} -ik_\beta U_\beta & \Omega_{a\beta} & -ik_\beta \\ -y & -ik_\beta U_\beta & -D_y \\ -ik_\beta\mathcal{H}_\beta & yU_\beta - \mathcal{H}_\beta D_y & -ik_\beta U_\beta \end{bmatrix}\ . \tag{2.16}$$

In the above, $D_y = \mathrm{d}/\mathrm{d}y$ and $\Omega_{a\beta}(\equiv y - D_y U_\beta)$ is the absolute vorticity of the base state. For boundary conditions, the perturbation fields are specified to go to zero as $y \to \pm\infty$.

In both the above cases, a modal (exponentially growing) instability exists when there is at least one eigenvalue with a positive imaginary part, i.e., when ω_s or ω_β has a positive imaginary part.

We also note that the wavenumbers in the spherical system k and in the β-plane system k_β are related by $k = R\cos\theta_0 k_\beta/L_\beta$, where θ_0 is the reference latitude about which the β-plane is defined. In the present study, as our β-plane is centred about the equator, we have $\theta_0 = 0$. This then gives us $k_\beta = L_\beta k/R$.

2.3 Weak Shear: neutral waves

Under low levels of shear, both the β-plane and spherical systems yield spectra consisting entirely of neutral modes. We demonstrate our findings on $|U_0| = 0.5$ m/s, which corresponds to $|Fr| = 0.02$.

2.3.1 Spectra

The configuration in the β-plane setting with no mean flow ($U_\beta = 0$) has been studied extensively [1, 65], and the non-dimensional eigenfrequencies are given by the dispersion relation [8]

$$\omega_\beta^2 - k_\beta^2 - \frac{k_\beta}{\omega_\beta} = n + \frac{1}{2}, \quad n = 0, 1, 2, \ldots. \tag{2.17}$$

In the above, n is the meridional mode number, which gives the number of zeros in the meridional velocity field along a given longitude. The cubic equation (2.17) yields three families of waves: EIG, WIG, and Rossby waves for $n \geq 1$. For $n = 0$, the WIG solution is unphysical and the Rossby wave solution is commonly known as the MRG mode. In addition to these modes, there exists the Kelvin mode with $\omega_\beta = k_\beta$ for $n = -1$.

On introducing mean shear, we find that the MRG and Rossby modes are significantly affected. In contrast, the effects of mean shear on the EIG, WIG and Kelvin modes are not as prominent. This is consistent with results from earlier studies (e.g. see [37]). Therefore, the subsequent discussion will focus on MRG and Rossby waves with the corresponding β-plane theory for zero mean flow case used as a template for comparison.

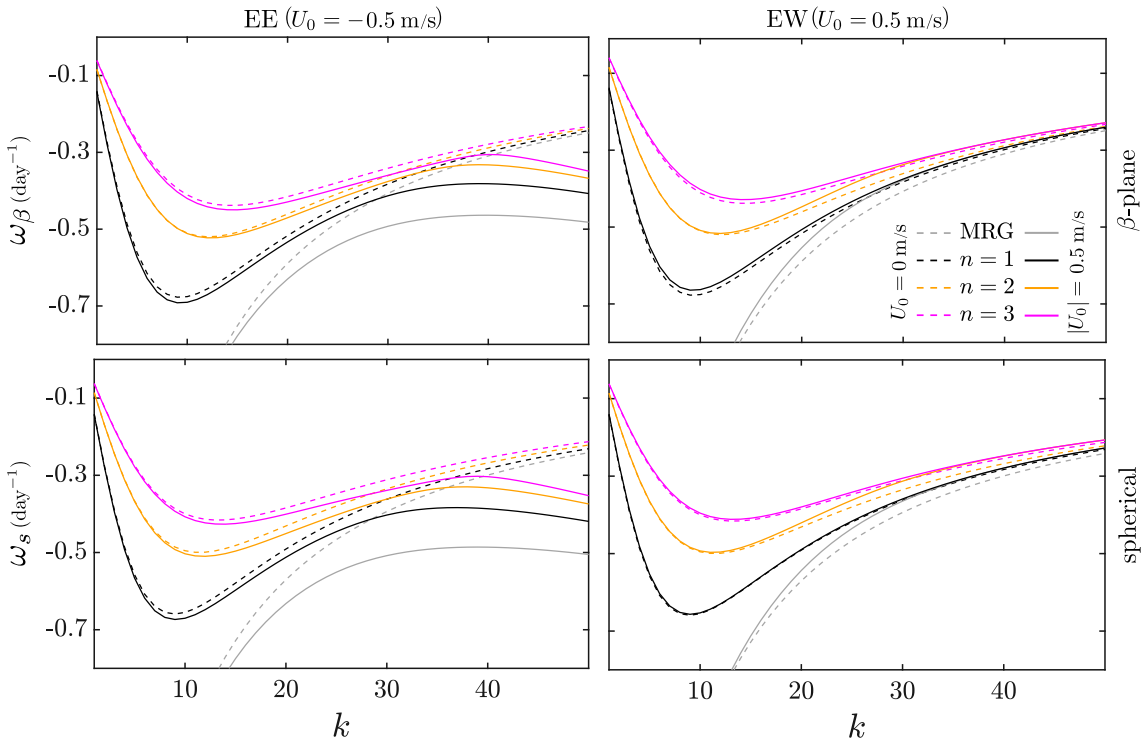

Figure 2.2: Dispersion curves for the Rossby and MRG waves in the β-plane (top) and the spherical system (bottom) for EE (left) and EW (right). Solid lines correspond to $|U_0| = 0.5$ m/s ($|Fr| = 0.02$) and dashed lines are for $U_0 = 0$ (no mean flow). Note that all the waves, both in the β-plane and on sphere are neutral. For equatorial westerly flow (EW), the frequencies corresponding to successive n are closely clumped for large k. For equatorial easterly flow (EE), the short waves (large k) tend to be non-dispersive, in contrast with the $U_0 = 0$ short waves that are dispersive with $\omega \sim -k^{-1}$.

Figure 2.2 shows the dispersion curves of MRG and Rossby modes for the first few values of n. The waves travel westward with a higher phase speed in EE than in EW, a characteristic also noted in [37]. From the figure, for both EE and EW, it is apparent that the deviations in the frequency in the presence of shear flow are more pronounced for short waves (high k). When the mean shear flow is weak, we see that the spectra are qualitatively similar in the spherical system and the β-plane. The eigenstructure however has pronounced differences, and we will return to this point.

MRG and Rossby waves have much slower phase speeds than the other families of waves. In the absence of shear, the dispersion relation for Rossby waves can be approximated by neglecting ω_β^2 in equation (2.17) [1, section 8.2] to get:

$$\omega_\beta \sim -\frac{k_\beta}{2n+1+k_\beta^2}. \tag{2.18}$$

The long waves ($k_\beta \to 0$) turn out to be effectively non-dispersive, propagating with a constant phase speed of $\omega_\beta/k_\beta \sim -(2n+1)^{-1}$. On the other hand, short waves ($k_\beta \to \infty$) are dispersive with the frequency scaling as $\omega_\beta \sim -k_\beta^{-1}$. It can also be noted that the frequencies of MRG and Rossby modes remain distinct for sufficiently large values of k_β in the absence of shear flow.

With EE, long waves continue to remain non-dispersive as in the zero mean shear configuration. In contrast to the case with no shear, however, the dispersion curve turns around, and short waves again tend to become non-dispersive (showing a constant phase speed) for each n that is lower than the Kelvin wave phase speed. With EW, waves of successive n display frequencies which clump closer to each other with increasing k. This clumping is less in the spherical system for a given k. Using the base flow profiles considered by [37], we were able to discern similar characteristics for short waves (not shown). In their study, these properties were not as evident owing to the smaller range of wavenumbers considered.

In order to compare the spectra of the β-plane and spherical systems, we compute the percentage difference as

$$\delta_\omega = \frac{\omega_\beta - \omega_s}{\omega_s} \times 100, \tag{2.19}$$

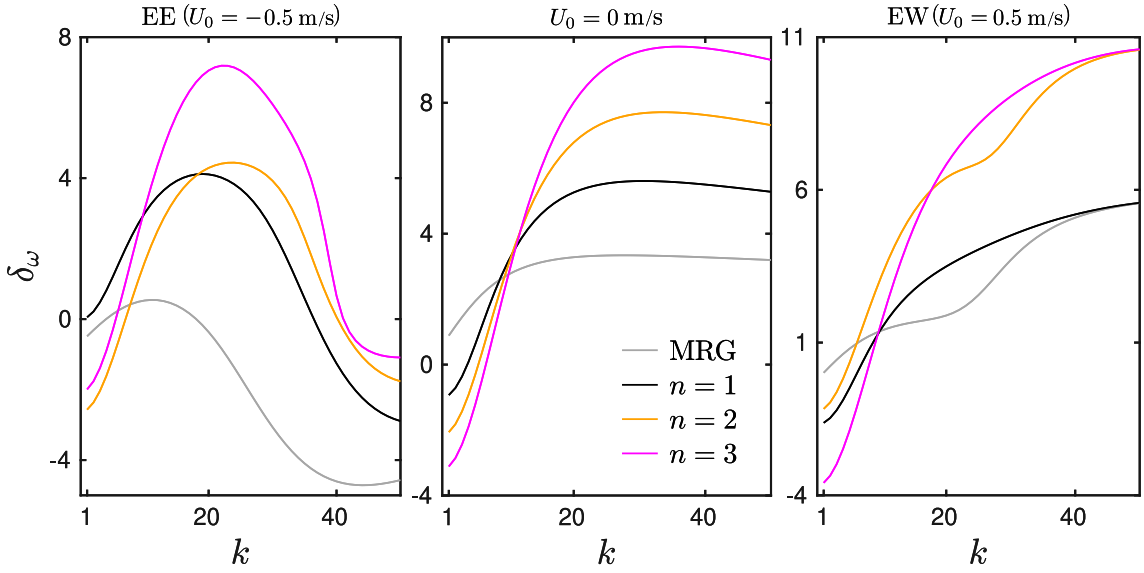

Figure 2.3: Relative difference δ_ω (defined in equation (2.19)) between eigenvalues of the modes on the β-plane and the spherical systems for MRG ($n = 0$) and Rossby modes ($n \geq 1$) for EE (left), no mean flow (centre), and EW (right). Even for a base flow confined to low latitudes, the deviations between the spectrum of the β-plane and spherical system are significant at moderate to high k, especially for EW.

and plot it in figure 2.3 for the case of no mean shear (middle), EE (left) and EW (right). In the absence of shear, there is already a deviation between results from the two systems, but this remains bounded within 10%. The frequency obtained under the β-plane approximation is seen to be underestimated for a majority of the long waves (small k). For short waves, there is a larger overestimation of the phase speeds, e.g., in the $n = 2$ and $n = 3$ Rossby modes with EW as the mean flow. It is curious that the margin of error is low for smaller k regardless of the type of mean flow, whereas intuition would not suggest this. In the following subsection, we examine the corresponding eigenfunctions to fully appreciate the limitations of the β-plane approximation.

2.3.2 Eigenfunctions

In the β-plane setting in the absence of shear flow, the meridional velocity takes the form [8]:

$$v_\beta(y) = He_n(y) \exp(-y^2/2), \tag{2.20}$$

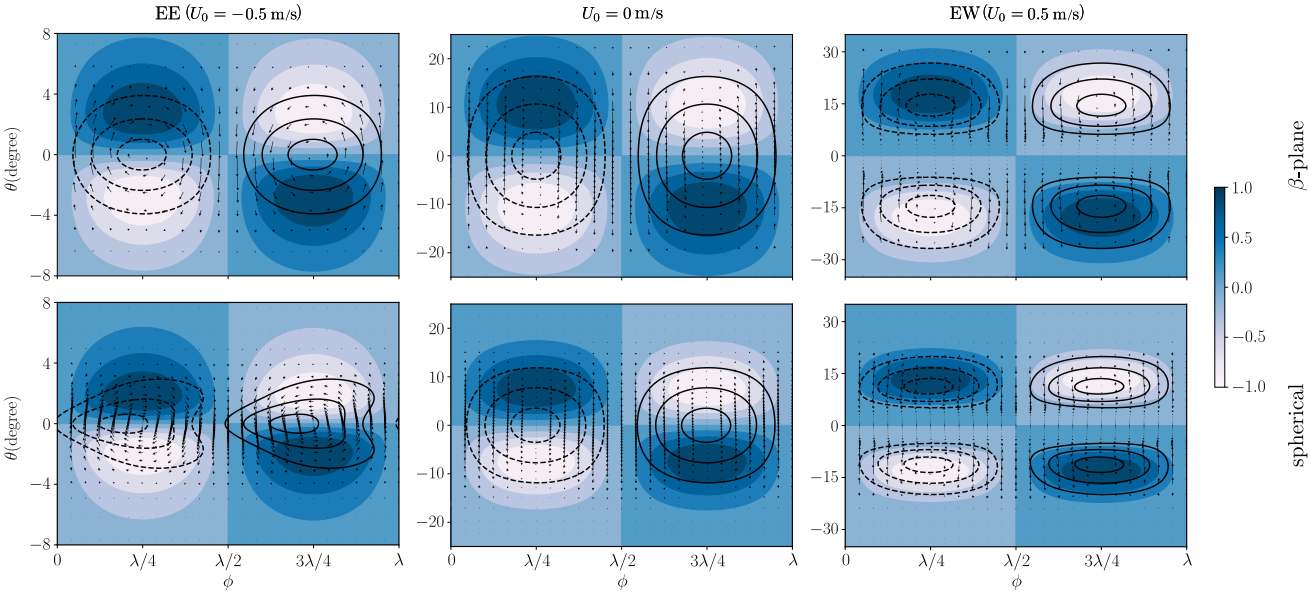

Figure 2.4: The MRG ($n = 0$) modes for $k = 50$ in the β-plane (top) and spherical (bottom) systems with EE (left), no shear (centre) and EW (right); the perturbation wavelength is $\lambda = 2\pi/k = \pi/25$ here. Line contours and arrows depict the vorticity and the velocity respectively; colour contours depict the surface elevation. The dashed and continuous contours correspond, respectively, to the negative and positive values of vorticity. Note that the limits in the latitude are not the same across the different panels. With shear, eigenfunctions are clearly less confined in the β-plane than in the spherical system, and in EW than EE.

where $He_n(y)$ is the nth order Hermite polynomial having n zeros [66]. As was done for the analysis of the spectra, we continue to employ the meridional mode number n to classify the eigenfunctions.

In figures 2.4 and 2.5, the $n = 0$ MRG and $n = 1$ Rossby modes are shown in the different mean flow configurations for the β-plane and spherical settings. We choose $k = 50$ for a demonstration of the findings, which corresponds to a wavelength of about 800 km. This example is characteristic of the entire range of high wavenumbers. Note that for plotting eigenfunctions obtained in the β-plane setting, we use $\theta = L_\beta y/R$. In the absence of mean flow, a primary feature of modes with even n is a longitudinal cross equatorial flow with a vortex cell centered at the equator. While this feature is still apparent for EE, the mode is characterised by two off-equatorial vortices accompanied by a quiet band around the equator when the mean flow is EW. When n is odd, with zero mean flow, the eigenfunction is characterised by off-

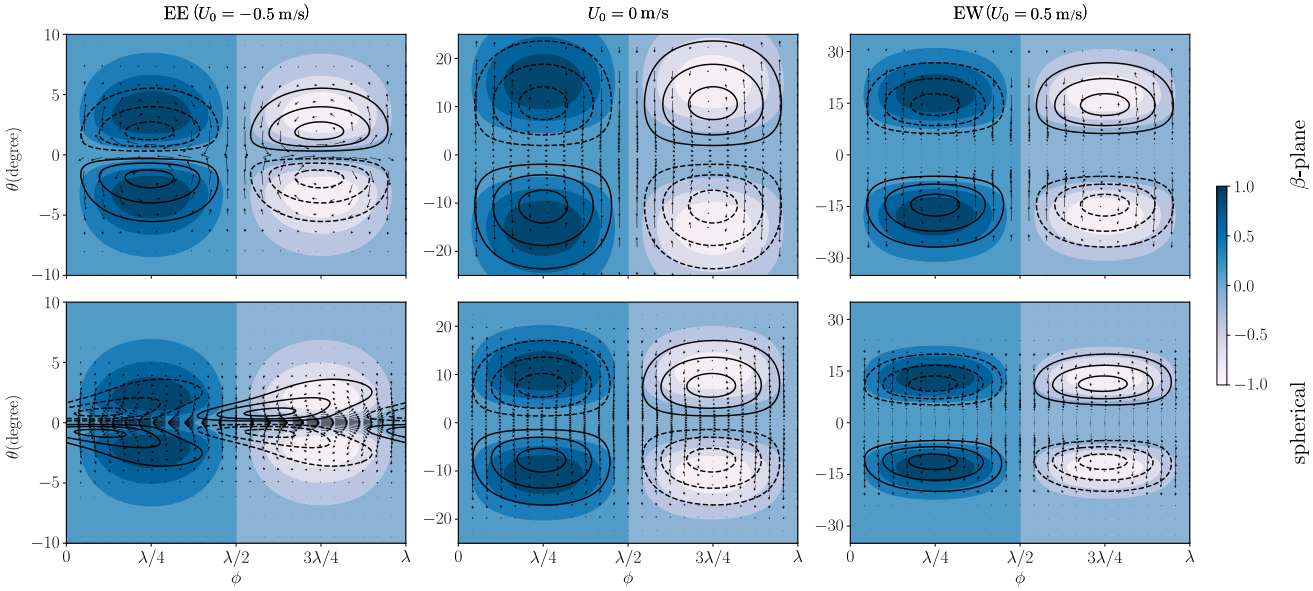

Figure 2.5: Same as figure 2.4, but for $n = 1$. Again, the eigenfunctions are less confined to the equatorial zone in the β-plane than on a sphere in the presence of shear.

equatorial vortices with a strong equatorial zonal flow. Once again, with EE as the mean flow, these qualitative features are retained. With EW, as before, the mode is quiescent near the equator with prominent off-equatorial vortices. With regard to the surface elevation, the fields are symmetric and antisymmetric about the equator when n is odd and even respectively.

Whether in EE or EW, the eigenfunction is more confined in the meridional direction for the complete spherical system for large k. For small k, the disturbance flow extends into the extratropics, far beyond the mean flow, which is negligible beyond 8 degree north or south. The visual evidence of figures 2.4 and 2.5 can be made more quantitative. To this end, for an eigenfunction $\tilde{\mathbf{q}}$, we define:

$$\|\tilde{\mathbf{q}}\|^2(\theta) = \frac{1}{4}\int_{-\theta}^{\theta} \mathrm{d}\theta' \ \cos\theta' \left(\tilde{u}^\dagger\tilde{u} + \tilde{v}^\dagger\tilde{v} + \tilde{h}^\dagger\tilde{h}\right) \ , \tag{2.21}$$

$$\text{and } \tau(\theta) = \frac{\|\tilde{\mathbf{q}}\|^2(\theta)}{\|\tilde{\mathbf{q}}\|^2(\pi/2)} \quad \text{for } 0 \le \theta \le \frac{\pi}{2} \ . \tag{2.22}$$

In the above, the dagger symbol (†) represents the complex conjugate. Note that $\|\tilde{\mathbf{q}}\|^2$ (and hence τ) monotonically increases with θ. As a result, we can define a

threshold latitude θ_τ as the value of θ for which τ takes a specific value; we choose $\tau = 0.9$ for our analysis. A small (large) θ_τ is associated with a high (low) degree of equatorial confinement.

Figure 2.6 shows θ_τ as a function of k for MRG and Rossby waves in EE and EW. This helps us examine the characteristics of waves ranging from planetary scales ($k \sim 1$–5) all the way to mesoscales ($k \sim 30$–50). Even though the mean flow is extremely confined equatorially, the perturbation waves it creates extend poleward. For the lower values of k, where we do not expect the β-plane system to perform well in approximating the full spherical system, the eigenfunctions on the β-plane are found to be more equatorially trapped. For larger wavenumbers, however, contrary to the expectation of a better agreement between the β-plane and the spherical systems, the degree of equatorial trapping turns out to be underestimated under β-plane. Consistent with the zero mean flow scenario, for lower values of k, the degree of confinement reduces as n increases. The short waves (large k) are significantly more equatorially trapped for EE than EW, showing the same trend as results pertaining to the meridional scale of Rossby waves for base flow of [37]. For EW at higher k it was seen (right panels of figure 2.2) that eigenvalues belonging to successive n were clustered together (see section 2.3.1). We see a similar feature in the degree of the confinement of the eigenfunctions in figure 2.6. For larger k, θ_τ get closer for successive values of n.

Next, we examine the characteristics of the perturbation zonal velocity and surface elevation. For a given eigenmode, these quantities can be expressed in terms of the perturbation meridional velocity and its meridional gradient as follows:

$$\tilde{u}_s = i\mathcal{S}_{uv}\tilde{v}_s + i\mathcal{S}_{uDv}D_y\tilde{v}_s,\ \tilde{h}_s = i\mathcal{S}_{hv}\tilde{v}_s + i\mathcal{S}_{hDv}D_y\tilde{v}_s\ , \tag{2.23}$$

$$\tilde{u}_\beta = i\mathcal{B}_{uv}\tilde{v}_\beta + i\mathcal{B}_{uDv}D_y\tilde{v}_\beta,\ \tilde{h}_\beta = i\mathcal{B}_{hv}\tilde{v}_\beta + i\mathcal{B}_{hDv}D_y\tilde{v}_\beta\ . \tag{2.24}$$

Appendix B gives explicit formulae for the coefficients above as functions of the base flow state and the eigenvalue. We define the number of zeros of the zonal velocity and the surface elevation as n_u and n_h respectively. For the zero mean flow case in the β-plane setting, with $\tilde{v}_\beta$ given by equation (2.20), $n_u = n_h = n+1$ for the MRG and Rossby modes. We report that this relationship for n_h continues to hold in the presence of shear flow for the range of wavenumbers considered here although there

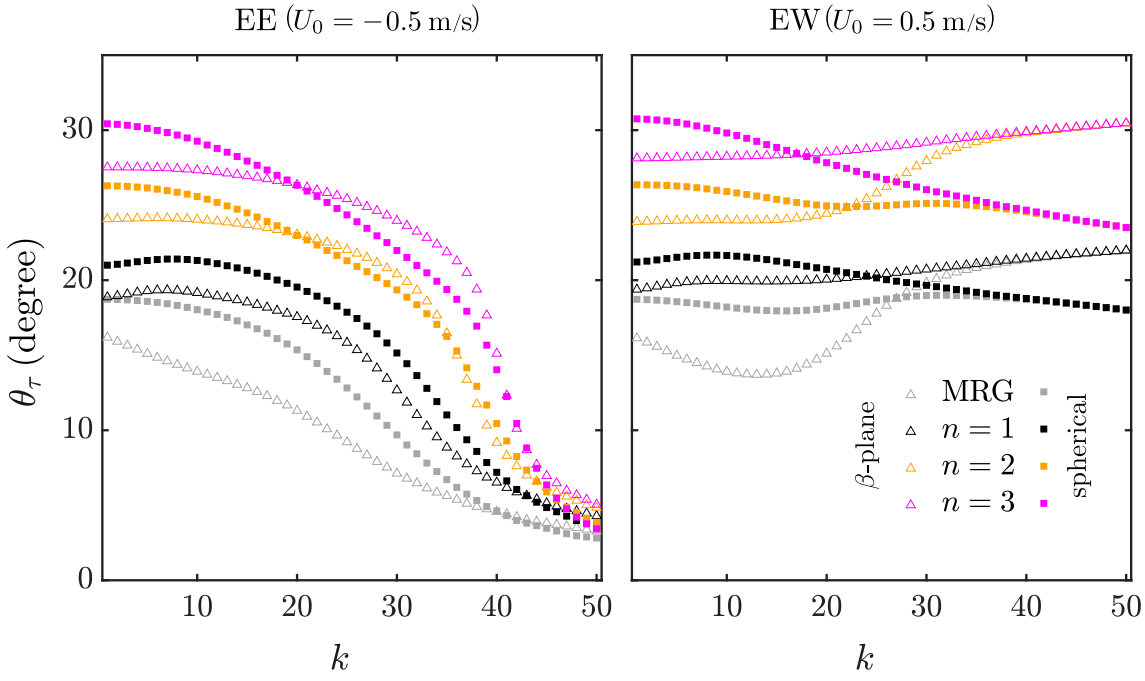

Figure 2.6: The latitude θ_τ (for $\tau = 0.90$) as a function of the wavenumber k in the β-plane (triangles) and the spherical system (squares) for EE (left) and EW (right). At small k, the meridional extent of the waves is lower in the β-plane setting. On the other hand, the β-plane overestimates the meridional extent for the waves at larger k.

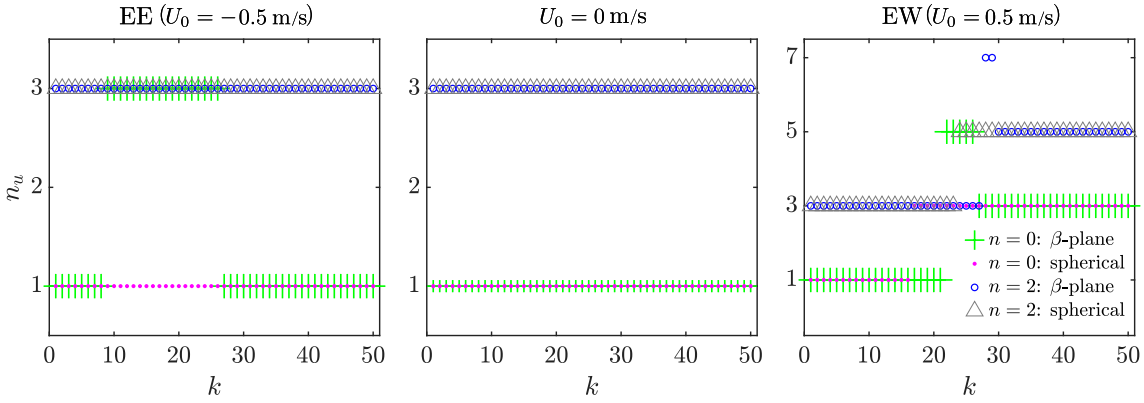

Figure 2.7: Number of zeros (n_u) in latitudinal variation of the zonal perturbation velocity field ($\tilde{u}$) as a function of k in the presence of EE (left), no shear (centre) and EW (right) in the β-plane and spherical systems. Compared to the zero mean shear case, the relationship $n_u = n+1$ does not hold in the presence of shear for a range of values of k. This leads to the bifurcation of the equatorial vortex of eigenfunctions corresponding to even n into two off-equatorial vortices (see section 2.3).

are notable changes in n_u, as discussed below.

In the zero mean flow case, we have $n_u = n + 1$ for all k. The corresponding velocity field involves either a cross-equatorial flow (even n) or an equatorial zonal flow (odd n). We report that when n is odd, n_u remains unchanged for the non-zero mean flow cases. In contrast, for even n, there are notable changes in n_u with change in the wavenumber. In figure 2.7, we plot n_u as a function of the wavenumber for $n = 0$ and $n = 2$. The central panel shows the zero mean flow case to serve as a reference, and the left and right panels are for EE and EW with $|U_0| = 0.5$ m/s. With EE as the mean flow, the perturbation velocity characteristics around the equator are similar to those obtained in the zero mean flow case. There is a range of wavenumbers for which $n_u = n + 3$ in the β-plane setting (see the left panel of figure 2.7).

The differences in n_u are more stark when EW is the mean flow. For lower values of k, the cross-equatorial flow continues to be prominent. As k increases, the eigenfunction structure comprises two off-equatorial vortices in addition to the equatorial vortex. These off-equatorial vortices become more pronounced with increasing k. While $n_u = n+1$ for the large part, there are some values of k for which $n_u = n+5$ in the β-plane setting. As k increases further, the off-equatorial vortex cells become

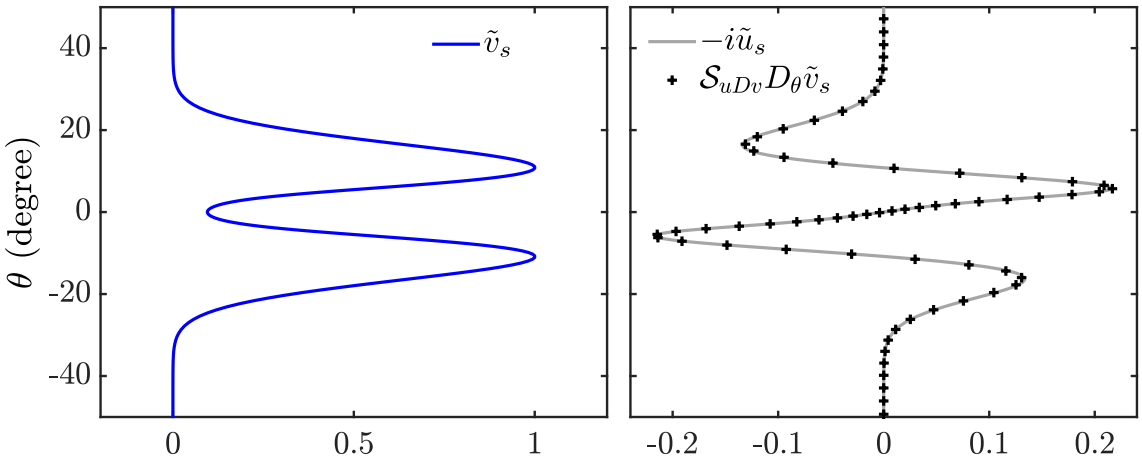

Figure 2.8: The velocity components of the MRG mode (in spherical coordinates) when $k = 40$ and $U_0 = 0.5$ m/s (EW). In the left panel, the meridional velocity $\tilde{v}_s$ is seen to have three local extrema. On the right, the dominant contribution to the zonal velocity $\tilde{u}_s$ is shown to be from the term proportional to $D_\theta \tilde{v}_s$. For this mode, $n = 0$ and $n_u = 3$.

dominant and the flow in the vicinity of equator is considerably weaker. Recall the nearly quiescent regions around the equator in figures 2.4 and 2.5. In this range of k, we have $n_u = n + 3$.

Using equations 2.23 and 2.24, we can understand the changes in n_u by examining the meridional velocity $\tilde{v}$ and its meridional gradient $D\tilde{v}$; as the arguments hold in both settings, we drop the subscripts that distinguish the quantities in the β-plane and the spherical system. We find that the dominant contribution to the zonal velocity $\tilde{u}$ is due to the term proportional to $D\tilde{v}$, and consequently n_u is precisely the number of sign changes in $D\tilde{v}$. We show this explicitly for the MRG mode (with $n = 0$) when $k = 40$ and $U_0 = 0.5$ m/s in figure 2.8. Therefore, the seemingly abrupt jumps in n_u are accounted for by the changes in the number of local extrema of the meridional velocity $\tilde{v}$.

2.4 Strong Shear

We now turn our attention to the stability characteristics of base flow configurations with larger $|U_0|$. Although the mean flow profile considered is idealised, our choices for $|U_0|$ here are motivated by the mean velocities at the equator obtained from cli-

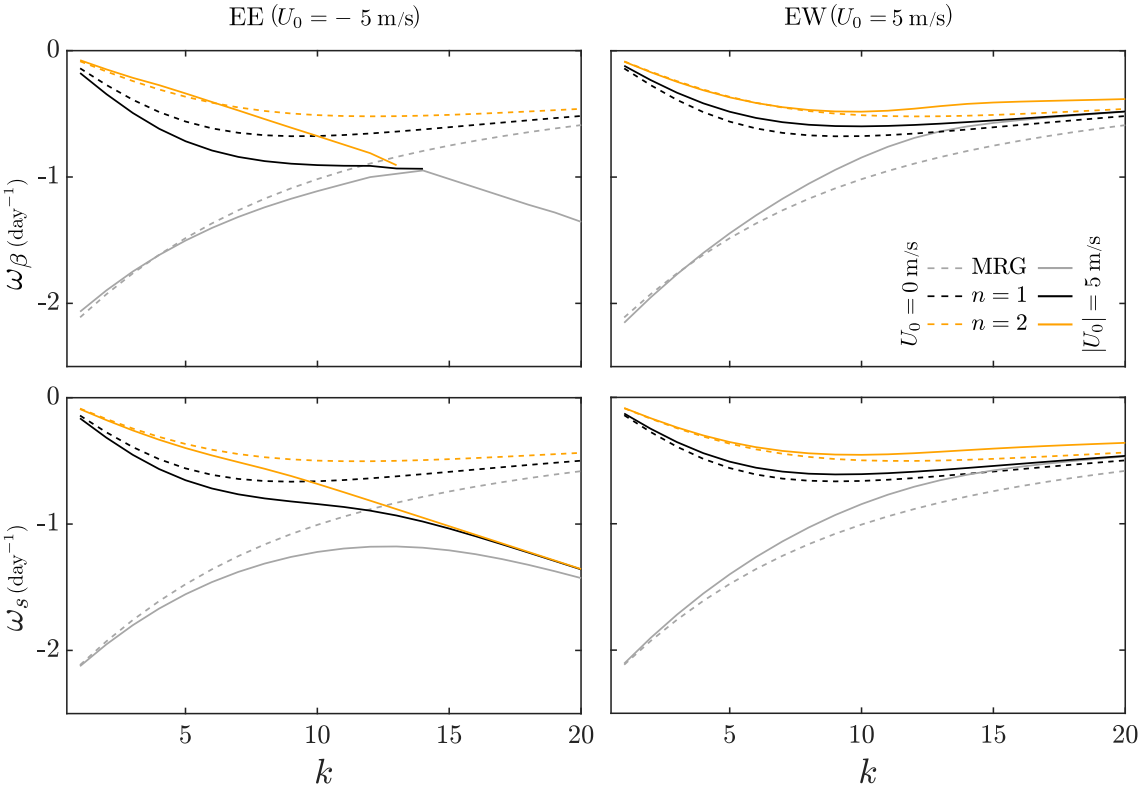

Figure 2.9: Dispersion curves for the Rossby and MRG waves in the β-plane (top) and the spherical system (bottom) for EE (left) and EW (right). Solid lines correspond to $|U_0| = 5$ m/s and dashed lines are for $U_0 = 0$ (no mean flow). For equatorial westerly flow (EW), the frequencies corresponding to successive n are closely clumped for large k. For equatorial easterly flow (EE), the short waves (large k) tend to be non-dispersive.

matological data [64]. We discuss four cases with $|U_0| = 5, 10, 15, 20$ m/s, which correspond to $Fr = 0.159, 0.319, 0.479, 0.639$ and $Ro = 0.0054, 0.0108, 0.0161, 0.0215$.

When compared with the low shear cases, the classification of modes becomes relatively challenging. As in the low shear configurations, the modes are categorised into different wave families based on the number of zeros of its meridional velocity component. We first examine the changes in the features of the MRG and Rossby modes with increasing shear. Figure 2.9 shows the eigenfrequency of MRG and Rossby for $|U_0| = 5$ m/s. The deviations in the phase speeds of the various waves from the zero mean case are considerably larger as expected. Note that the eigenfrequencies of $n = 1$ and $n = 2$ Rossby modes for the β-plane system in EE are shown

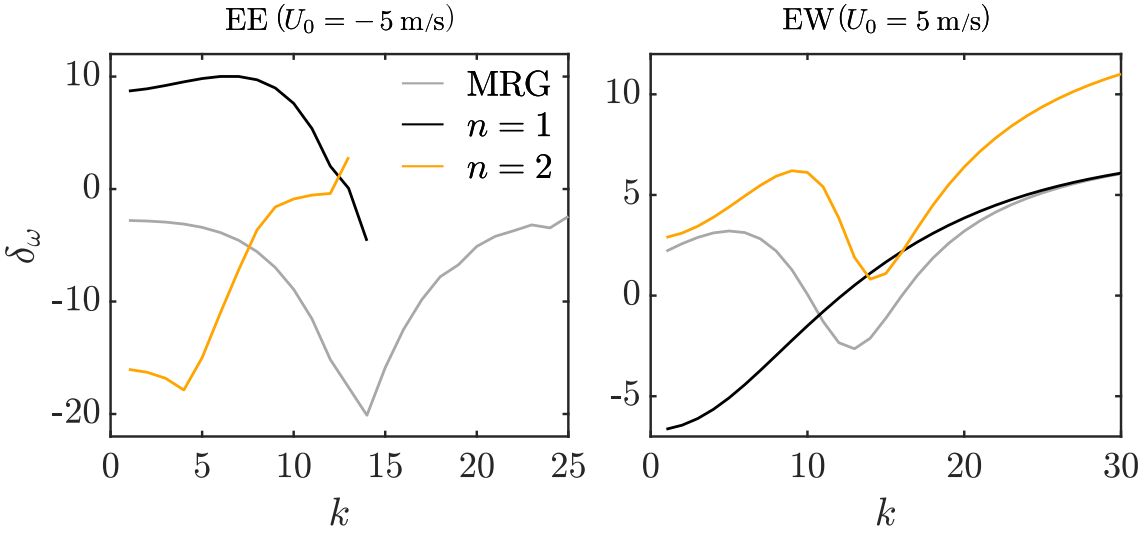

Figure 2.10: Relative difference δ_ω (defined in equation (2.19)) between spectra of the β-plane and the spherical systems for MRG ($n = 0$) and Rossby modes ($n \geq 1$) for EE (left) and EW (right) when $|U_0| = 5$ m/s. The deviations between the two systems are in a similar range as in the low Fr case (see figure 2.3).

for a smaller range of wavenumbers (k ∼1-15) owing to the difficulty of resolving the modes at such high shear employing the current numerical method.

Beyond these quantitative changes, the system retains most of the qualitative features as observed in the low Fr regime. The non-dispersive nature of short waves in EE is evidently clear even for relatively moderate wavenumbers ($k \gtrsim 15$). In EW, as in weak shear, the frequencies of modes corresponding to successive n become nearly indistinguishable with increasing k. Compared to the low Fr regime, the clumping of frequencies starts at considerably lower wavenumbers ($k \gtrsim 15$). In figure 2.10, we plot δ_ω as a function of the wavenumber k. For the most part, it is seen that the phase speed obtained in the β-plane is still within $\pm 10\%$ of that of the spherical system. We report that the discrepancy in the phase speeds become more pronounced with increase in $|U_0|$.

On examining the eigenfunction structures of the MRG mode in the presence of a stronger mean shear with $|U_0| = 5$ m/s (Figure 2.11), the differences in the degree of trapping with EE and EW as the mean flows are no longer as prominent as in the case of low Fr. The latitudinal spans are also similar in the β-plane and spherical systems. The identification of the MRG mode continues to be based upon n. The

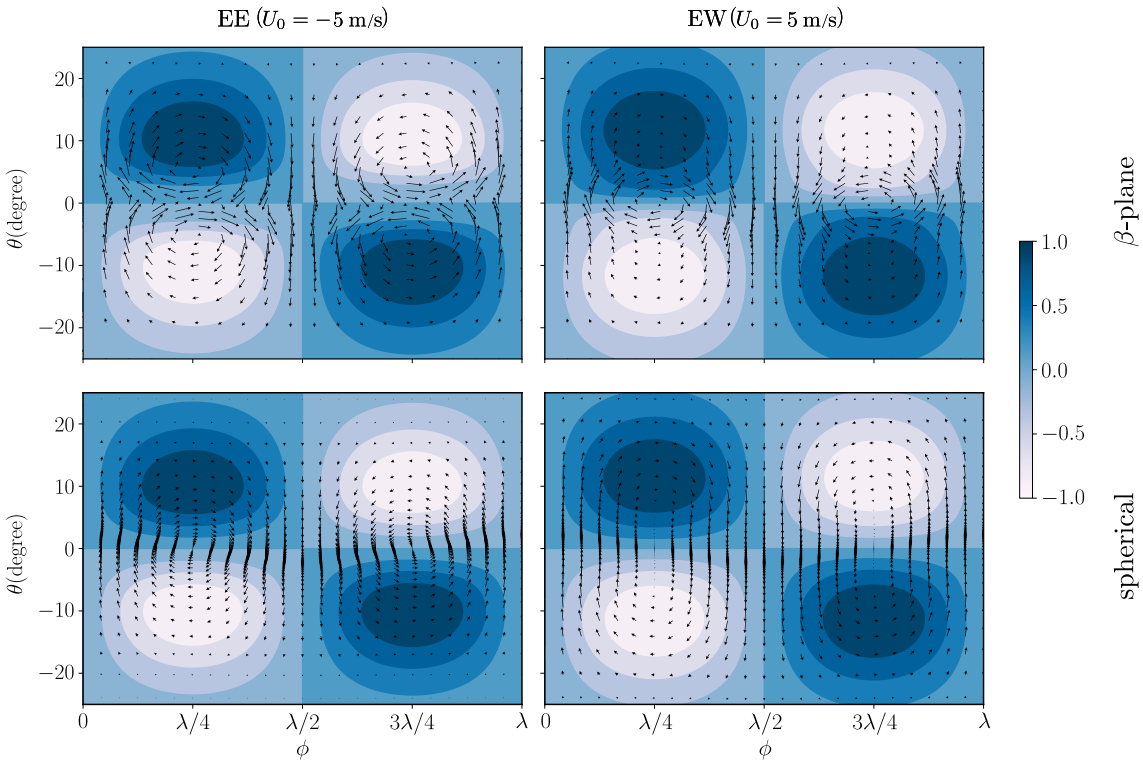

Figure 2.11: The MRG ($n = 0$) modes for $|U_0| = 5$ m/s and $k = 10$ in the β-plane (top) and spherical (bottom) systems with EE (left) and EW (right); the perturbation wavelength is $\lambda = 2\pi/k = \pi/5$. The arrows depict the velocity and the colour contours depict the surface elevation.

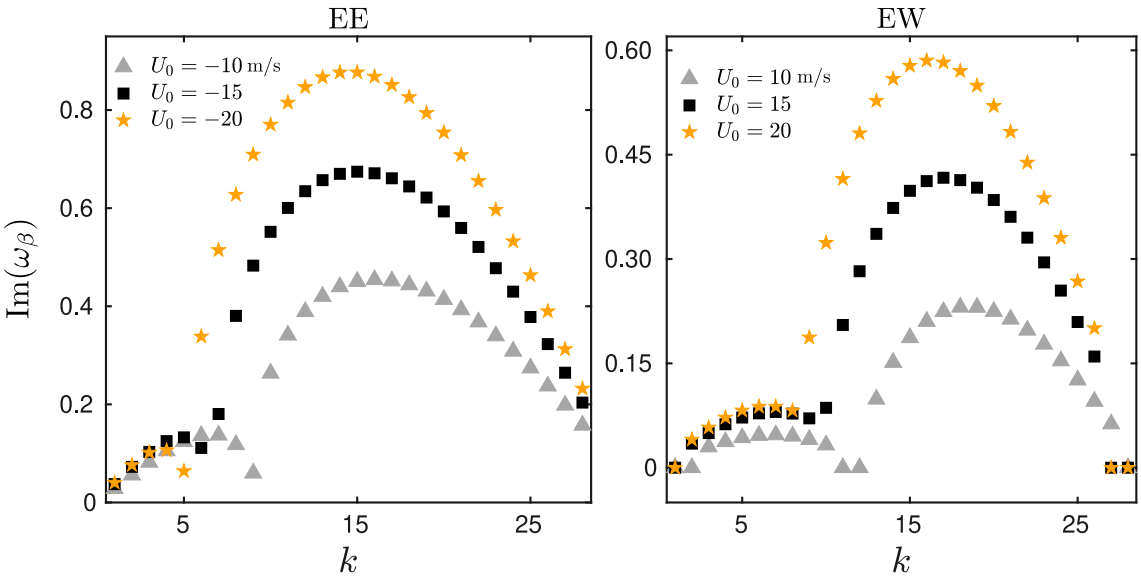

Figure 2.12: Growth rates of the most unstable mode in the β-plane setting. The system exhibits higher growth in EE (left) compared to EW (right). The peaks at low and high k correspond to two distinct modes.

antisymmetric geopotential field accompanied by an equatorial vortex, which are the distinguishing features of the MRG mode, are observed to hold. Under the β-plane approximation with EE as mean flow, the mode exhibits additional features of bimodality in the velocity structures; a closer examination of the mode reveals a higher value n_u.

Despite an increase in Fr, the base flow remains modally stable in the spherical setting. In stark contrast, for the same mean flow, the β-plane approximation predicts exponentially growing disturbance modes. Figure 2.12 shows the growth rates of the most unstable mode in the β-plane as a function of the wavenumber k for different values of $|U_0|$; we do not show results for $|U_0| = 5$ m/s as the unstable modes are excited for only a small range of k. The non-monotonic nature of the curves arises from the fact that there are different types of unstable modes. For the parameters considered here, at a given k, these modes could belong to different branches of the eigenspectrum. As the strength of the mean flow increases, the wavenumber at which the maximum growth rate is achieved reduces.

Selecting the case with $|U_0| = 10$ m/s, we now take a closer look at the unstable modes obtained in the β-plane setting. For other $|U_0|$ in this regime, similar

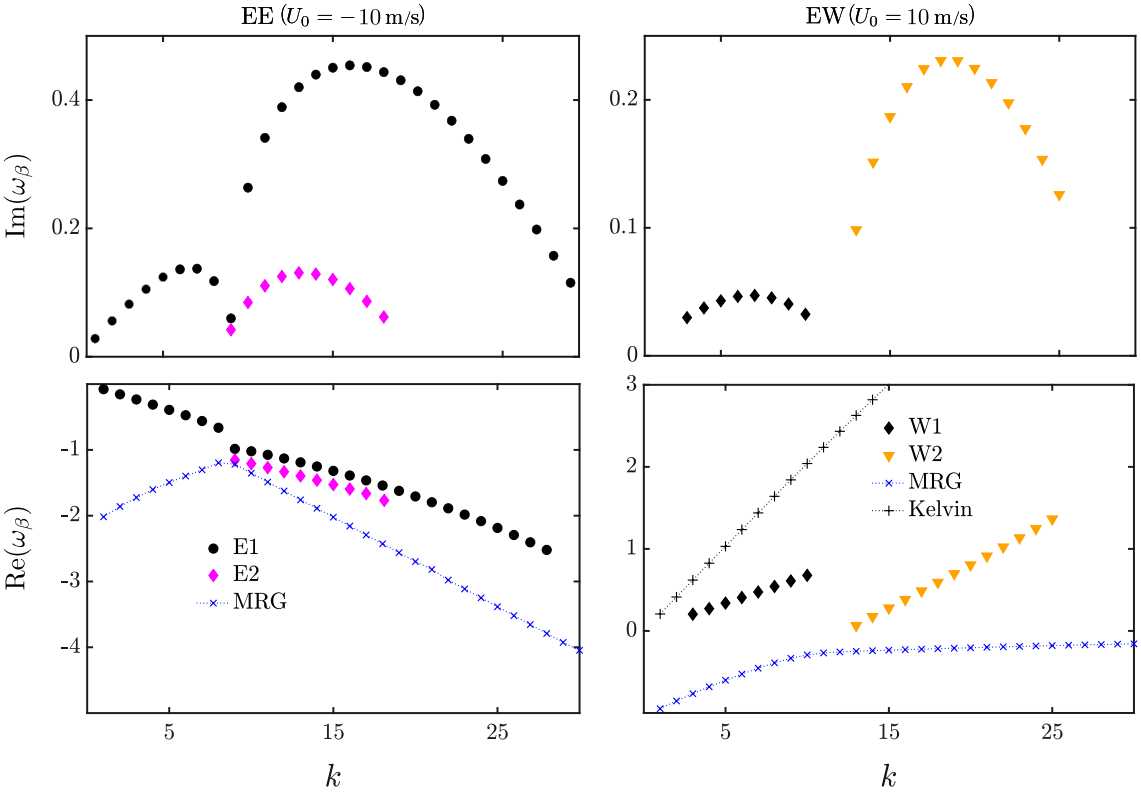

Figure 2.13: The growth rates (top) and the frequencies (bottom) of different unstable modes of RSWE on β-plane in the presence of EE (left) and EW (right) for $|U_0| = 10$ m/s. The frequencies of the MRG and Kelvin modes are shown for reference. Note that the spherical system does not yield any unstable modes.

behaviour is observed. In figure 2.13, we show the growth rates $\mathrm{Im}(\omega_\beta)$ of the unstable modes and their corresponding frequencies $\mathrm{Re}(\omega_\beta)$. One notable feature is that instabilities occur for the lower range of k, where the suitability of the β-plane approximation is already in question. In the bottom panels, we also show the frequencies of the Kelvin and MRG modes. Thus, it is possible to recognise if these modes can be categorised into any of the established wave families.

With EE as the mean flow, the unstable modes are westward-propagating with smaller phase speeds than that of the MRG mode. This suggests these modes have propagation characteristics similar to those of Rossby modes. The corresponding eigenfunctions of the most unstable modes (E1) change gradually with k. For low values of k, there is an dominant equatorial vortex accompanied by weak off-equatorial vortices (see top left panel in figure 2.14). As k assumes more moderate values,

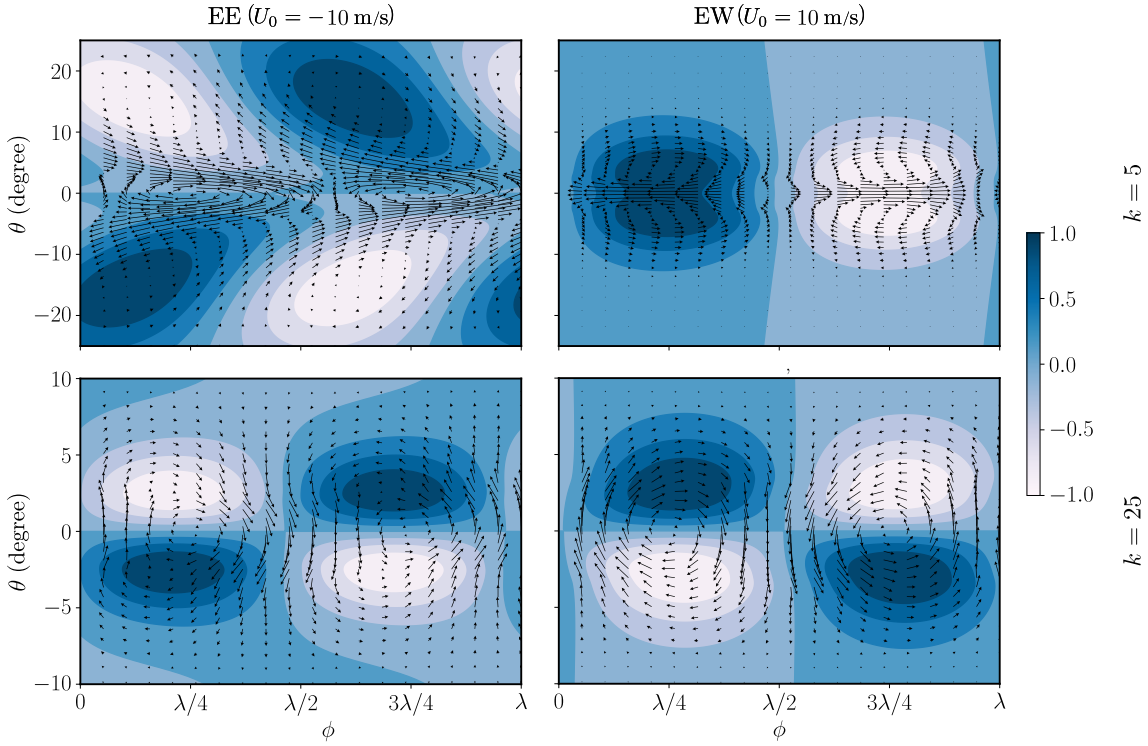

Figure 2.14: The most unstable mode in the β-plane setting for $k = 5$ (top) and $k = 25$ (bottom) in the presence of EE (left) and EW (right) for $|U_0| = 15$ m/s. The arrows depict the velocity and the colour contours depict the surface elevation. Note that the limits in the latitude are different for the top and bottom panels.

these two vortical features have comparable strengths. Upon further increase in k, a predominantly equatorial vortex resembling the traditional MRG mode emerges (bottom left panel in figure 2.14). All these modes have even n, and consequently the associated geopotential fields are antisymmetric about the equator. It was shown in figure 2.9 that there is a range of moderate k for which two unstable modes are found simultaneously. The less dominant unstable mode E2 (not shown) has characterstics of $n = 1$ Rossby mode, i.e., zonal equatorial flows sandwiched between off-equatorial vortices (see the middle panels of figure 2.5). The unstable eigenfunctions are found to be more equatorially trapped with increasing k.

On the other hand, with EW as the base flow, the unstable modes are seen to have positive phase velocities. However, these velocities are less than that of the Kelvin wave. Therefore these unstable modes can not be classified into any family identified hitherto. The number of zeros in the meridional velocity component for

W1 and W2 are 0 and 1 respectively. Despite these modes propagating eastward, their velocity fields resemble those of the $n = 1$ Rossby at lower k while $n = 0$ MRG mode at large k, as shown in the right panel of figure 2.14. As in the case with EE as the base flow, the unstable eigenfunctions become more localised around the equator as k increases.

It is apparent that these unstable modes in β-plane discussed above have no counterpart in the spherical system. They emerge as an artefact of the β-plane approximation, and may be termed spurious for the earth system. This calls for caution while employing the β-plane approximation for stability studies, even for highly equatorially confined mean flows.

2.5 Effects of varying equivalent depth H_0

The effects of varying the equivalent depth H_0 are presented here for the Gaussian mean flows considered with $|U_0| = 0.5$ m/s. Note that varying H_0 while keeping U_0 fixed is effectively changing the value of Fr, i.e., increasing H_0 results in lower value of Fr and vice versa.

The top panels of figure 2.15 show the dispersion curves for a $n = 1$ Rosby mode in EE (left) and EW (right) for different values of H_0 in the spherical system. For a range of moderate wavenumbers ($k \sim 1-30$), the frequency increases with increasing H_0. Curiously, the frequencies of short waves ($k \gtrsim 40$), appear to be only weakly sensitive to the value of H_0. We have verified that these features hold for other Rossby modes with different n. Similar dispersion curves are also obtained when the analysis is performed using the β-plane approximation. The bottom panels of the figure 2.15 shows δ_ω as a function of k when $H_0 = 200$ m. While the deviations remain within nearly 10% when EE is the mean flow, δ_ω takes on relatively larger values for EW. This is similar to what we have earlier for $H_0 = 100$ m (see figure 2.3).

We plot the MRG mode for $H_0 = 200$ m and $|U_0| = 0.5$ m/s in figure 2.16. It is seen that the eigenfunctions tend to be slightly less equatorially trapped in both the β-plane and spherical settings when compared with the modes for $H_0 = 100$ m (figure 2.4). As was seen earlier, the eigenfunction in the spherical system is seen to have a smaller extent beyond the equator than its counterpart in the β-plane.

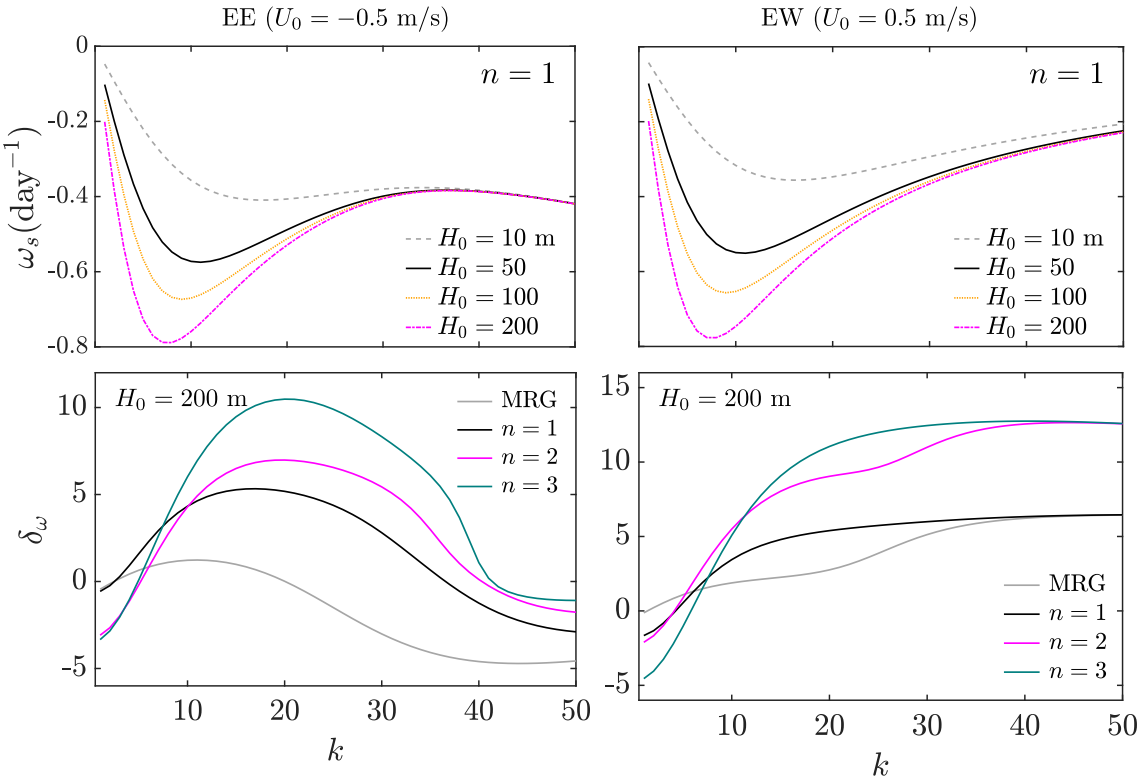

Figure 2.15: Top panels: dispersion curves for $n = 1$ Rossby mode in the spherical system in the presence of EE (left) and EE (right) for different values of equivalent depth (H_0). Bottom panels: Relative difference (δ_ω) (defined in eq. 2.19) between the spectra of the β-plane and the spherical system for MRG (n=0) and Rossby modes ($n > 1$) for $H_0 = 200$ m in the presence of EE (left) and EW (right).

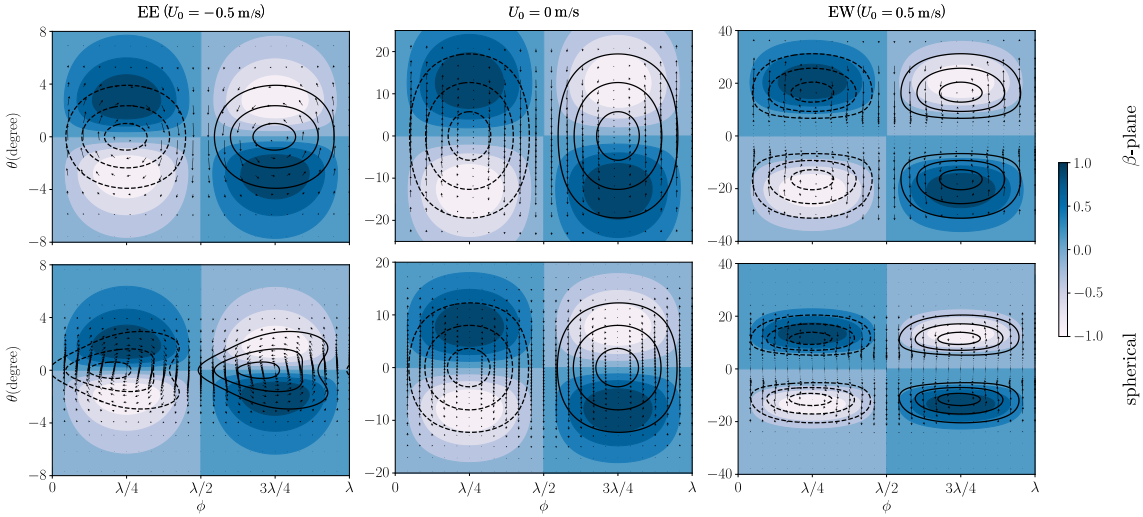

Figure 2.16: Same as figure 2.4, but for $H_0 = 200$ m. The eigenfunctions are observed to be less trapped for a higher H_0.

2.6 Stability analysis of Mexican hat profiles

Here, we analyse a different mean flow – one with a Mexican hat profile (see figure 2.17). This flow is characterised off-equatorial westerly flow; at the equator, the mean flow velocity could be negative (corresponding to EE) or positive (corresponding to EW). These profiles are motivated by those considered by Zhang & Webster [37]. Compared to their case, we choose the profiles to span considerably smaller latitudes so as to provide us with conditions under which, we may expect the β-plane approximation to perform well with the full spherical system. Further, the mean shear considered here is much weaker. For the velocity at the equator, we choose $|U_0| = 0.5$ m/s. As before, the mean flow is labelled as EE or EW depending on the sign of $|U_0|$.

The top panels of figure 2.18 show the dispersion curves for MRG ($n = 0$) and Rossby modes for the zero shear case and when $|U_0| = 0.5$ m/s. The qualitative features observed when the mean flow took the form of the Gaussian profile continue to hold. Short waves (large k) become nearly non-dispersive when the base flow is EE. With EW as the base flow, the frequencies of short waves for modes with successive n become nearly indistinguishable. The bottom panels show the relative difference in the frequencies of these modes in the β-plane and spherical system. For

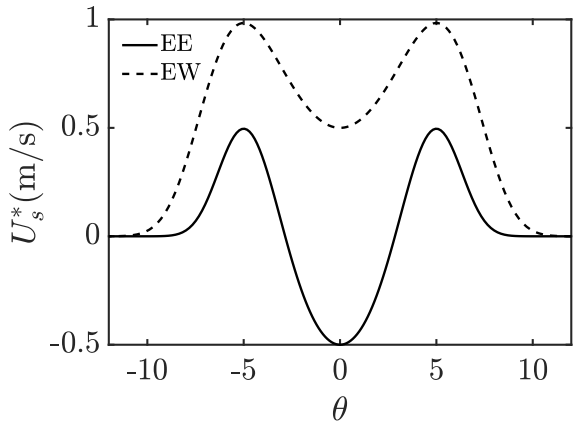

Figure 2.17: Profiles of equatorial easterly (EE) and equatorial westerly (EW) mean flow with Mexican hat profiles.

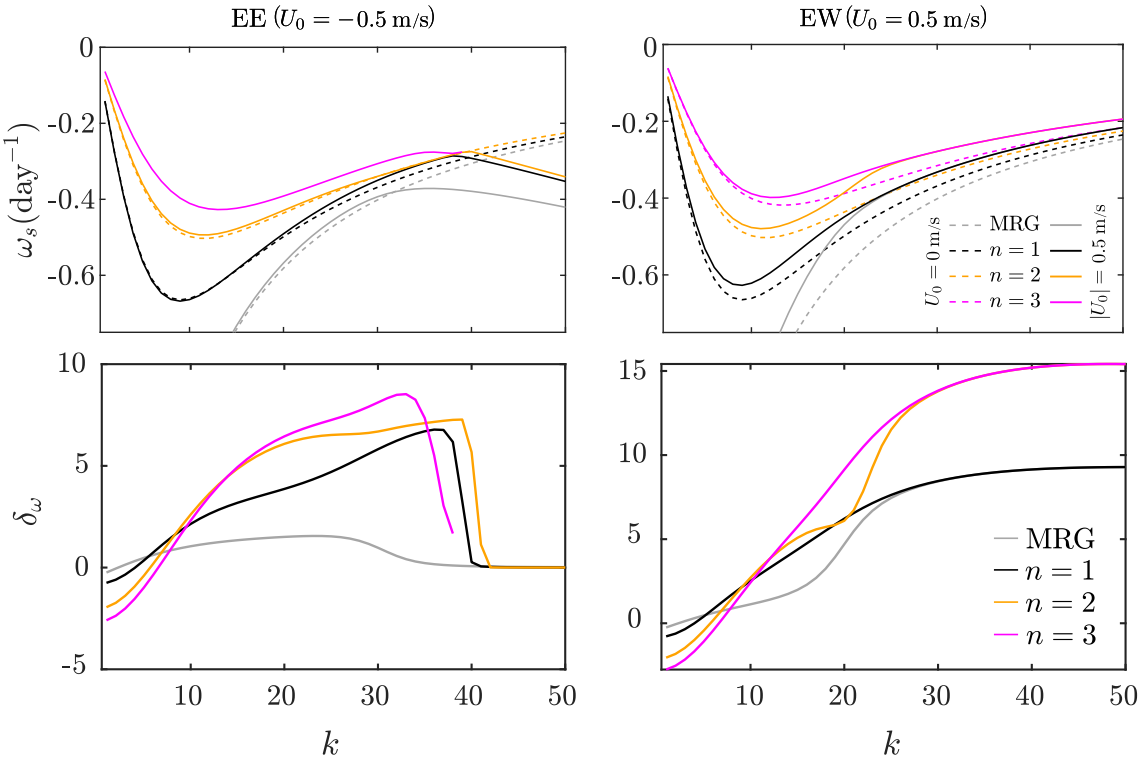

Figure 2.18: Top panels: dispersion curves for the first few Rossby and MRG waves in the spherical system (top) for EE (left) and EW (right) with $|U_0| = 0.5$ m/s ($|Fr| = 0.02$); the no mean flow case is shown for a reference. Bottom panels: δ_ω for the MRG ($n = 0$) and Rossby modes ($n \geq 1$) for EE (left) and EW (right).

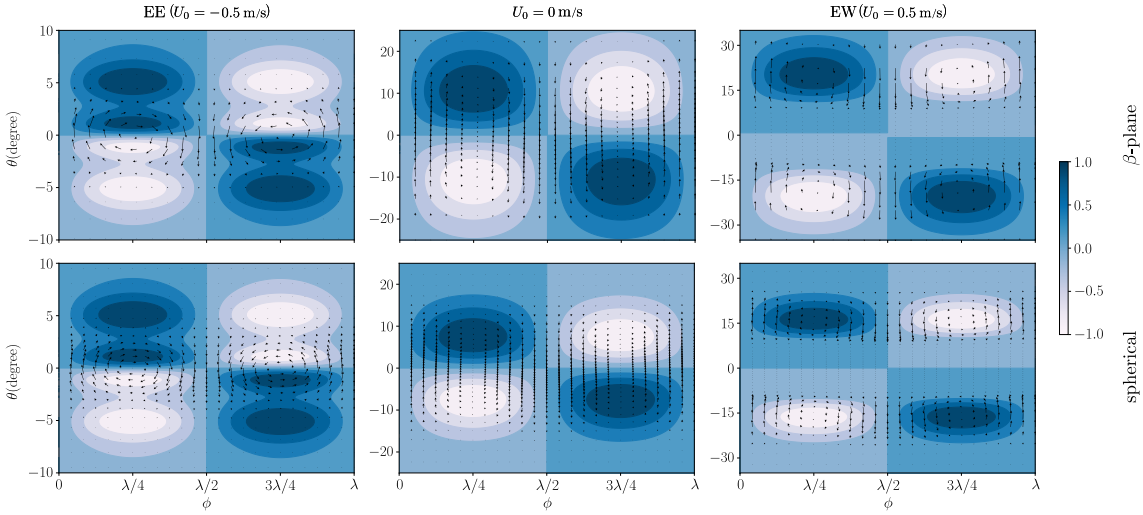

Figure 2.19: Same as figure 2.4, but for Mexican hat profile with $|U_0| = 0.5$ m/s. For this mode, $k = 50$ and $n = 0$. The broader qualitative features observed for the Gaussian profile continue to hold even for the Mexican hat mean flow.

EE, δ_ω is seen to be within 10 %. On the other hand, with EW as the mean flow, δ_ω takes values that are even higher than those for EW with a Gaussian profile. As in Gaussian profiles (see figure 2.3), the differences in frequency is relatively larger in EW than in EE.

Figure 2.19 shows the eigenfunctions of the MRG mode ($n = 0$) obtained in the β-plane (left) and spherical (right) settings for EW when $k = 50$. When comparing with the eigenfunction shown in figure 2.4, we see a greater degree of localisation of the eigenfunction when the mean flow assumes the Mexican hat profile. As in the case with the Gaussian mean flow profile, the eigenfunctions are less trapped in the β-plane system. We have verified that the qualitative features seen for the Gaussian mean flow is observed for the Mexican hat mean flow profile for other Rossby modes as well.

2.7 Summary and discussion

In this study, the stability characteristics of confined equatorial mean shear flows have been examined in the β-plane and spherical coordinate systems. It is seen that shear flow, even while itself highly confined to small latitudes, causes the perturbation energy to spread meridionally to a major extent, at all wavenumbers, and for

all families of atmospheric waves. It is hoped that this finding will motivate detailed simulations and comparisons with observations to understand non-local effects of shear flow on the earth system.

The β-plane approximation is designed to simplify the study of equatorial dynamics and is expected to correlate well with that of the full spherical system when the flow is confined near the equator. However we find that even under these conditions which are seemingly favourable for comparison, there are several notable differences in the results obtained with the linear β-plane and spherical systems, both in the spectra and the spatial structure of eigenmodes. Hence, in the presence of any equatorial shear, the stability analysis of the atmosphere must be performed in the full spherical system.

When the mean flow is weak with low Fr (section 2.3), the modes that are prominently affected are the MRG and Rossby modes. These waves propagate faster (slower) in the presence of EE (EW) when compared with the zero mean flow case. With respect to the zero mean flow configuration, the eigenfunctions are more (less) equatorially trapped in EE (EW). Moreover, the eigenfunctions are found to be more (less) equatorially trapped in the β-plane case compared to the spherical case for small (large) k. With EE as the mean flow, at high values of the wavenumber k, the waves become non-dispersive with a phase speed lower than that of the Kelvin mode. With EW, at high wavenumbers, the phase speeds of modes with successive n become increasingly close to each other. The consequences of this behaviour are reflected in the topological properties of eigenfunctions. The equatorially centred vortex (a signature of modes with even n in the absence of shear) bifurcates into two off-equatorial vortices for higher k.

For stronger mean flows with larger Fr (section 2.4), the dispersion curves in the two settings are qualitatively different, with additional branches appearing in the spectrum under the β-plane approximation. The physical origin of these branches and their relevance to equatorial dynamics would be important avenues for future research. More importantly, while the flow is shown to be unstable, with exponentially growing modes, in the β-plane system, the spherical system continues to remain neutrally stable. We note that these instabilities are seen only for a lower range of wavenumbers that are ill-suited for analysis in the β-plane, but which nevertheless are sometimes studied under this approximation. On analysing the

stability of the mean flow as a function of k, it is found that synoptic scale waves ($\lambda \sim 2500$ km) exhibit largest growth rates in most of the cases.

The methods used and the assumptions made in the present study naturally present some limitations to their application in a more realistic setting. The shallow water approximation neglects the variation of the vertical structure of atmosphere. In addition to this, the effects of a longitudinally varying mean flow and a non-zero meridional mean flow have not been studied here; such a scenario could also involve significant variations of the equivalent depth of the shallow layer. With effects of stratification (or vertical structure) incorporated, [67] showed that there are different types of instabilities depending on the lateral extent of the mean flow. It would be interesting to also examine if different classes of unstable modes emerge in a single layer as the mean flow's extent is varied. Finally, the analysis is linear, which restricts the investigation into the system over time scales when the perturbations are small enough for linearity to hold. However, the results obtained even with such a simplified model have non-trivial implications for the theoretical understanding of equatorial waves.

In the study of Zhang and Webster [37], the Rossby waves are shown to have smaller degree of equatorial trapping (larger meridional extent) in EW. As a result, it is speculated that tropical-extratropical interactions are more likely to occur at longitudes, where the zonal mean flow are westerlies. Our study shows that, the suggested differences in the latitudinal extent of the waves between EE and EW are prominent only at large wavenumbers ($k \gtrsim 40$). Further, the defining features of the Rossby waves corresponding to even values of n, i.e., cross equatorial flow with an equatorially centred vortex cease to hold in EW at large k. The eigenfunctions with off-equatorial vortices and a very weak equatorial flow can thus serve as markers for the identification of mesoscale ($\lambda \sim 500$ km) Rossby waves in the atmospheric in the presence of a westerly mean flow.

Chapter 3

Non-modal Analysis

The work presented in this chapter has benefited substantially from the guidance and contributions of Sharath Jose. The definition of the norm used, the notational conventions, and the protocol for constructing optimal perturbations in both the two-mode and multi-mode settings were proposed by him, including an analytical reduction in computational effort for the two-mode optimisation by relating the optimal target time to the difference in modal frequencies. His identification of the Lamb parameter as the determinant of normality, as well as his specifications for visualisation strategies and the interpretation of ϵ-bounded growth, were central in shaping both the methodology and the physical understanding of the results.

3.1 Introduction

In Chapter 2, we investigated the linear stability of the rotating shallow–water equations (RSWE) through a modal approach, wherein the perturbation fields are expanded in terms of eigenfunctions of the governing linear operator. This approach, which identifies the behaviour of disturbances through their associated eigenvalues, has historically been central to the stability studies of geophysical flows [8, 39, 68, 69] and has successfully described many features of tropical atmospheric variability [13, 19, 70–75]. Modal analysis, however, is fundamentally concerned with the asymptotic behaviour of the system where the eigenvalues determine exponential growth or decay, and the eigenfunctions (or normal modes) describe the spatial structure of disturbances. As such, modal analysis does not fully determine how a perturbation evolves over a finite time interval, where significant short-term amplification may occur even in the systems whose eigenvalues indicate neutral or decaying behaviour [51, 52, 76]. This phenomenon, known as non-normal growth, motivates the present

chapter, where we extend the analysis of Chapter 2 to the finite-time behaviour of perturbations. Nonmodal stability theory provides a complementary perspective to the classical modal analysis. Instead of characterising stability solely in terms of eigenvalues, the nonmodal approach explicitly retains the time scale over which disturbances evolve and formulates stability in terms of energy gain computed from the initial-value problem (IVP). Within this framework, a plane wave ansatz is assumed in the zonal direction leading to a general equation of the form

$$\begin{aligned} &\frac{\partial \hat{\mathbf{q}}}{\partial t} = \mathbf{A}\hat{\mathbf{q}}, \\ &\text{subject to initial condition, } \hat{\mathbf{q}}(0) = \hat{\mathbf{q}}_0, \end{aligned} \tag{3.1}$$

where, $\mathbf{A}$ is a general linearised operator governing the evolution of perturbation ($\hat{\mathbf{q}}$). Identifying whether the operator governing the dynamics is normal or non-normal offers some preliminary insight into the characteristics of the perturbation evolution. An operator is normal if it commutes with its adjoint, $\mathbf{A}^\dagger$ i.e., $\mathbf{A}\mathbf{A}^\dagger = \mathbf{A}^\dagger\mathbf{A}$. With an inner product of two state vectors $\hat{\mathbf{q}}_i$ and $\hat{\mathbf{q}}_j$ given by $\langle \hat{\mathbf{q}}_i, \hat{\mathbf{q}}_j \rangle$, the adjoint operator, by definition, satisfies $\langle \hat{\mathbf{q}}_i, \mathbf{A}\hat{\mathbf{q}}_j \rangle = \langle \mathbf{A}^\dagger \hat{\mathbf{q}}_i, \hat{\mathbf{q}}_j \rangle$. For normal operators, the eigenvectors form an orthogonal basis, and the eigenvalues completely determine perturbation behaviour at all time horizons. Such systems cannot exhibit nonmodal growth: any perturbation either decays, grows, or remains neutral at the exponential rate dictated by the eigenvalues. In contrast, non-normal operators do not commute with their adjoints. Their eigenvectors are non-orthogonal and, in general, do not form a complete basis. As a result, disturbances can evolve through linear combinations of eigenvectors that partially cancel or reinforce one another over finite times which can generate substantial transient amplification that is entirely invisible in the eigenvalue spectrum. Consequently, non-normal operators require more careful analysis, because their short-term behaviour can differ markedly from what modal stability analysis alone would suggest.

In majority of hydrodynamic flows, non-normality arises predominantly from the presence of mean shear, which produces transient growth through classical mechanisms such as the Orr mechanism [77], the lift-up effect [78, 79], and shear-induced vorticity tilting in barotropic and baroclinic shear flows [36, 49]. While mean shear is the driver of non-normality in such planar systems, spherical and other curved-

coordinate systems may exhibit non-normal behaviour even in its absence. To highlight this, the background mean shear is set to zero in this chapter. Setting $U_s = 0$ and $U_\beta = 0$ in eq. 2.14 and 2.16, respectively, the governing linearised operators on the β-plane and sphere in the absence of mean shear take the form,

$$\mathbf{M}_\beta = \begin{bmatrix} 0 & y & -ik_\beta \\ -y & 0 & -D_y \\ -ik_\beta & -D_y & 0 \end{bmatrix}. \tag{3.2}$$

$$\mathbf{M} = \begin{bmatrix} 0 & \sin\theta & -ik/(\epsilon\cos\theta) \\ -\sin\theta & 0 & -(1/\epsilon)D_\theta \\ -ik/\cos\theta & \tan\theta - D_\theta & 0 \end{bmatrix}. \tag{3.3}$$

In the spherical system, we choose to work with inner product having the following form:

$$\langle \hat{\mathbf{q}}_i, \hat{\mathbf{q}}_j \rangle = \frac{1}{2}\int_{-\pi/2}^{\pi/2} \mathrm{d}\theta \cos\theta \, (\hat{\mathbf{q}}_i^* \hat{\mathbf{q}}_j + \hat{\mathbf{q}}_j^* \hat{\mathbf{q}}_i). \tag{3.4}$$

In the above, and for the remainder of the chapter, any quantity with an asterisk represents a complex conjugate transpose. The integration over the surface element at latitude θ on the sphere is accounted for by the factor $\cos\theta$. The choice of the norm is contingent on the nature of physical attribute whose growth needs to be studied, consequently having a bearing on the stability results. While the choice of the norm is not unique, it is required to be positive definite. Using the norm chosen here which captures the squared sum of all the fields, the size of the perturbations can be naturally expressed. Notably, the analysis can be performed for different choices of other commonly used perturbation measures, such as the physical energy, kinetic energy, enstrophy etc. Using the the definition of the adjoint operator and the inner product in equation (3.4), the adjoint operator $\mathbf{M}^\dagger$ is found to be:

$$\mathbf{M}^\dagger = \begin{bmatrix} 0 & -\sin\theta & ik/(\cos\theta) \\ \sin\theta & 0 & D_\theta \\ ik/(\epsilon\cos\theta) & (1/\epsilon)(D_\theta - \tan\theta) & 0 \end{bmatrix}. \tag{3.5}$$

It can be readily shown that $\mathbf{M}^\dagger\mathbf{M} \neq \mathbf{M}\mathbf{M}^\dagger$.

A careful examination of the operator reveals that the value of ϵ determines whether we are working with a non-normal system or not. When $\epsilon = 1$, which gives us $\mathbf{M}^\dagger = -\mathbf{M}$, the operator is normal. However, this corresponds to a system with a very high equivalent depth ($H_0 = 88044$m), where it would not be justifiable to employ the framework of shallow water equations.

On the β-plane, we work the following inner product:

$$\langle \hat{\mathbf{q}}_i, \hat{\mathbf{q}}_j \rangle_\beta = \frac{1}{2} \int_{-\infty}^{\infty} dy \, (\hat{\mathbf{q}}_i^* \hat{\mathbf{q}}_j + \hat{\mathbf{q}}_j^* \hat{\mathbf{q}}_i). \tag{3.6}$$

Under this definition, the adjoint operator $\mathbf{M}_\beta^\dagger$ is:

$$\mathbf{M}_\beta^\dagger = \begin{bmatrix} 0 & -y & ik_\beta \\ y & 0 & D_y \\ ik_\beta & D_y & 0 \end{bmatrix}. \tag{3.7}$$

It is apparent that $\mathbf{M}_\beta$ is skew-Hermitian with $\mathbf{M}_\beta^\dagger = -\mathbf{M}_\beta$ [8]. Such operators have a complete set of eigenfunctions that are orthogonal to each other. As a result, in the absence of a mean shear flow, the β-plane is not a framework where non-normal behaviour can emerge. Therefore, the focus of the results in the subsequent will be on those pertaining to the spherical system.

3.2 Optimisation procedure

Having established that the spherical system is non-normal, we now have to find those perturbations that demonstrate significant non-normal behaviour. To this end, we need to identify a suitable measure of the perturbation for quantifying the extent of the non-normal behaviour. Often, the selected measure represents a physical attribute of the perturbation that involves all components of the state vector. While the choice of measure need not be unique, it is required to be positive definite.

For a state vector $\hat{\mathbf{q}}$, equation (3.4) implies that the norm is:

$$\|\hat{\mathbf{q}}\|^2 \equiv \langle \hat{\mathbf{q}}, \hat{\mathbf{q}} \rangle = \int_{-\pi/2}^{\pi/2} \mathrm{d}\theta \cos\theta \ \hat{\mathbf{q}}^* \hat{\mathbf{q}} = \int_{-\pi/2}^{\pi/2} \mathrm{d}\theta \ \cos\theta (\hat{u}^* \hat{u} + \hat{v}^* \hat{v} + \hat{h}^* \hat{h}). \tag{3.8}$$

In this study, consider initial conditions $\hat{q}_0$ that are combinations of a finite number of eigenfunctions of the linearised operator $\mathbf{M}$. The coefficient of $\tilde{\mathbf{q}}_j$ in the expansion of $\hat{\mathbf{q}}$ is denoted by $\hat{c}_j$, i.e., $\hat{\mathbf{q}}(\theta, t) = \sum_{i=1}^{l} \tilde{\mathbf{q}}_i(\theta)\hat{c}_i(t)$,. Each eigenfunction $\tilde{\mathbf{q}}_j$ oscillates with a specific temporal frequency ω_j. The IVP given by equation (3.1) can then be reduced to the evolution of the coefficients governed by:

$$\frac{\mathrm{d}\hat{\mathbf{c}}}{\mathrm{d}t} = \Lambda \hat{\mathbf{c}} \text{ and } \hat{\mathbf{c}}(0) = \hat{\mathbf{c}}_0 \Rightarrow \hat{\mathbf{c}}(t) = \exp(\Lambda t)\hat{\mathbf{c}}_\mathbf{0}, \tag{3.9}$$

$$\text{where } \hat{\mathbf{c}} = [\hat{c}_1 \ \hat{c}_2 \ \cdots \ \hat{c}_l]^T \text{ and } \Lambda = \mathrm{diag}\left(-i\,[\omega_1 \ \omega_2 \ \cdots \ \omega_l]^T\right). \tag{3.10}$$

As a result, we have:

$$\|\hat{\mathbf{q}}\|^2 = \hat{\mathbf{c}}^* \mathbf{P} \hat{\mathbf{c}} = \hat{\mathbf{c}}^* \mathbf{F}^* \mathbf{F} \hat{\mathbf{c}} = \|\mathbf{F}\hat{\mathbf{c}}\|_2^2, \tag{3.11}$$

$$\text{where } \mathbf{P}_{ij} = \langle \tilde{\mathbf{q}}_i, \tilde{\mathbf{q}}_j \rangle = \mathbf{F}^* \mathbf{F}.$$

By working with the 2-norm form given above, the computations are greatly simplified.

Starting with any initial condition $\hat{\mathbf{q}}_0 \equiv \hat{\mathbf{q}}(0)$, where the wavenumber is k, we can define the gain at time T as:

$$g(T; k) = \frac{\|\hat{\mathbf{q}}(T)\|^2}{\|\hat{\mathbf{q}}_0\|^2} = \frac{\|\mathbf{F}\hat{\mathbf{c}}(T)\|_2^2}{\|\mathbf{F}\hat{\mathbf{c}}_\mathbf{0}\|_2^2}. \tag{3.12}$$

In this study, this gain is chosen as the measure of interest to quantify non-normal perturbation behaviour, and we wish to find those initial conditions that maximise g. We postpone the discussion on the choice of the target time T to a later point. The optimal gain G is defined as:

$$G(T; k) \equiv \max_{\hat{\mathbf{q}}_0} g(T; k) = \max_{\hat{\mathbf{c}}_\mathbf{0}} \frac{\|\mathbf{F}\exp(\Lambda T)\hat{\mathbf{c}}_\mathbf{0}\|_2^2}{\|\mathbf{F}\hat{\mathbf{c}}_\mathbf{0}\|_2^2} = \|\mathbf{F}\exp(\Lambda T)\mathbf{F}^{-1}\|_2^2. \tag{3.13}$$

We use the singular value decomposition (SVD) to evaluate the norm in equation

(3.13). This yields the optimal growth G and the corresponding $\hat{\mathbf{c}}_\mathbf{0}$, which can be used to reconstruct the optimal initial condition ($\hat{\mathbf{q}}_0$) responsible for the amplification. Notably, G measures algebraic, finite-time growth resulting from non-normality, in contrast to exponential growth associated with unstable eigenmodes.

A key feature of the procedure outlined above is the state vector is expanded in terms of a set of eigenfunctions [80, 81]. While a variational problem could also have been employed to find initial conditions $\hat{\mathbf{q}}_0$ [82], it is not straightforward to determine the modes that end up contributing in the non-normal dynamics. The current approach appealingly grants us freedom to consider different combinations, and pinpoint which set of modes can act in concert to yield significant gain.

3.3 The eigenfunctions

Modal analysis of the linearised RSWE yields eastward (EIG) and westward inertio-gravity (WIG), mixed Rossby-gravity (MRG), Rossby and Kelvin modes as the eigenfunctions [8, 39]. For the sake of brevity, the reader is referred to Raghav *et al.* [53] for details of the numerical computation of the eigenvalues and the corresponding eigenfunctions. The perturbation wavenumber k is specified to take on integer values between 5 and 50, which covers dynamical regimes on the length scales of the planetary ($k \lesssim 10$), the synoptic ($k \sim 30$) and the mesoscale ($k \gtrsim 40$) . Additionally, note that every eigenfunction $\tilde{\mathbf{q}}_i$ is normalized such that $\|\tilde{\mathbf{q}}_i\|^2 = 1$.

For discussing the results to follow in a concise manner, it is useful to employ a system of nomenclature for the modes used in the construction of the non-normal perturbation. On the β-plane, with the exception of the Kelvin mode, the eigenfunctions are identified by the number of zeros of the meridional velocity component (n_v, also known as the meridional mode number) in addition to their wave family. However, on the sphere, this is no longer a viable option. We find that it is instead more suitable to use the number of zeros of the zonal velocity component (n_u). In the β-plane setting, it is to be noted that the relationship between n_u and n_v are: $n_u = n_v + 1$ for EIG, MRG and Rossby modes, and $n_u = n_v - 1$ for WIG modes.

The label used for identifying a mode alludes to the family to which it belongs and its n_u. WIG, EIG and Rossby modes are labelled as W_i, E_i and R_i respectively with the subscript $i \equiv n_u$. For convenience, we include the MRG mode in the

Rossby family and is identified as R_1. We consider the first five modes in each of the WIG, EIG and Rossby families in this study. While $n_u \in [1, 5]$ for the EIG and Rossby modes, the WIG modes have $n_u \in [0, 4]$. This is consistent with how the modes would have been labelled in the β-plane setting had n_u been used instead of n_v. Lastly, the Kelvin mode is denoted as 'Kel'. The meridional velocity of the Kelvin mode is very weak, and its zonal velocity does not change its sign at a given longitude ($n_u = 0$).

3.4 Perturbations comprising two modes

As a starting point, we first examine perturbations that are constructed from only two eigenfunctions $\tilde{\mathbf{q}}_1$ and $\tilde{\mathbf{q}}_2$. This exercise gives us valuable insight about which pairs of modes can yield notable gains, and can serve as a reference while building initial conditions from a larger number of modes. An immediate benefit of considering such a perturbation is that the number of the parameters to be explored drastically reduces.

At a given wavenumber k, a state vector constituted of only two modes is given by:

$$\hat{\mathbf{q}} = [\tilde{\mathbf{q}}_1\, \tilde{\mathbf{q}}_2] \begin{bmatrix} \hat{c}_1 \\ \hat{c}_2 \end{bmatrix} = \tilde{\mathbf{q}}_1 \hat{c}_1 + \tilde{\mathbf{q}}_2 \hat{c}_2 = \tilde{\mathbf{q}}_1 \hat{c}_1(0) e^{-i\omega_1 t} + \tilde{\mathbf{q}}_2 \hat{c}_2(0) e^{-i\omega_2 t}. \tag{3.14}$$

Using equation (3.14) in equation (3.8), and noting that $\|\tilde{\mathbf{q}}_1\|^2 = \|\tilde{\mathbf{q}}_2\|^2 = 1$, we get:

$$\|\hat{\mathbf{q}}\|^2 = |\hat{c}_1(0)|^2 + |\hat{c}_2(0)|^2 + 2\langle \hat{c}_1(0) e^{-i\omega_1 t} \tilde{\mathbf{q}}_1, \hat{c}_2(0) e^{-i\omega_2 t} \tilde{\mathbf{q}}_2 \rangle. \tag{3.15}$$

The last term alone on the RHS of equation (3.15) is a function of time and is given by:

$$\int_{-\pi/2}^{\pi/2} \mathrm{d}\theta \cos\theta \, \left[\hat{c}_1^*(0) \hat{c}_2(0) e^{-i(\omega_2 - \omega_1)t} \tilde{\mathbf{q}}_1^* \tilde{\mathbf{q}}_2 + \hat{c}_1(0) \hat{c}_2^*(0) e^{i(\omega_2 - \omega_1)t} \tilde{\mathbf{q}}_2^* \tilde{\mathbf{q}}_1 \right]. \tag{3.16}$$

From the above, it is evident that $\|\hat{\mathbf{q}}\|^2$ is periodic with a time period

$$T_p \equiv 2\pi / |\omega_2 - \omega_1|. \tag{3.17}$$

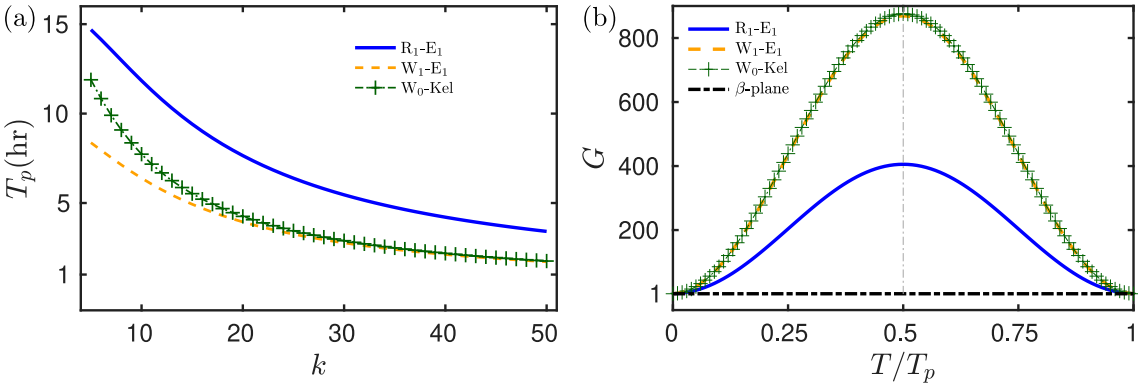

Figure 3.1: (a) The time period, T_p as a function of the wavenumber, k. Regardless of the combination of eigenfunctions, T_p reduces with k. (b) The gain G as a function of the scaled target time (T/T_p) for perturbations constructed with different eigenmode combinations; $k = 5$ for R_1-E_1, and $k = 50$ for W_1-E_1 and W_0-Kel. Note that G is maximum when $T = T_p/2$ for all combinations. For both (a) and (b), $H_0 = 100$ m.

This periodicity occurs as a result of the oscillatory nature of the modes which are governed by purely imaginary eigenvalues. Crucially, this behaviour is physically distinct from the standard nonmodal growth associated with systems whose eigenvalues have negative real parts. The perturbation gain in such systems undergoes initial transient amplification, reaching a single finite-time maximum before eventually decaying at a rate determined by the eigenvalue with the largest negative real part. T_p is shown in Fig. 3.1 (a) for representative pairs of counter-propagating eigenmodes as a function of k. For the range of k considered, T_p for combinations with a Rossby mode are typically much higher than other set of pairs.

As its time-dependent part is a single harmonic at frequency $\Delta_\omega = |\omega_2 - \omega_1|$, the largest departure of $\|\hat{\mathbf{q}}\|^2$ from its initial value occurs at $t = T_p/2$. Therefore, for perturbations comprising only two modes, we are presented with a natural choice for the target time T for finding optimal initial conditions. Fig. 3.1 (b) precisely highlights this fact. Regardless of the pair of eigenmodes selected to construct the optimal initial condition, the largest gain G is obtained when $T = T_p/2$. For all the results to follow in this section, the target time is fixed to be $T = T_p/2$. To proceed

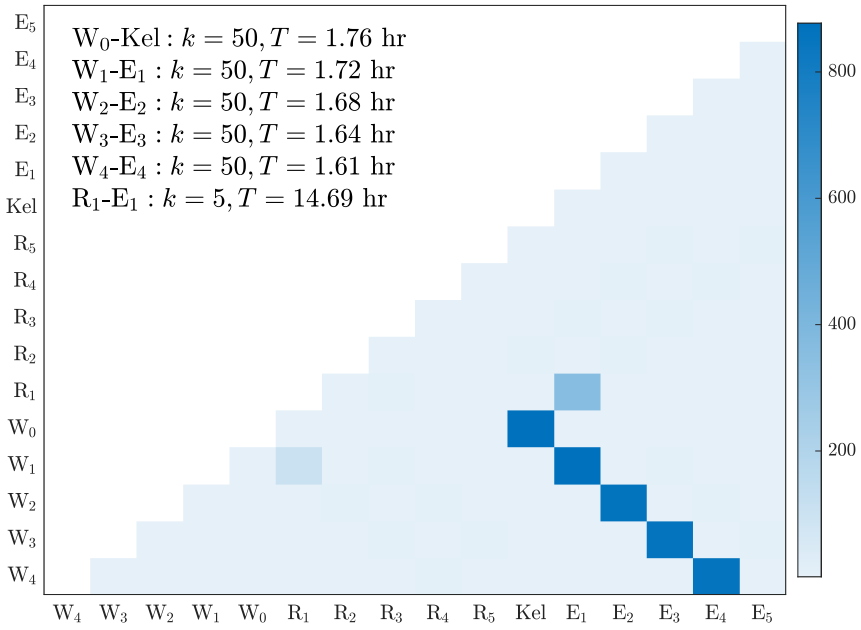

Figure 3.2: Maximum non-normal gain ($\mathcal{G}_m$) is shown for different eigenmode combination pairs. We find perturbations comprising counter-propagating eigenmodes (e.g. W$_0$-Kel, R$_1$-E$_1$, W$_1$-E$_1$) undergoing significant non-normal growth. This is not the case for perturbations constructed with co-propagating modes. For the combinations that yield considerably large values of $\mathcal{G}_m$, the corresponding values of k and T_p are provided.

with the discussion, we define the following:

$$\mathcal{G}_m = \max_k \mathcal{G}, \tag{3.18}$$

$$\text{where } \mathcal{G}(k) \equiv \max_T G(T;k) = G(T_p/2;k). \tag{3.19}$$

We wish to examine how large the gain becomes for initial conditions comprising different pairs modes across a wide range of k.

Fig. 3.2 shows $\mathcal{G}_m$ for non-modal perturbations comprising of different eigenmode pairs for a typical equivalent depth $H_0 = 100$ m ($\epsilon = 880.44$). Curiously, significant growth is observed only for a few perturbations constructed with a pair of counter-propagating modes. These have been highlighted in the figure, and will be the focus of the subsequent discussion. Henceforth, note that we label the perturbation based on the two modes used for its construction. We report that significant growth occurs within a short period of time (less than an hour) for those perturbations

comprising only the faster propagating modes (e.g., W_0-Kel, W_1-E_1, and W_2-E_2). Such growth is more pronounced at larger wavenumbers. In contrast, R_1-E_1 exhibits larger growth at lower wavenumbers and the amplification occurs over a longer period of time ($>$ 10 hours). While Fig. 3.2 provides a general idea of the extent of non-normal behaviour, we will now examine more closely the effect of changing the perturbation wavenumber k and the equivalent depth H_0. To this end, we will focus on three specific perturbations: W_1-E_1 (representative of perturbations constructed from WIG-EIG pairs), W_0-Kel and R_1-E_1.

The dependence of the gain $\mathcal{G}$ on the wavenumber when $H_0 = 100$ m ($\epsilon = 880.44$) is shown in Fig. 3.3 (a). For all the perturbations, the growth is highly sensitive in the low-to-moderate wavenumber range ($k \in (1, 30)$). For R_1-E_1, $\mathcal{G}$ is considerable at planetary scales ($k < 10$)) before dropping sharply till synoptic scales ($k \sim 30$). This is followed by a gradual decay beyond mesoscales ($k \gtrsim 40$), where the amplification experienced by the perturbations may be deemed insignificant. This is in complete contrast to W_0-Kel and W_1-E_1 where the gains increase with k. At higher wavenumbers, the values of $\mathcal{G}$ approaches ϵ from below. In other words, ϵ appears to provide an upper bound for $\mathcal{G}$ for these perturbations. It should be emphasised that the optimisation is carried out using the norm, which does not include ϵ. In the physical energy norm, ϵ enters in the denominator of the potential energy term, where it has been verified that the non-normal growth is not observed. The choice of norm yields the initial condition which can experience non-normal growth. The subsequent evolution is purely physical, governed by RSWE on sphere.

To examine the effect of the equivalent depth of the shallow layer (or equivalently, ϵ), we focus on the perturbations that give largest value of $\mathcal{G}$ in Fig. 3.3 (a). This leads us to fix $k = 5$ for R_1-E_1, and $k = 50$ for W_0-Kel and W_1-E_1. On increasing H_0, as seen in Fig. 3.3 (b), $\mathcal{G}$ decreases for all perturbations without exception. More strikingly, $\mathcal{G}$ appears to be directly proportional to ϵ for all the perturbations. In fact, the differences between $\mathcal{G}$ and ϵ are nearly imperceptible for W_0-Kel and W_1-E_1. Therefore, these results suggest that the equivalent depth can also quantitatively prescribe the importance of non-normal dynamics, or lack thereof.

Now we turn our attention to the structure of the perturbations at different time instances over the course of their evolution. While comparing different snapshots, it is necessary that the visualisation is unambiguous. For a given initial condition,

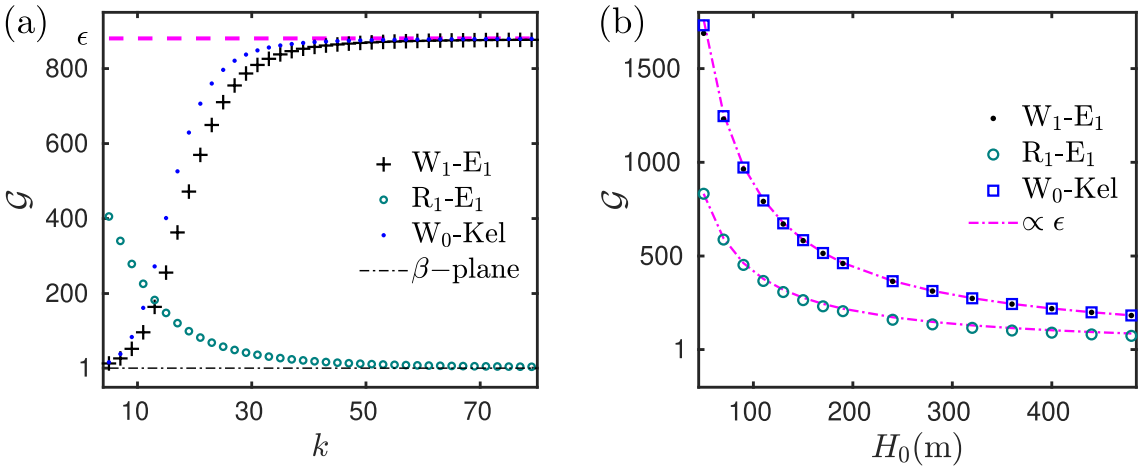

Figure 3.3: (a) $\mathcal{G}$ as a function of wavenumber k when $H_0 = 100$m. While $\mathcal{G}$ increases with k for W$_0$-Kel and W$_1$-E$_1$, the opposite trend is seen for R$_1$-E$_1$. (b) $\mathcal{G}$ as a function of equivalent depth H_0 for R$_1$-E$_1$ (with $k = 5$), and for W$_1$-E$_1$ and W$_0$-Kel (with $k = 50$). All the curves in panel b appear to be proportional to ϵ.

we identify the largest value of the geopotential field on the latitude and longitude grid over the course of its evolution:

$$h_* = \max_{\theta,\phi,t} h(\theta,\phi,t) = \max_{\theta,\phi,t} \frac{1}{2}\left[\hat{h}(\theta,t)\exp(ik\phi) + \hat{h}^*(\theta,t)\exp(-ik\phi)\right]. \tag{3.20}$$

h_* is used to normalise the height field for all the snapshots; it turns out that h_* is obtained when $t = T_p/2$ for all the perturbations under consideration. For visualising the velocity, we use an independent normalisation procedure. At each instant, the largest magnitude of the velocity ($l = l(t)$) is used for normalisation. To compare velocity vectors at different times, we evaluate $L = \max_t l(t)$ and l is given as a fraction of L; as we are working with a linear system, we set $L = 1$ without loss of generality.

As the perturbation energy evolves in a periodic fashion, it suffices to focus on the time window $t \in [0, T_p]$. The specific times that we consider are: $t = 0$, $t = T_p/4$, $t = T_p/2$, $t = 3T_p/4$ and $t = T_p$. Fig. 3.4 shows the perturbation structure R$_1$-E$_1$, W$_0$-Kel, and W$_1$-E$_1$ at these times when $H_0 = 100$ m; the perturbation wavenumbers are 5, 50 and 50 for R$_1$-E$_1$, W$_0$-Kel and W$_1$-E$_1$, respectively. The different panels show the velocity vector and the geopotential field at the selected times.

Several common features are observed in all the perturbations. At $t = 0$, all the

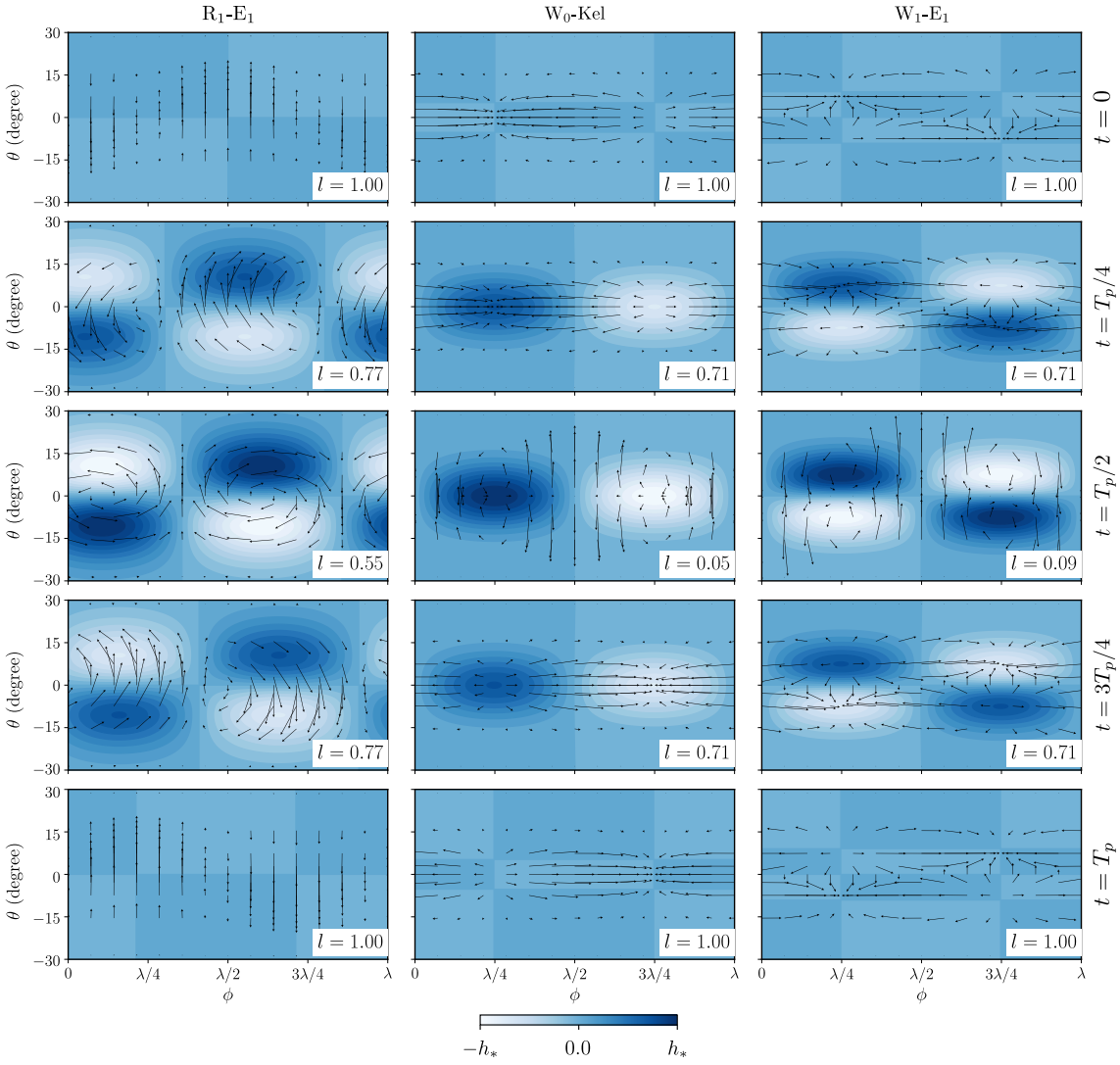

Figure 3.4: Time evolution of optimal initial condition leading to the growth of systems with different pairs. Arrows depict the velocity and colour contours depict the surface elevation. The magnitude of velocity relative to the maximum velocity (denoted by l) is shown for each case. The colorbar depicts the range of height field from its minimum (-h_*) to maximum (h_*) value during the evolution. The analysis is performed for $k = 50$ for W_0-Kel and W_1-E_1 (middle and right panel) and $k = 5$ for R_1-E_1 (left panel) case. $T_p = 14.69\text{hr}, 1.76\text{hr}, 1.72\text{hr}$ for R_1-E_1, W_0-Kel and W_1-E_1, respectively.

perturbations can be characterised by a very weak geopotential and predominant velocity fields. This can be understood by having a closer look at the contributing eigenmodes. The two eigenmodes combine in such a way that their velocity fields reinforce each other, such the net velocity of the optimised perturbation remains strong. In contrast, the geopotential components of these modes have nearly opposite spatial structures–peaks of one align with troughs of the other. As a result, their contributions largely cancel when superposed, producing a very weak total geopotential field. $\|\hat{\mathbf{q}}\|^2$ increases from the initial instant till it reaches its peak value at $t = T_p/2$, and then proceeds to decrease until $t = T_p$. For all perturbations, the non-normal growth observed is primarily tied to the enhancement of the perturbation geopotential over time. In contrast, we observe that the velocity fields decrease in strength between $t = 0$ and $t = T_p/2$. The trend is reversed when $t \in [T_p/2, T_p]$. During this period, while the velocity field starts gaining in strength, the geopotential field becomes weaker. The perturbation at $t = T_p$ is a phase-shifted version of the initial condition, which leads to a repeat of the cycle described.

We now look at specific perturbations, starting with R_1-E_1 (left column in Fig. 3.4). The velocity field for R_1-E_1 is principally meridional at $t = 0$. While $t < T_p/2$, vortical features emerge and become the prominent characteristic of the perturbation's velocity field. The geopotential fields have off-equatorial peaks and troughs that get amplified in time. At $t = T_p/2$, when the magnitude of the geopotential field is maximum, the velocity field is characterised by a predominantly equatorial vortex. As the perturbation evolves further till $t = T_p$, the vortical structure and the geopotential field weakens. The velocity field ultimately returns to its initial form at $t = T_p$ where the zonal component is negligible, albeit with a phase-shift in the longitudinal direction.

For W_0-Kel and W_1-E_1 (middle and right columns in Fig. 3.4), it is useful to look at the geopotential and velocity fields together. When $t < T_p/2$, the convergence and divergence zones correspond to the regions where the geopotential increases and decreases, respectively. At $t = T_p/2$, the maximum magnitude of the geopotential field is observed. Additionally, note that there is a significant drop in the strength of the velocity field from its initial state. Beyond $T_p/2$, the velocity field reverses sign everywhere. As a result, the regions that showed maximum convergence at $t = 0$ now experience maximum divergence, and the corresponding geopotential anomalies

begin to diminish. This weakening continues until $t = T_p$, when the geopotential recovers its initial amplitude. These features are observed for perturbations identified from other WIG-EIG pairs as well.

3.5 Perturbations constructed from more than two modes

While the results from the previous section revealed the scope for non-modal dynamics, the perturbations were found under the restrictive condition that they be constructed from only two eigenmodes. We shall now consider the case where a larger number of eigenfunctions is included in the basis. The focus will be on how large the gains can become for different choices of the eigenfunction basis and the perturbation wavenumber.

The main benefit of constructing initial conditions from two eigenmodes is the straightforward choice for the optimisation time. When the basis comprises more than two eigenmodes, we no longer have such a convenient option. There is a need to explore a sufficiently wide range of target times. Furthermore, unlike in the previous section, we can no longer predict a priori when the gain will be maximum. For any given basis, let $T_{p,min}$ and $T_{p,max}$ be the minimum and maximum values of the values of T_p of all eigenmode pairs. The target time for optimisation is varied between $0.25T_{p,min}$ to $3T_{p,max}$. Although arbitrary, this choice may be believed to cover the physical range. The initial conditions obtained via the SVD procedure are evolved for sufficiently long period, within which the largest value of g (defined in eq. 3.12) is recorded. We report that recording the evolution of the perturbation over a period of three days (around 37.7 non-dimensional time units) is sufficient for our purpose. Of all the initial conditions obtained for different target times, we pinpoint the one yielding the largest amplification (denoted by $\mathcal{G}_*$) and discuss its characteristics. While $\mathcal{G}_* = \mathcal{G}$ for the perturbations constructed from two eigenfunctions, it will generally not be so for the perturbations considered in this section.

Our aim in this chapter is not to get the maximum energy growth possible, for which we would just automatically include all the modes and conduct an SVD, but the idea is to examine the different families of modes, and see how interactions between them will affect algebraic growth. This was the reason we chose two modes at a time from different families in the above section, and here we include multiple

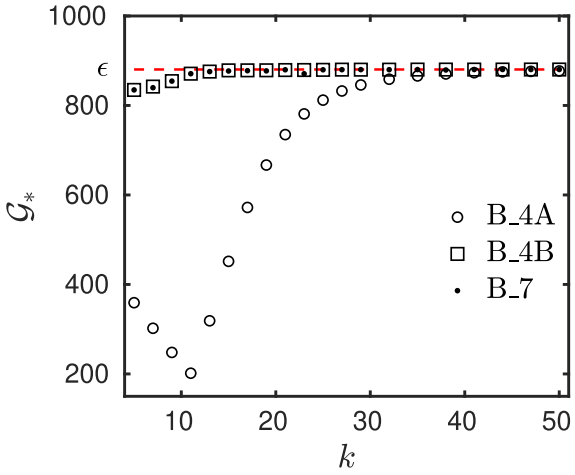

Figure 3.5: Maximum Gain ($\mathcal{G}_*$) as a function of wavenumber (k) for perturbations with different combinations of modes, as specified in table 3.1. Note that $\mathcal{G}_*$ never exceeds the value of ϵ.

modes but still in small numbers, and ensure that modes from different families are included in each choice. The choice of eigenfunctions included in the basis will naturally play a vital role. While requiring that every basis considered comprise at least one mode each from the WIG, Rossby, and EIG families in addition to the Kelvin mode, we explore several combinations of the eigenfunctions. In the interest of brevity, the primary focus will be on perturbations constructed from the three bases given in table 3.1; as before, the perturbation will be labelled by the basis used. While B_4A and B_4B comprise four modes each, they only differ in the choice of Rossby and EIG modes. B_7 is simply the combination that includes all the modes included in B_4A and B_4B.

Basis	**WIG**	**Rossby**	**Kelvin**	**EIG**
B_4A	W_0	R_1	Kel	E_1
B_4B	W_0	R_2	Kel	E_2
B_7	W_0,W_1	R_1, R_2	Kel	E_1, E_2

Table 3.1: Constituent modes in different sets of basis used for constructing non-modal perturbation.

Fig. 3.5 shows the maximum amplification $\mathcal{G}_*$ perturbations constructed from the three bases attain as a function of the wavenumber k. $\mathcal{G}_*$ for B_4A initially decreases till $k = 11$ before the trend reverses. Noting the eigenfunction basis yielding B_4A,

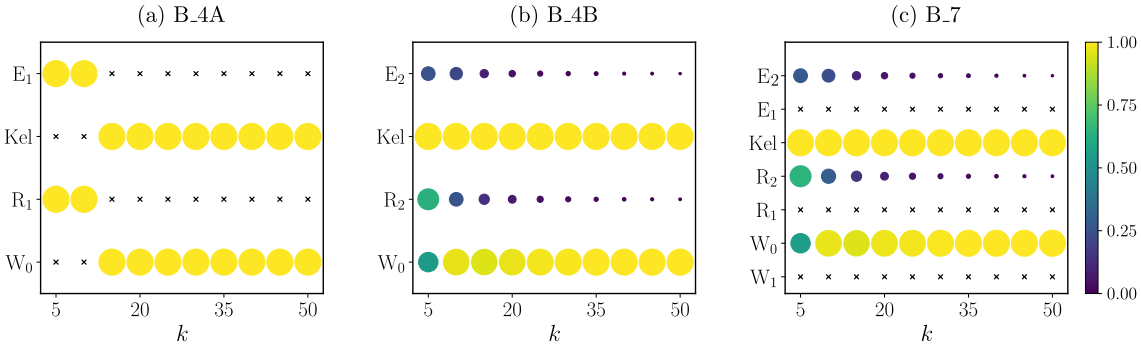

Figure 3.6: Contribution of different eigenfunctions in non-modal perturbations as a function of the wavenumber k. The size and the colour of the circles depict the relative magnitude of the eigenfunction coefficients. In the plots, the symbol 'x' indicates that the coefficient of the eigenfunction is zero. Note that the wavenumbers are varied in steps of five starting with $k = 5$.

on comparing with Fig. 3.3 (a), its $\mathcal{G}_*$ resembles a combination of the curves of $\mathcal{G}$ for the non-modal perturbations R_1-E_1 (for $k \leq 11$) and W_0-Kel (for $k > 11$). On the other hand, the values of $\mathcal{G}_*$ for B_4B and B_7 are close to ϵ for the entire range of k. In particular, the amplification for B_4B and B_7 is much higher than that of any perturbation considered for low k (see section 3.4). For larger k, the values of $\mathcal{G}_*$ approach, but do not exceed, ϵ for all perturbations. This is similar to what we saw in the last subsection for perturbations constructed with two modes.

It is clear that significant amplifications can also be observed for non-modal perturbations constructed from several modes. However, the question remains as to how much individual eigenmodes contribute. We will address this matter now by examining the coefficients in the initial condition given by the optimisation procedure. To be more precise, we compare the magnitude of the coefficients of the different eigenmodes at $t = 0$ for a given basis. As the eigenmodes are normalised in identical fashion, this gives us a firm handle of their contribution.

The relative magnitudes of the coefficients of the different eigenfunctions are shown in Fig. 3.6. For B_4A perturbations, it is striking that, within our choices, each time, only two eigenfunctions contribute at any given k. In other words, these perturbations are no different from those considered in section 3.4. We now have a clearer explanation for the $\mathcal{G}_*$ curve for B_4A (see Fig. 3.5) resembling a combination of $\mathcal{G}$ curves of R_1-E_1 and W_0-Kel. The initial dip in $\mathcal{G}_*$ at low k resembles

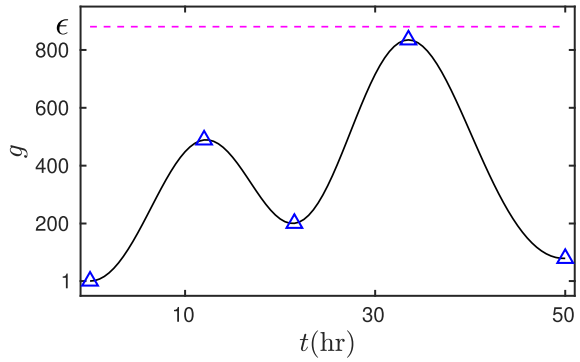

Figure 3.7: Gain as a function of time for the perturbation B_4B with $k = 5$ (table 3.2). The blue triangles represent the local extrema in g shown at $t = 0, T_1, T_2, T_3, T_4$, respectively; the corresponding perturbation structures at these times can be seen in Fig. 3.8.

the behaviour seen in R_1-E_1 case followed by increasing $\mathcal{G}_*$ associated with W_0-Kel at large k. We now consider perturbations B_4B and B_7, which undergo much higher amplification than B_4A. It is notable that the constructions of the perturbations are nearly identical for B_4B and B_7. The coefficients of the additional eigenmodes (W_1, R_1 and E_1) in B_7 are zero. We report this to be the case even when more eigenmodes are included in the basis with the optimisation procedure yielding the same initial condition (not shown).

Now we will discuss how the contributions change when the wavenumber is varied. From Fig. 3.6, we are again presented with the scenario that the contribution to the perturbation is dominated by two modes at higher wavenumbers. This provides justification for performing the analysis using only two modes in section 3.4 when k is large. But the picture is quite different at lower wavenumbers. Four modes end up combining to give the perturbation (Fig. 3.6 (b) and (c)), which in turn is responsible for $\mathcal{G}_*$ being greater than the gain seen for any perturbation constructed using only two eigenfunctions.

When the wavenumber is large, the preceding discussion demonstrated that the perturbations that undergo significant amplification are mainly constructed from two eigenfunctions. The principal characteristics of the perturbation structure mirror those shown in section 3.4. This is not the case with perturbations with low wavenumber. Let us consider the perturbation B_4B for $k = 5$. In Fig. 3.7, the gain is plotted as a function of time. It is characterised by irregular oscillations in

Basis	**Explicit form**
R_1-E_1	$\hat{\mathbf{q}}$ = -9.4894 R_1 - 9.4894 E_1
B_4B	$\hat{\mathbf{q}}$ = (-7.8712 + 0.8377i)W_0+(6.8627-6.0982i)R_2 +(6.3492+12.7936i)Kel+(1.2762 - 3.66

Table 3.2: Explicit form of the perturbations constructed using optimal coefficients obtained from the SVD, shown for different choices of basis functions at wavenumber $k = 5$.

time marked by several local extremas. On extending the observation window, we report that more local extrema are seen. The perturbation structures, corresponding to the extrema highlighted in Fig. 3.7, are shown in Fig. 3.8. At $t = 0$, the perturbation is characterised by strong equatorial zonal wind associated with convergence and divergence zones located along the equator. As before the amplitude of the imposed geopotential field is negligible in the initial perturbation. With time, the convergence and divergence zones lead to the amplification and suppression of geopotential inducing anticyclonic and cyclonic vorticity, respectively. At the time when g in Fig. 3.7 reaches its first maximum ($t = T_1$), the evolved perturbation exhibits large geopotential anomalies located precisely where the combined velocity field produces strong equatorial convergence. These convergence regions are accompanied by off-equatorial vortical structures, which arise as the meridional flow adjusts to the intensified equatorial inflow. The resultant velocity, having the features of a saddle point, lead to the subsequent decay of geopotential till it becomes negligible at the time of second minima in g ($t = T_2$). The convergence zone at $t = T_2$ facilitates the eventual amplification of geopotential leading to the highest non-normal growth experienced at $t = T_3$. At this time, the velocity field reverses, and the geopotential anomalies in these regions begin to weaken. By ($t = T_3$), the perturbation has returned to the same spatial pattern it had initially, except with an overall phase shift.

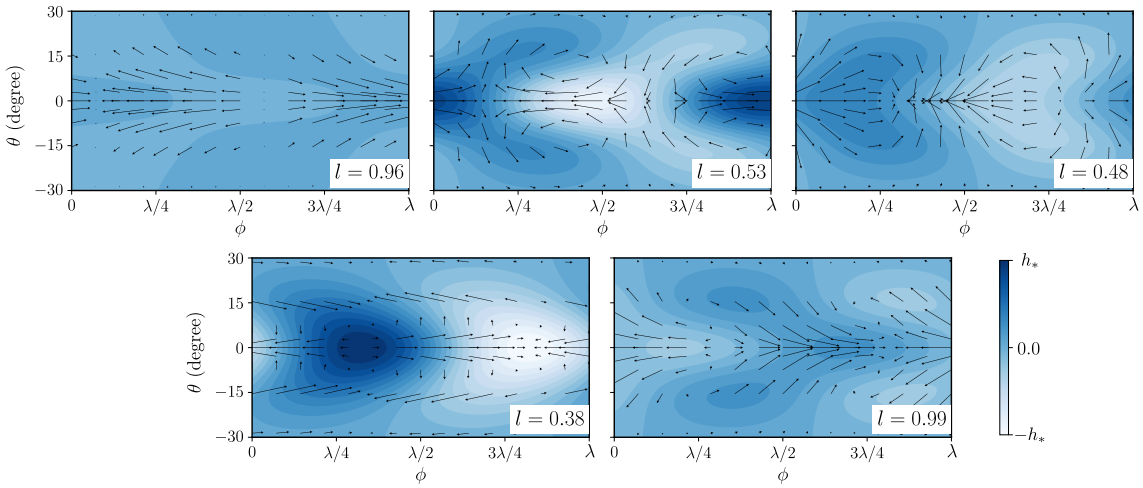

Figure 3.8: Time evolution of the perturbation B_4B when $k = 5$ (table 3.2). Arrows depict the velocity and colour contours depict the surface elevation. The magnitude of velocity relative to the maximum velocity (denoted by l) is shown for each case. The colorbar depicts the range of height field from its minimum ($-h_*$) to maximum (h_*) value during the evolution. The snapshots correspond to the times highlighted in Fig. 3.7.

3.6 Conclusion

This study investigates the non-normal behaviour of the linearised RSWE about a state with no mean flow on the sphere. The governing linearised operator on the β-plane is normal. As a result, there is no scope for non-normal behaviour, which highlights a shortcoming of the β-plane system. In contrast, the corresponding governing operator on the sphere is non-normal, leading to a scenario where non-normal growth of perturbations is possible even in the absence of a mean shear flow. The value of the Lamb parameter (ϵ) determines the degree of the non-normality of the system.

We identify perturbations constructed by various combinations of eigenfunctions which exhibit significant non-normal growth. Evidently, the Lamb parameter provides an upper bound to the growth. Within our range of investigation, we find that in the high wavenumber ($k \in (30, 50)$) range, two modes are sufficient to capture the significant non-normal growth of the system. For these cases, only for the pairs with counter-propagating modes used for the construction, the perturbations undergo considerable growth. At low wavenumber ($k \in (10, 30)$), however, addi-

tional modes contribute in the construction of perturbations. At the initial time, the perturbations exhibit weak geopotential. As the geopotential components of the two contributing eigenmodes are nearly out of phase with each other, their contributions interfere destructively and produce a small net geopotential field even though the modal amplitudes themselves are not small. The subsequent evolution of these initial conditions is marked by significant amplification of the geopotential field. In all cases, this amplification of the geopotential field is closely linked with the non-normal growth.

The underlying assumptions and methods employed in the current study naturally pose some limitations to their applicability to realistic scenarios. The shallow water approximation neglects the variation of the vertical structure of the atmosphere. The dry shallow water framework, while conceptually powerful, neglects the full vertical structure of the atmosphere and omits key physical processes such as moist convection, diabatic heating, frictional effects, and topographic influences. Additionally, the impact of mean shear flow on non-normal behaviour remains unexplored. Finally, the analysis is linear, which is applicable for time scales during which the perturbations are small. As a result of non-normality, we observe the amplification of perturbations in time scales where the suitability of linearity is questionable. It will be interesting to study the role of non-linearity over such time scales by studying the evolution of the perturbations yielding the observed significant growth in the framework of non-linear RSWE on a sphere.

Chapter 4

Nonlinear Analysis

The results presented in this chapter have been generated with the help of codes developed by Prof. Jai Sukhatme to solve RSWE on the sphere in vorticity-divergence form. In particular, he developed the spherical harmonic transform infrastructure, which implements forward and inverse spectral transforms, the computation of wind components from vorticity and divergence, and the evaluation of gradient operators using the SHTns library.

4.1 Description of the system and framework

In the preceding chapters, the linear dynamics of equatorial shallow water flows was examined in detail, both in the presence and absence of background shear. While linear theory provides a foundation for understanding wave propagation and transient amplification, it cannot describe the subsequent saturation and redistribution of energy once perturbation amplitudes become finite. In the nonlinear regime, a rich dynamical behaviour including wave-wave and wave-mean flow interactions govern the redistribution of energy among different spatial and temporal scales and mediate the feedback between eddies and the mean flow [1, 36]. Finite-amplitude waves can interact through quadratic nonlinearity, exchanging energy among resonant triads. These interactions underlie the spectral transfer processes that lead to energy cascades and the formation of coherent large-scale structures [83, 84]. Additionally, nonlinear Reynolds stresses associated with wave activity can accelerate or decelerate the zonal mean flow, leading to the emergence of alternating jets or oscillations such as the QBO [85, 86]. Nonlinearity determines whether initial transient amplification identified in the linear framework can trigger sustained nonlinear evolution, possibly leading to secondary instabilities [1], wave breaking, or the

spontaneous generation of zonal flows [87]. Doing nonlinear dynamics is crucial for understanding whether the transiently amplified perturbations saturate into steady patterns, evolve into intermittent bursts, or transition to chaotic behaviour [49, 88].

This chapter extends the investigation beyond the linear regime to examine the perturbation evolution under the nonlinear inviscid RSWE on the sphere. The fully nonlinear shallow water equations (2.1) are solved, subject to initial condition $(u(\theta,\phi,0),\ v(\theta,\phi,0),\ h(\theta,\phi,0)) = (u_0,\ v_0,\ h_0)$. The analysis is performed on a sphere which is why the subscript (s) in the equations in (2.1) is dropped for simplicity. For the purpose of analysis, the state vector in the nonlinear setting is decomposed into a longitudinally averaged field ($\bar{\mathbf{q}}(\theta,t)$) and the perturbation field ($\mathbf{q}'(\theta,\phi,t)$) as,

$$\mathbf{q}_0(\theta,\phi,t) = \bar{\mathbf{q}}(\theta,t) + \mathbf{q}'(\theta,\phi,t). \tag{4.1}$$

In particular, we set out to investigate the effects of nonlinearity on the propagation and structure of optimal perturbations identified in the linear non-normal analysis.The system is initialised by specifying $\bar{\mathbf{q}}(\theta,0) \equiv [\bar{u}\ \bar{v}\ \bar{h}] = [0,0,H_0]$ which accounts for the state of zero mean flow and scaling the perturbations by an amplitude A, such that,

$$[u_0,\ v_0,\ h_0] = [0 + Au'(\theta,\phi), 0 + Av'(\theta,\phi), H_0 + Ah'(\theta,\phi)]. \tag{4.2}$$

By systematically varying A, which controls the perturbation strength, the transition of the system from linear (small A) to finite-amplitude, nonlinear regime (large A) can be explored. The details of numerical method employed are discussed in Appendix C.

4.2 Nonlinear Evolution of optimal initial conditions

The optimal perturbations which exhibit considerable non-normal growth in the linear regime were identified in the previous chapter. Here we wish to assess how the behaviour of these optimal perturbations is modified when perturbation amplitude A is finite. To begin with, we consider the optimal perturbation constructed from the combination of MRG and R_1 modes (R_1-E_1) as discussed in section 3.4. The

explicit form of the perturbations analysed here is shown in table 3.2. This perturbation is shown (top left panel in figure 3.4) for $k = 5$, having dominant meridional velocity field and weak geopotential anomaly. Figure 4.1 shows its evolution for two intermediate values of A and compares it against a negligible amplitude ($A = 10^{-8}$) which mimics the linear evolution. Even in the weakly nonlinear regime ($A = 0.05$), the influence of nonlinear interactions is visible in the evolution. While the nonlinearly evolved fields have broad qualitative features of their linear counterparts, the geopotential anomalies grow more rapidly and attain larger meridional extent with time. Additionally, although a vortical pattern still forms around $t \sim 14$ hr, the velocity field too exhibits pronounced latitudinal extent. The subsequent evolution clearly departs from recurrence observed in the linear regime and settles to a state with meridionally elongated equatorial vortices and weak off-equatorial geopotential field. On further increasing the amplitude ($A = 0.1$), the deformations in the velocity and geopotential field are much more rapid, exhibiting irregularities not present at lower amplitudes. Instead of amplifying into the symmetric off-equatorial lobes, the geopotential spreads into highly distorted, latitudinally asymmetric structure with steeper crests and troughs. The velocity field transitions from the initial meridional pattern into persistent deformed equatorial vortex with larger meridional elongation.

In the linear regime, the non-normal growth of perturbations was quantified using the measure defined in eq. 3.8. In the nonlinear setting, we work with a generalised version of this quantity and define the perturbation measure as,

$$\|\mathbf{q}'(t)\|^2 = \int_0^{2\pi} \mathrm{d}\phi \int_{-\pi/2}^{\pi/2} \mathrm{d}\theta \, \cos\theta (u'(\theta,\phi,t)^2 + v'(\theta,\phi,t)^2 + h'(\theta,\phi,t)^2). \tag{4.3}$$

To analyse the gain in the measure experienced by the perturbation, we define

$$\mathrm{G\_pert}(t) = \frac{\|\mathbf{q}'(t)\|^2}{\|\mathbf{q}'(0)\|^2} \tag{4.4}$$

Figure 4.3 (left panel) illustrates the perturbation gain (G_pert) for the E_1-R_1 pair for different values of A. In the linear regime ($A = 10^{-8}$), the gain displays a clear periodic oscillation with a well-defined period (T_p), consistent with the definition in (3.17). For finite-amplitude perturbations, the early-time evolution re-

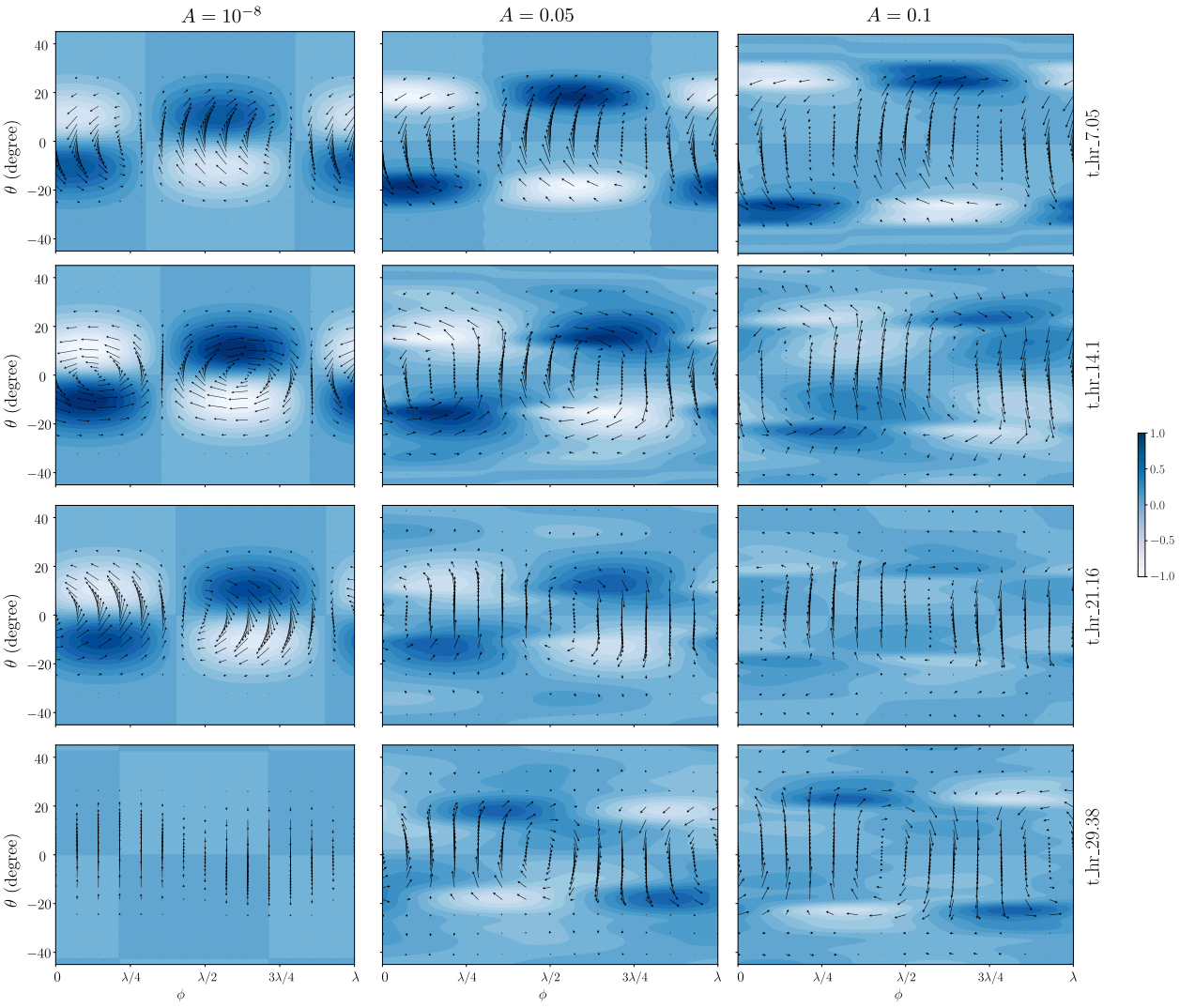

Figure 4.1: Time evolution of optimal initial condition leading to the growth of R_1-E_1 for Linear (left) and finite values of initial amplitude (middle and right). Arrows depict the velocity and colour contours depict the surface elevation. The analysis is performed for $k = 5$.

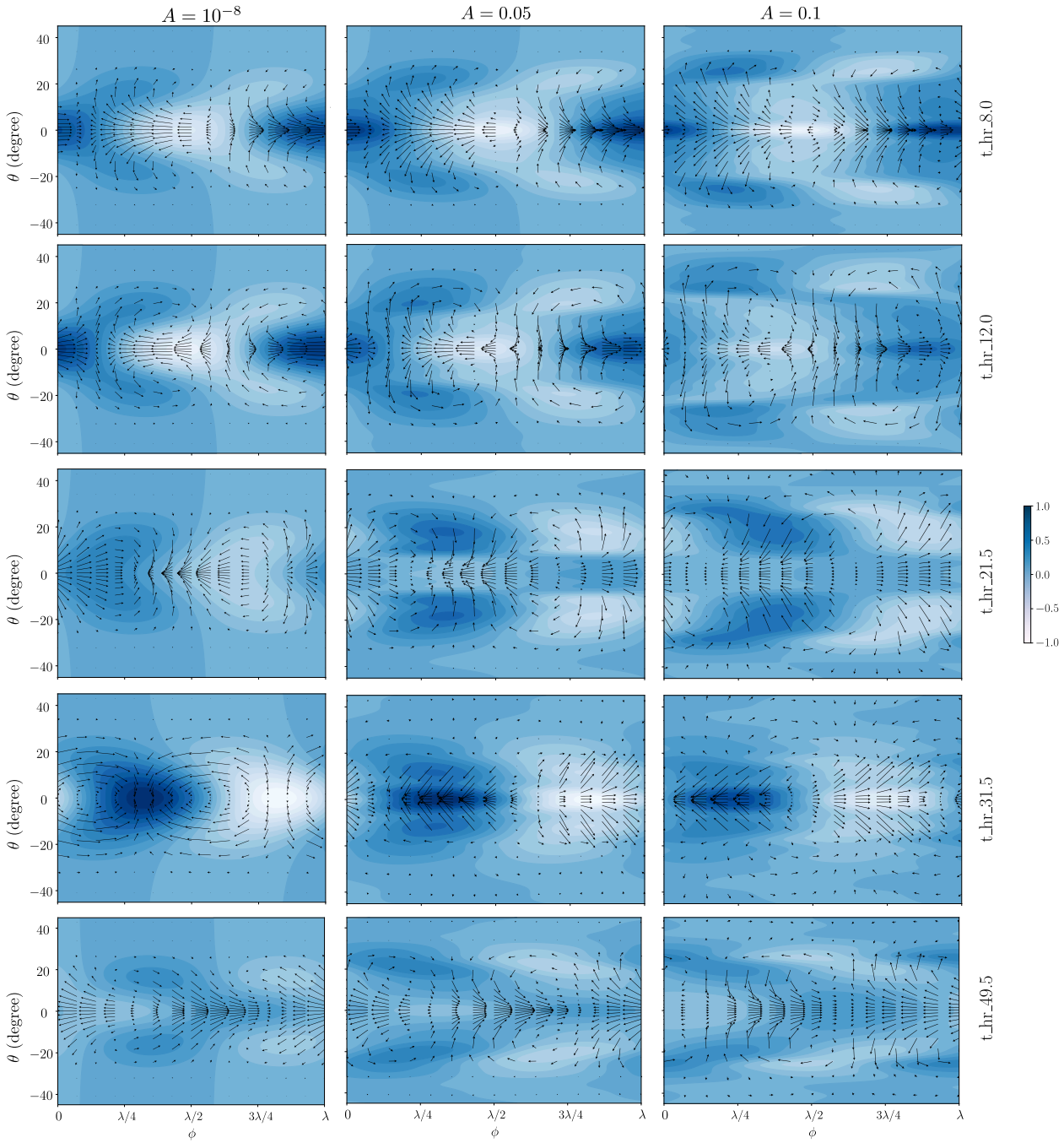

Figure 4.2: Time evolution of optimal initial condition leading to the growth of B_4B for linear (left) and finite values of initial amplitude (middle and right). Arrows depict the velocity and colour contours depict the surface elevation. The analysis is performed for $k = 5$.

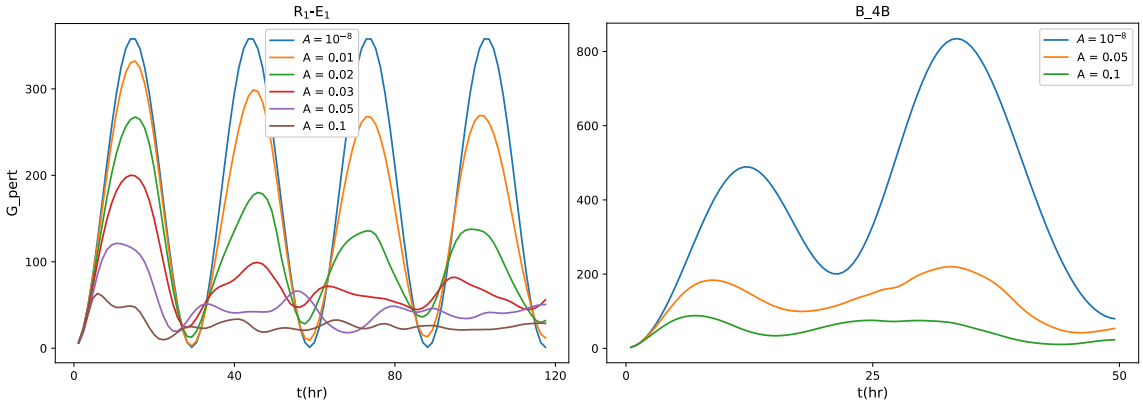

Figure 4.3: Perturbation gain (G_pert) in the linear regime ($A = 10^{-8}$) compared to the intermediate values of initial perturbation amplitude A for R_1-E_1(left) and B_4B for (right).The results in the left panel are shown for a larger range of A to demostrate the systematic effect of increasing the strength of nonlinearity in weakening the maximum gain acheived by the perturbations. The analysis is performed for $k = 5$.

mains close to the linear prediction, such that over an initial time window of a few hours, the perturbation gain in the nonlinear system closely follows that of the linear dynamics. However, as the perturbation amplitude grows through non-normal amplification, nonlinear effects become significant and the evolution progressively departs from its linear counterpart. This departure occurs earlier as the strength of nonlinearity increases with (A), leading to a reduction in the duration of the initial agreement. Moreover, relative to the linear case, the maximum gain attained by the perturbation is reduced for finite (A), with stronger suppression at larger amplitudes. At later times, this nonlinear influence manifests as a gradual weakening of the oscillatory behaviour of the gain. The results in this case are shown for a range of values of initial amplitude showing gradual gradual weakening of the maximum gain attained by the perturbations.

Next we consider the optimal initial condition constructed from W_0, Kel, R_2 and E_2 (B_4B in table 3.2). It is shown in the first panel of figure 3.8 for $k = 5$ to be characterised by strong equatorial zonal wind associated with convergence and divergence zones located along the equator. Figure 4.2 shows its evolution for different values of A. With increasing amplitude A, departures from the linear evolution become evident during the first few snapshots. At the first snapshot

(t = 8hr), predominant geopotential anomaly is located along the equator in the linear regime ($A = 10^{-8}$). For higher A, it gets modified by the presence of secondary geopotential peaks which extend to higher latitudes. The accompanying circulation spans larger meridional extent as well compared to the linear case. With time, the off-equatorial geopotential anomalies for intermediate A broaden meridionally and progressively migrate towards the equator before merging across the equatorial region around t = 31.5 hrs. Right panel of figure 4.3 shows perturbation gain for B_4B for different values of A. As observed in the R_1-E_1 pair, the system deviates faster from its linear counterpart with increasing A. The observed peaks in gain in the linear regime gets significantly suppressed with increasing perturbation amplitude.

4.3 Summary and Conclusion

In this chapter, we examined the nonlinear evolution of optimal perturbations in the inviscid RSWE, with particular emphasis on equatorial wave dynamics in the absence of a mean flow. The results demonstrate that, for sufficiently small but finite perturbation amplitudes, the early-time evolution closely follows the linear prediction. As the perturbation amplitude is increased, nonlinear interactions progressively modify the evolution. The window of agreement with linear dynamics shortens, the maximum gain achieved by the perturbations is suppressed relative to the linear case, and the periodic oscillations in perturbation growth weaken with time. Spatially, nonlinear effects manifest as a meridional spreading of both geopotential and circulation anomalies. Together, these results illustrate how nonlinearity regulates the perturbation growth and structure.

Despite these insights, the present study is subject to several important limitations. Most notably, the analysis is restricted to perturbations evolving about a state of zero mean flow. In realistic settings, equatorial waves interact with background shear, which is known to alter both structure and non-normal growth characteristics. Extending the present framework to include mean zonal shear on the sphere would therefore be a natural and important next step, particularly to assess how nonlinearity modifies optimal perturbations in more dynamically relevant shear flows.

In addition to that, the vertical structure and effects of bottom topography are

neglected in RSWE model considered in our study. While these simplifications allow for a clean interpretation of the underlying dynamics, they restrict the direct applicability of the results to the real atmosphere or ocean. Future work incorporating multi-layer models and realistic topography would provide important insights in this direction.

Chapter 5

Conclusion

The objective of this thesis is to explore the stability characteristics of inviscid shallow water flows on a rotating sphere, with particular emphasis on two central aspects of equatorial dynamics: the properties of individual equatorial waves in the presence of horizontal shear, and the non-normal growth of perturbations in the absence of mean flow. A comparison of tropical wave dynamics between the β-plane approximation and the full spherical geometry is made in both modal and non-modal frameworks.

The modal analysis demonstrated that the presence of equatorial mean shear predominantly alters the behaviour of slowly propagating equatorially trapped MRG and Rossby modes. Even the mean flow considered, which is confined to a narrow latitudinal band has remarkably non-local dynamical impact leading to substantial meridional spreading of perturbation energy across a wide range of zonal wavenumbers. This suggests that realistic tropical flows, where shear is ubiquitous, can provide mechanisms by which equatorial disturbances communicate with higher latitudes, potentially influencing large-scale circulation and atmospheric teleconnections. A central question addressed in the thesis concerned the limitations of the equatorial β-plane approximation. Designed as a local representation of spherical geometry near the equator, the equatorial β-plane has been widely used in theoretical studies of equatorial waves. However, even under conditions that appear ideal for its application, namely, the confinement of the mean flow to the equatorial region, the β-plane approximation shows distinct shortcomings. Both in the spectrum and spatial structures of eigenmodes, considerable discrepancies emerge between the β-plane and spherical systems. In the weak-shear regime, the waves most influenced by the background flow are the mixed Rossby-gravity (MRG) and Rossby modes. These waves respond sensitively to the directional nature of the shear: in equatorial

easterlies, they propagate faster and become more meridionally confined, whereas in westerlies they slow down and expand in meridional extent. The comparison between β-plane and spherical geometries further reveals that the β-plane tends to overestimate equatorial trapping at small wavenumbers and underestimate it at larger ones. This difference becomes especially pronounced at high wavenumbers. Under easterlies (EE), the high-wavenumber modes approach a non-dispersive limit with a phase speed below that of the Kelvin mode. Under westerlies (EW), at high-wavenumber, the phase speed of modes with successive meridional number becomes indistinguishable. Additionally, equatorially centred vortices undergo a clear splitting into off-equatorial structures at large wavenumbers. This feature may serve as an observational indicator of mesoscale Rossby waves in westerly mean flows. In the strong-shear regime, the β-plane system develops unstable modes, with growth rates highest for synoptic-scale disturbances (wavelengths around 2500 km), whereas the spherical system remains neutrally stable. The additional branches appear at small to intermediate zonal wavenumbers, corresponding to synoptic to planetary horizontal scales (a few thousand to 10000 km). At such large lengthscales, a local approximation such as β-plane approximation is likely to inaccurately represent the dynamics on the sphere. Consequently, the additional branches are likely artefacts of the β-plane approximation rather than robust physical instabilities, and their presence cautions against the use of β-plane models in strong-shear environments. Taken together, the modal analysis illustrates the combined influence of geometry and shear on the stability and structural characteristics of equatorial waves.

The second part of the thesis, concerning non-modal analysis investigated the capacity for transient amplification arising from non-normality of the governing linear operator. In the absence of mean shear flow, the β-plane operator is normal, precluding the possibility of transient growth. However, under the same configuration, the governing operator on the sphere is non-normal. The degree of non-normality depends on the Lamb parameter, which is shown to provide an upper bound to the observed non-normal growth. At high zonal wavenumbers, perturbations constructed from only two counter-propagating eigenmodes are sufficient to generate substantial amplification. In the resulting perturbations, an initially weak geopotential component undergoes strong amplification during the evolution, leading to significant non-normal growth. At intermediate and low wavenumbers, transient

growth requires the constructive participation of more than two modes, yielding richer structures.

A preliminary nonlinear analysis is done towards the end of the thesis, which studies the evolution for a few perturbations identified in the linear non-normal analysis. Nonlinear evolution of optimal initial conditions show that even weak finite amplitudes alter the linear dynamics, accelerating geopotential growth and enhancing meridional spreading. With increasing amplitude, nonlinear interactions reduce the maximum attainable growth and reorganise the flow into persistent, meridionally elongated equatorial vortices with distorted and asymmetric geopotential fields. These results confirm that geometric non-normality provides an effective linear amplification mechanism, whose magnitude, structure, and temporal persistence is ultimately regulated by the nonlinear processes.

The results obtained in the thesis collectively highlight the importance of spherical geometry in the study of equatorial flows, the significant effects of horizontal shear on wave characteristics, and the role of non-normality as a mechanism for transient amplification of the perturbations in the absence of instability.

5.1 Limitations and Future directions

Several limitations of the study in this thesis warrant discussion:

- **Shallow water approximation:** The modelling framework adopted here represents the atmosphere as a single layer, thereby neglecting the vertical structure of the atmosphere. Vertical stratification and shear are central to baroclinic instability, which cannot be captured in the current framework.
- **Idealised physical setting:** The dry shallow water framework omits key physical process such as moist convection. Further, the current study does not account for several processes that are central to atmospheric dynamics, such as thermal forcing, dissipative effects, and interactions with topography.
- **Role of background shear in non-normal growth:** The current study, in the estimation of non-normal effects, is confined to configurations lacking a background velocity field, leaving open the question of how the presence of shear alters non-normal amplification of perturbations.

- Role of baroclinic instability: Baroclinic instability is traditionally invoked as a primary mechanism for the growth of large-scale atmospheric disturbances. Dynamically the classification of flows between barotropic or baroclinic is attributed to thermal wind balance, which links vertical shear of the zonal wind to horizontal temperature gradients. Owing to strong meridional temperature gradients, the balance works remarkably well in midlatitude. However, the assumptions underlying thermal wind balance are less robust in the equatorial region. This raises questions about the extent to which baroclinic processes can act as an effective energy source for the growth of equatorial disturbances. Understanding the mechanisms that supply energy to such perturbations needs to be explored.

Appendix A

Eigenvalue analysis - Numerical Method and Validation

In this section, we discuss the numerical method employed to obtain the eigenvalues and eigenfunctions in chapter 2. Equations (2.12) and (2.15) are solved numerically using a Chebyshev collocation method. The general method has been extensively validated and used in several contexts (see e.g. [81, 89]). Our starting point is the set of $N+1$ Chebyshev collocation points $\xi_j \in [-1, 1]$:

$$\xi_j = \cos\frac{j\pi}{N},\ j = 0,\ 1,\ \cdots,\ (N-1),\ N. \tag{A.1}$$

Differentiation matrices, which give derivatives of functions defined on these collocation points in discrete form are well-known [90, 91]. The Chebyshev grid $\xi \in [-1, 1]$ is mapped appropriately to the domains of interest in the β-plane $y \in (-\infty, \infty)$ and in spherical coordinates $\theta \in [-\pi/2, \pi/2]$, in such a way that the grid is clustered to provide a higher density of grid points in regions of large variations.

In the β-plane, the algebraic mapping

$$y = \frac{\alpha\xi}{\sqrt{1-\xi^2}}. \tag{A.2}$$

is used to transform the domain of interest (y) to the Chebyshev grid (ξ). In general logarithmic or exponential maps could also be used [92]. Under this transformation, the derivative with respect to y is given as:

$$\frac{\mathrm{d}}{\mathrm{d}y} = \frac{(1-\xi^2)^{3/2}}{\alpha}\frac{\mathrm{d}}{\mathrm{d}\xi}. \tag{A.3}$$

We use the above to pre-multiply the Chebyshev differentiation matrix appropriately

to obtain the discrete differentiation matrix in y. For every value of α, the points $\xi = \pm 1$ are mapped to $y \to \pm\infty$. For low values of α ($\sim$0.1), the number of points in y are insufficient in the far-field. On the other hand, for larger values of α ($\sim$20), the grid is poorly resolved in the vicinity of the equator. For all our calculations, we use $\alpha = 1$; we have verified that the results do not change when α is changed to 0.8 or 2.

For the spherical system, the Chebyshev grid (ξ) is first stretched and then scaled by a factor of $\pi/2$, such that the two grids are related as [93, 94]:

$$\theta = \frac{a\pi}{\sinh(by_0)}\left[\sinh b\left(\frac{\xi+1}{2} - y_0\right) + \sinh(by_0)\right] - \frac{\pi}{2}, \tag{A.4}$$

$$\text{where } y_0 = \frac{1}{2b}\log\frac{1 + a\left(\mathrm{e}^{b} - 1\right)}{1 + a\left(\mathrm{e}^{-b} - 1\right)}. \tag{A.5}$$

In the above, $\pi(2a-1)/2$ is the location where the grid points are concentrated and b is a stretching parameter. Given that our interest primarily lies in the region about the equator, we select $a = 0.5$. In this study, we have varied b between 4 and 8 and ensured that the results do not change. For the results shown below, we use $b = 8$. We now have

$$\frac{\mathrm{d}}{\mathrm{d}\theta} = \frac{2}{\pi a b}\sinh(by_0)\, b\left(\frac{\xi+1}{2} - y_0\right)\frac{\mathrm{d}}{\mathrm{d}\xi}. \tag{A.6}$$

Using these matrices, the operators $\mathbf{M_s}$ and $\mathbf{M}_\beta$ in equations (2.12) and (2.15), respectively, are discretized, and the resulting matrix eigenvalue problem is solved using the `eig` function in MATLAB to obtain its eigenvalues and eigenfunctions. However, although the number of eigenvalues obtained equals the number of collocation points, not all the associated eigenfunctions are smooth; many of them correspond to spurious modes. To extract the physically meaningful, non-spurious eigenfunctions, a filtering procedure is applied as follows. Two sets of collocation points, N_1 and N_2, are chosen, and the eigenvalues obtained from both resolutions are compared. The eigenvalues that are closest to each other between the two sets are identified. Among these matched values, the corresponding eigenfunctions are further filtered based on the number of sign changes—only those with sign changes less than a specified threshold are retained as the true, smooth eigenfunctions.

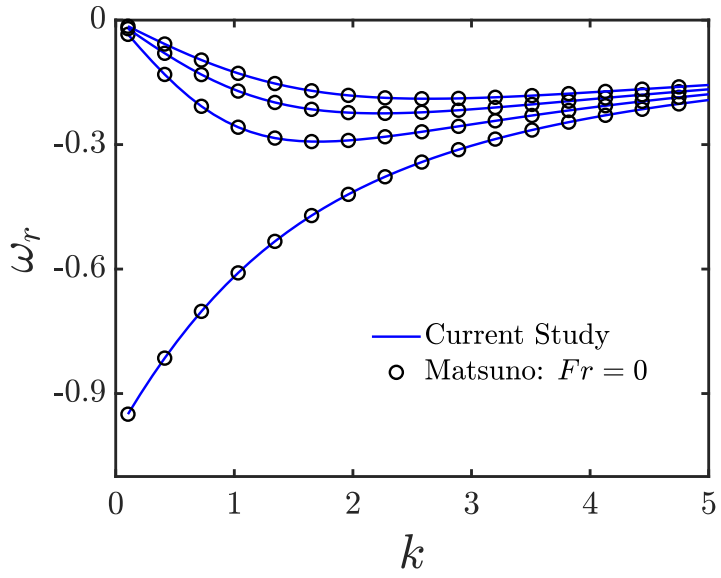

Figure A.1: Non-dimensional numerical dispersion curves for MRG and a first few Rossby modes in the absence of shear flow compared with the analytical relation from Matsuno [8]

For both the systems, we select $N = 200$. We have verified that the eigenvalues match to ten significant digits upon changing N to 300. Additionally, we have subjected the code to rigorous validation, which has achieved remarkable accuracy as a result of our prescription of the stretched grid. Under the β-plane in the absence of shear, we are able to reproduce the theoretical results of Matsuno [8] quite accurately. The comparison of eigenfrequencies shown in figure A.1 highlights the robustness of the method. In the presence of shear, we validate our numerical approach for the β-plane by reproducing the spectrum of the Rossby modes in Zhang & Webster [37, Figure 14] as shown in figure A.2. As a validation of our numerical approach in spherical coordinates, the growth rates as a function of H_0 for $k = 1$ as reported in [46] (Figure 5 therein) were recovered as shown in figure A.3.

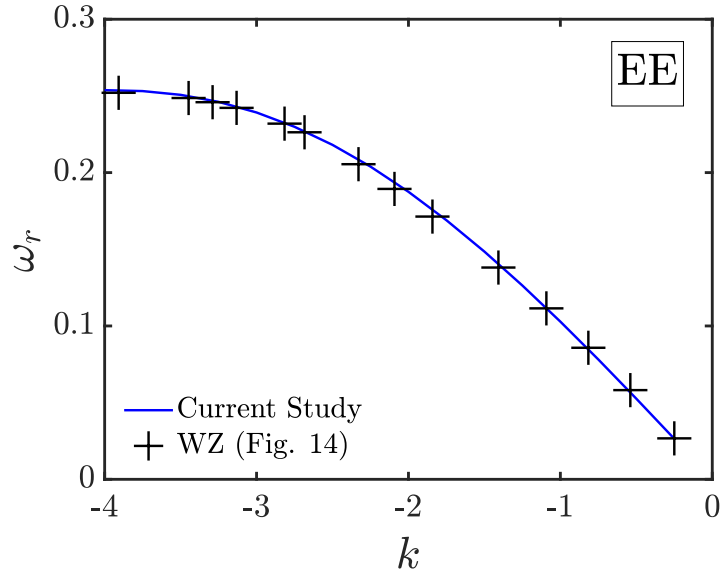

Figure A.2: Numerical dispersion curves for $n = 1$ Rossby modes in the presence of EE mean flow compared with Zhang & Webster [37, Figure 14]

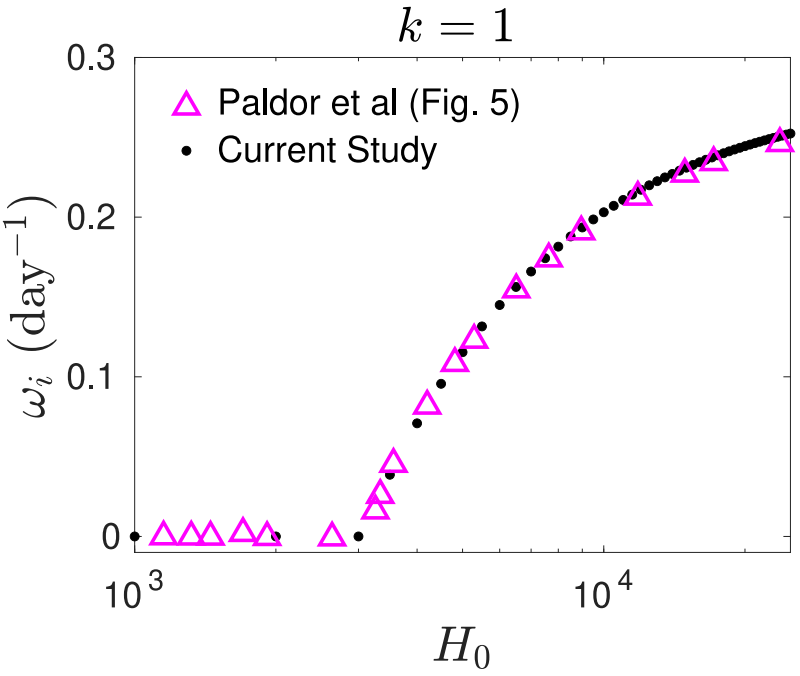

Figure A.3: Growth rates for equatorial jet in spherical system compared with Paldor *et al.* [46, Figure 5]

Appendix B

Perturbation zonal velocity and geopotential

Using the eigenvalue problems defined by equations 2.12 and 2.15 as a starting point, it is possible to obtain expressions for any component of the eigenvector in terms of another component. In this work, the meridional velocity of the mode is employed to identify its family. Here we provide expressions for the zonal perturbation velocity and the perturbation height in terms of the meridional perturbation velocity.

B.0.1 Spherical coordinate system

From equation 2.12, we get:

$$\tilde{u}_s = i\mathcal{S}_{uv}\tilde{v}_s + i\mathcal{S}_{uDv}D_y\tilde{v}_s,\ \ \tilde{h}_s = i\mathcal{S}_{hv}\tilde{v}_s + i\mathcal{S}_{hDv}D_y\tilde{v}_s \tag{B.1}$$

where

$$\mathcal{S}_{uv} = \frac{\epsilon\hat{\omega}_s\Omega_{as}\cos\theta - kD_\theta\left(\mathcal{H}_s\cos\theta\right)}{\epsilon\hat{\omega}_s^2 - k^2\mathcal{H}_s}\ , \tag{B.2a}$$

$$\mathcal{S}_{uDv} = -\frac{k\mathcal{H}_s\cos\theta}{\epsilon\hat{\omega}_s^2 - k^2\mathcal{H}_s}\ , \tag{B.2b}$$

$$\mathcal{S}_{hv} = \frac{\epsilon\left[k\mathcal{H}_s\Omega_{as}\cos\theta - \hat{\omega}_s D_\theta\left(\mathcal{H}_s\cos\theta\right)\right]}{\epsilon\hat{\omega}_s^2 - k^2\mathcal{H}_s}\ , \tag{B.2c}$$

$$\mathcal{S}_{hDv} = -\frac{\epsilon\hat{\omega}_s\mathcal{H}_s\cos\theta}{\epsilon\hat{\omega}_s^2 - k^2\mathcal{H}_s}\ . \tag{B.2d}$$

In the above expressions, $\hat{\omega}_s = \omega_s\cos\theta - kU_s$.

B.0.2 β-plane system

From equation 2.15, we get:

$$\tilde{u}_\beta = i\mathcal{B}_{uv}\tilde{v}_\beta + i\mathcal{B}_{uDv}D_y\tilde{v}_\beta,\ \tilde{h}_\beta = i\mathcal{B}_{hv}\tilde{v}_\beta + i\mathcal{B}_{hDv}D_y\tilde{v}_\beta, \tag{B.3}$$

where

$$\mathcal{B}_{uv} = \frac{k_\beta y U_\beta + (\omega_\beta - k_\beta U_\beta)(y - D_y U_\beta)}{(\omega_\beta - k_\beta U_\beta)^2 - k_\beta^2 \mathcal{H}_\beta}\ , \tag{B.4a}$$

$$\mathcal{B}_{uDv} = -\frac{k_\beta \mathcal{H}_\beta}{(\omega_\beta - k_\beta U_\beta)^2 - k_\beta^2 \mathcal{H}_\beta}\ , \tag{B.4b}$$

$$\mathcal{B}_{hv} = \frac{y U_\beta (\omega_\beta - k_\beta U_\beta) + k_\beta \mathcal{H}_\beta (y - D_y U_\beta)}{(\omega_\beta - k_\beta U_\beta)^2 - k_\beta^2 \mathcal{H}_\beta}\ , \tag{B.4c}$$

$$\mathcal{B}_{hDv} = -\frac{\mathcal{H}_\beta (\omega_\beta - k_\beta U_\beta)}{(\omega_\beta - k_\beta U_\beta)^2 - k_\beta^2 \mathcal{H}_\beta}\ . \tag{B.4d}$$

When $U_\beta = 0$ (and hence $\mathcal{H}_\beta = 1$), the expressions for $\tilde{u}_\beta$ and $\tilde{h}_\beta$ reduce to those given in [1, section 8.2].

Appendix C

Nonlinear analysis - Numerical Method and Validation

The nonlinear RSWE are solved on the sphere in vorticity-divergence formulation, which accounts for the evolution of the relative vorticity (ζ), horizontal divergence (δ), and free-surface height anomaly (h). Under this formulation, eq. (2.1) in the coordinate independent form (without the terms in box) can be expressed as,

$$\frac{\partial \zeta}{\partial t} + \nabla\cdot\left[(\zeta + f)\,\mathbf{u}\right] = \boxed{-\nu(\nabla^2)^p\zeta}, \tag{C.1}$$

$$\frac{\partial \delta}{\partial t} = -\nabla\cdot\left[\mathbf{k}\times\left[(\zeta + f)\,\mathbf{u}\right]\right] - \nabla^2\left(\frac{u^2+v^2}{2} + gh\right)\boxed{-\nu(\nabla^2)^p\delta}, \tag{C.2}$$

$$\frac{\partial h}{\partial t} + \nabla\cdot(h\,\mathbf{u}) = \boxed{-\nu(\nabla^2)^p}. \tag{C.3}$$

$$\text{where, } \zeta = \mathbf{k}\cdot(\nabla\times\mathbf{u}), \qquad \delta = \nabla\cdot\mathbf{u}, \qquad \mathbf{u} = (u, v). \tag{C.4}$$

$\mathbf{k}$ denotes the unit vector in the direction normal to the surface. The boxed terms above denote numerical damping which is introduced for numerical stability of the code. It should be noted that in the above, p is even. In the simulations, eighth-order hyperviscosity ($p = 4$) is applied in spectral space where numerical viscosity ($\nu = 10^{-5}$) controls the strength of dissipation at the smallest resolved scales. The fields are expanded in spherical harmonics basis ($Y_{\ell m}$) [95] as,

$$f(\theta,\phi,t) = \sum_{\ell=0}^{\ell_{\max}}\sum_{m=-\ell}^{\ell}\hat{f}_{\ell m}(t)\,Y_{\ell m}(\theta,\phi). \tag{C.5}$$

All the spherical harmonic transforms are performed using the SHTns library, which is a highly optimized library in python designed for efficient forward and inverse

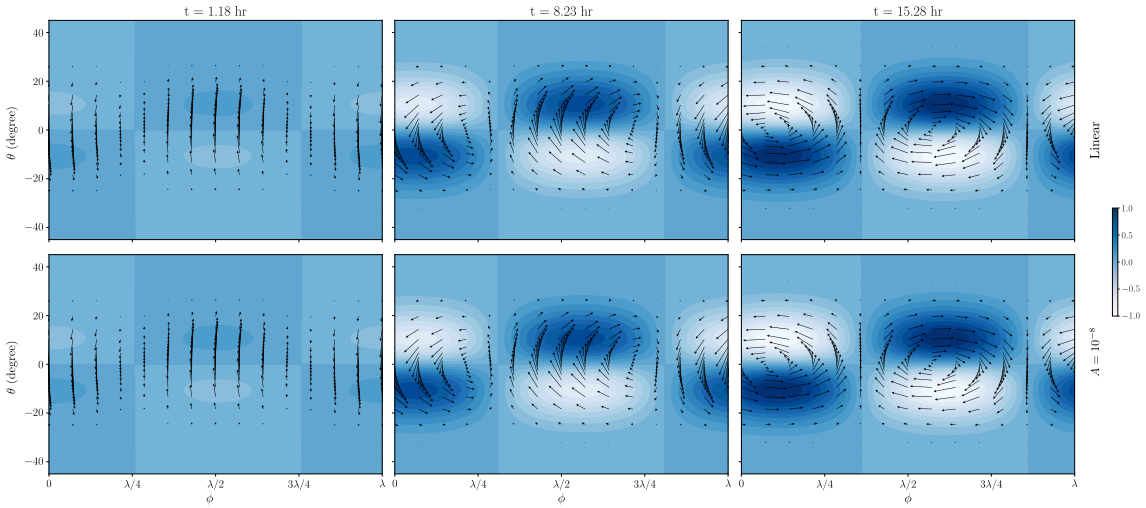

Figure C.1: snapshots of R_1-E_1 pair (top left panel in fig. 3.4) at different times for linear and low amplitude ($A = 10^{-8}$) nonlinear case. Arrows depict the velocity and colour contours depict the surface elevation. The height field in both the linear and nonlinear setting is scaled by its maximum value during the evolution.

spherical harmonic transforms, particularly suited to pseudospectral simulations on the sphere [96]. It provides exact spectral representations of gradient, divergence, curl, and Laplacian operators using analytical properties of spherical harmonics. In particular, since the spherical harmonics ($Y_{\ell m}$) are the eigenfunctions of Laplacian on sphere, the Laplacian is evaluated analytically in spectral space as

$$\nabla^2 Y_{\ell m} = -\ell(\ell+1) Y_{\ell m}, \tag{C.6}$$

Upon expanding the fields in spherical harmonics and dealing with nonlinear term appropriately, the governing nonlinear equations reduce to a system of ordinary differential equations for the spherical harmonic coefficients. For the simulations, zonal resolution is chosen to be $n_{lons} = 512$, where n_{lons} are number of grid points in ϕ coordinate. To control aliasing errors, we adopt the standard 2/3-rule and choose $\ell_{\max}$ to be the nearest integer to $n_{lons}/3$, i.e., $n_{lons} = 170$ [90]. The number of grid points in θ (n_{lats}) is chosen to be $n_{lats} = 384$, such that it satisfies $n_{lats} \geq 2\ell_{\max} + 1$, demanded by Gauss-Legendre quadrature [92]. Time stepping of the spectral coefficients is performed by initialising using forward Euler scheme followed by second and third order Adams-Bashforth scheme [97].

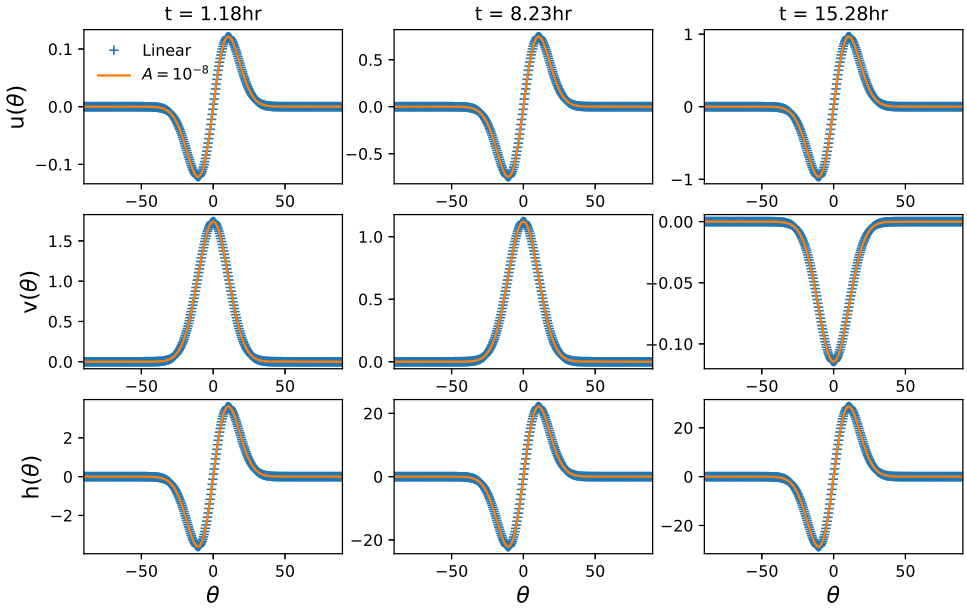

Figure C.2: snapshots of zonal,meridional velocity and geoptential of R_1-E_1 pair as a function of latitude at the times shown in figure C.1 for linear and low amplitude ($A = 10^{-8}$) nonlinear case.

The code is validated for both low and intermediate value of amplitude(A). For low A, the evolution in nonlinear system is expected to agree well with that in linear system. The fields in the linear regime are obtained by the SVD approach. It yields coefficients to construct optimal perturbations, whose evolution is governed by the linearised operator($\mathbf{M}$). To analyse the deviation between linear and nonlinear regime, we compute $f_{lin}(\theta, \phi, t)$ using the linear code which is compared to the nonlinear evolution ($f_{nl}(\theta, \phi, t)$) using the nonlinear code described above. Figure C.1 shows the structure of R_1-E_1 in the linear and low amplitude ($A = 10^{-8}$) nonlinear regime at different times, showing a good agreement between the two systems. At the longitude where geopotential achives its maximum value in each panel, the zonal and meridional velocity with geopotential is plotted as a function of latitude, which is shown in figure C.2 to have good agreement between linear and weakly nonlinear regime. To quantify the comparison, the percentage relative difference is

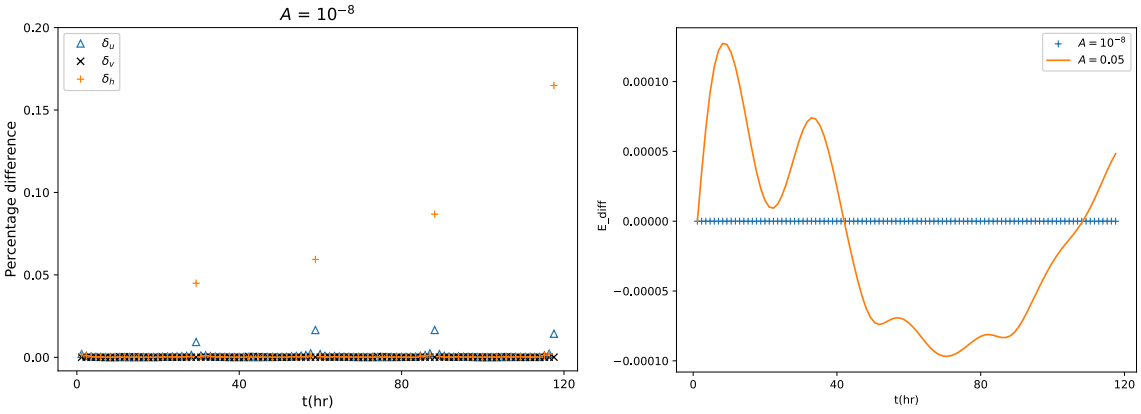

Figure C.3: left: Percentage difference between linear and nonlinear fields (δ_q) as a function of time for initial condition costructed from R_1-E_1 pair (top left panel in fig. 3.4) right: relative change in physical energy with respect to the initial value as a function of time for $A = 10^{-8}$ and $A = 0.05$.

calculated at each time, given by,

$$\delta_f(t) = 100 \times \frac{\max_{\theta,\phi}(|f_{nl} - f_{lin}|)}{\max_{\theta,\phi}(|f_{lin}|} \tag{C.7}$$

Figure C.3 (left panel) shows that the deviation in u, v and h between the linear and nonlinear evolution for $A = 10^{-8}$ are less than 1%. To further validate the code, it should be noted that the total energy density integrated over the domain (E) is conserved in nonlinear RSWE [1], such that,

$$\frac{\mathrm{d}E}{\mathrm{dt}} = \frac{1}{2}\frac{\mathrm{d}}{\mathrm{dt}}\int_A (h(u^2 + v^2) + gh^2) = 0 \tag{C.8}$$

Figure C.3(right panel) shows the relative change in physical energy with respect to its initial value,

$$\mathrm{E\_diff} = \frac{E(t) - E(0)}{E(0))}$$

for the same initial condition for $A = 10^{-8}$ and $A = 0.05$. The relative changes are negligible, such that energy changes by less than 0.1% from its initial value for $A = 0.05$. This highlights that code performs well both in the weak as well as moderate nonlinear regime.

Bibliography

1. Vallis, G. K. *Atmospheric and Oceanic Fluid Dynamics: Fundamentals and Large-Scale Circulation* doi:10.1017/9781107588417 (Cambridge University Press, Cambridge, UK, 2017).
2. Holton, J. R. & Hakim, G. J. *An introduction to dynamic meteorology* (Academic press, 2013).
3. Lorenz, E. N. in *Universality in Chaos, 2nd edition* 367–378 (Routledge, 2017).
4. Palmer, T. N. Predicting uncertainty in forecasts of weather and climate. *Reports on progress in Physics* **63,** 71 (2000).
5. Zhang, C. Madden-julian oscillation. *Reviews of Geophysics* **43** (2005).
6. Hoskins, B. J. & Karoly, D. J. The steady linear response of a spherical atmosphere to thermal and orographic forcing. *Journal of Atmospheric Sciences* **38,** 1179–1196 (1981).
7. McPhaden, M. J., Zebiak, S. E. & Glantz, M. H. ENSO as an integrating concept in earth science. *science* **314,** 1740–1745 (2006).
8. Matsuno, T. Quasi-Geostrophic Motions in the Equatorial Area. *J. Meteorol. Soc. Jpn.* **44,** 25–43. doi:10.2151/jmsj1965.44.1_25 (1966).
9. Gill, A. E. Some simple solutions for heat-induced tropical circulation. *Quarterly Journal of the Royal Meteorological Society* **106,** 447–462 (1980).
10. Lindzen, R. D. Planetary waves on beta-planes. *Monthly Weather Review* **95,** 441–451 (1967).
11. Yanai, M. & Maruyama, T. Stratospheric Wave Disturbances Propagating over the Equatorial Pacific. *J. Meteorol. Soc. Jpn.* **44,** 291–294. doi:10.2151/jmsj1965.44.5_291 (1966).

12. Lindzen, R. S. & Holton, J. R. A Theory of the Quasi-Biennial Oscillation. *J. Atmos. Sci.* **25,** 1095–1107. doi:10.1175/1520-0469(1968)025<1095:ATOTQB>2.0.CO;2 (1968).

13. Wallace, J. M. & Kousky, V. Observational Evidence of Kelvin Waves in the Tropical Stratosphere. *J. Atmos. Sci.* **25,** 900–907. doi:10.1175/1520-0469(1968)025<0900:OEOKWI>2.0.CO;2 (1968).

14. Takayabu, Y. N. Large-Scale Cloud Disturbances Associated with Equatorial Waves Part I: Spectral Features of the Cloud Disturbances. *J. Meteorol. Soc. Jpn.* **72,** 433–449. doi:10.2151/jmsj1965.72.3_433 (1994).

15. Takayabu, Y. N. Large-scale cloud disturbances associated with equatorial waves Part II: Westward-propagating inertio-gravity waves. *J. Meteorol. Soc. Jpn.* **72,** 451–465. doi:10.2151/jmsj1965.72.3_433 (1994).

16. Holton, J. R. & Lindzen, R. S. A note on "Kelvin" waves in the atmosphere. *Mon. Weather Rev.* **96,** 385–386. doi:10.1175/1520-0493(1968)096<0385:ANOKWI>2.0.CO;2 (1968).

17. Boyd, J. P. *Dynamics of the Equatorial Ocean* doi:10.1007/978-3-662-55476-0 (Springer, Berlin, Germany, 2018).

18. Wallace, J. M. General circulation of the tropical lower stratosphere. *Rev. Geophys.* **11,** 191–222. doi:10.1029/RG011i002p00191 (1973).

19. Wheeler, M. & Kiladis, G. N. Convectively Coupled Equatorial Waves: Analysis of Clouds and Temperature in the Wavenumber-Frequency Domain. *J. Atmos. Sci.* **56,** 374–399. doi:10.1175/1520-0469(1999)056<0374:CCEWAO>2.0.CO;2 (1999).

20. Wang, B. & Xie, X. Low-frequency equatorial waves in vertically sheared zonal flow. Part I: Stable waves. *Journal of the Atmospheric Sciences* **53,** 449–467 (1996).

21. Han, Y. & Khouider, B. Convectively coupled waves in a sheared environment. *J. Atmos. Sci.* **67,** 2913–2942. doi:10.1175/2010JAS3335.1 (2010).

22. Zhang, C. & Webster, P. J. Laterally forced equatorial perturbations in a linear model. Part I: Stationary transient forcing. *Journal of Atmospheric Sciences* **49,** 585–607 (1992).

23. Hoskins, B. J. & Yang, G.-Y. The longitudinal variation of equatorial waves due to propagation on a varying zonal flow. *Journal of the Atmospheric Sciences* **73,** 605–620 (2016).

24. Yang, G.-Y. & Hoskins, B. J. ENSO-related variation of equatorial MRG and Rossby waves and forcing from higher latitudes. *Quarterly Journal of the Royal Meteorological Society* **142,** 2488–2504 (2016).

25. Mahó, S. I., Vasylkevych, S. & Žagar, N. Excitation of mixed Rossby–gravity waves by wave–mean flow interactions on the sphere. *Quarterly Journal of the Royal Meteorological Society* **150,** 2920–2936 (2024).

26. Mahó, S., Žagar, N., Lunkeit, F. & Vasylkevych, S. The mechanism of scale selection for mixed Rossby-gravity waves in the upper troposphere and the upper stratosphere. *Geophysical Research Letters* **51,** e2024GL110811 (2024).

27. Andrews, D. & Mcintyre, M. E. Planetary waves in horizontal and vertical shear: The generalized Eliassen-Palm relation and the mean zonal acceleration. *Journal of Atmospheric Sciences* **33,** 2031–2048 (1976).

28. Yang, G.-Y., Hoskins, B. & Slingo, J. Convectively Coupled Equatorial Waves: A New Methodology for Identifying Wave Structures in Observational Data. *J. Atmos. Sci.* **60,** 1637–1654. doi:10.1175/1520-0469(2003)060<1637:CCEWAN>2.0.CO;2 (2003).

29. Booker, J. R. & Bretherton, F. P. The critical layer for internal gravity waves in a shear flow. *Journal of fluid mechanics* **27,** 513–539 (1967).

30. Webster, P. J. & Chang, H.-R. Equatorial Energy Accumulation and Emanation Regions: Impacts of a Zonally Varying Basic State. *J. Atmos. Sci.* **45,** 803–829. doi:10.1175/1520-0469(1988)045<0803:EEAAER>2.0.CO;2 (1988).

31. Ripa, P. Nonlinear wave–wave interactions in a one-layer reduced-gravity model on the equatorial β plane. *Journal of Physical Oceanography* **12,** 97–111 (1982).

32. Boyd, J. P. The effects of latitudinal shear on equatorial waves. Part II: Applications to the atmosphere. *Journal of Atmospheric Sciences* **35,** 2259–2267 (1978).

33. Saravanan, R. Equatorial superrotation and maintenance of the general circulation in two-level models. *Journal of Atmospheric Sciences* **50,** 1211–1227 (1993).

34. Holton, J. R. The influence of mean wind shear on the propagation of Kelvin waves. *Tellus* **22,** 186–193 (1970).

35. Hoskins, B. The role of potential vorticity in symmetric stability and instability. *Quarterly Journal of the Royal Meteorological Society* **100,** 480–482 (1974).

36. Pedlosky, J. An inertial theory of the equatorial undercurrent. *Journal of physical oceanography* **17,** 1978–1985 (1987).

37. Zhang, C. & Webster, P. J. Effects of Zonal Flows on Equatorially Trapped Waves. *J. Atmos. Sci* **46,** 3632–3652. ISSN: 0022-4928. doi:10.1175/1520-0469(1989)046<3632:EOZFOE>2.0.CO;2 (Dec. 1989).

38. Hough, S. S. V. On the application of harmonic analysis to the dynamical theory of the tides.—Part II. On the general integration of Laplace's dynamical equations. *Phil. Trans. R. Soc. A* **191,** 139–185. doi:10.1098/rsta.1898.0005 (1898).

39. Longuet-Higgins, M. S. The eigenfunctions of Laplace's tidal equation over a sphere. *Phil. Trans. R. Soc. A* **262,** 511–607. ISSN: 0080-4614. doi:10.1098/rsta.1968.0003 (1968).

40. Kasahara, A. Numerical integration of the global barotropic primitive equations with Hough harmonic expansions. *Journal of Atmospheric Sciences* **34,** 687–701 (1977).

41. Kasahara, A. & Puri, K. Spectral representation of three-dimensional global data by expansion in normal mode functions. *Monthly Weather Review* **109,** 37–51 (1981).

42. Castanheira, J. M. & Marques, C. A. Convectively coupled equatorial-wave diagnosis using three-dimensional normal modes. *Quarterly Journal of the Royal Meteorological Society* **141,** 2776–2792 (2015).

43. Žagar, N., Kasahara, A., Terasaki, K., Tribbia, J. & Tanaka, H. Normal-mode function representation of global 3-D data sets: Open-access software for the atmospheric research community. *Geoscientific Model Development* **8,** 1169–1195 (2015).

44. Paldor, N., Fouxon, I., Shamir, O. & Garfinkel, C. I. The mixed Rossby–gravity wave on the spherical Earth. *Q. J. Roy. Meteor. Soc.* **144,** 1820–1830. doi:10.1002/qj.3354 (2018).

45. Garfinkel, C. I., Fouxon, I., Shamir, O. & Paldor, N. Classification of eastward propagating waves on the spherical Earth. *Q. J. Roy. Meteor. Soc.* **143,** 1554–1564. doi:10.1002/qj.3025 (2017).

46. Paldor, N., Shamir, O. & Garfinkel, C. I. Barotropic instability of a zonal jet on the sphere: from non-divergence through quasi-geostrophy to shallow water. *Geophys. Astrophys. Fluid Dynam.* **115,** 15–34. doi:10.1080/03091929.2020.1724996 (2021).

47. Farrell, B. F. Optimal excitation of perturbations in viscous shear flow. *Physics of Fluids* **31,** 2093 (1988).

48. Trefethen, L. N., Trefethen, A. E., Reddy, S. C. & Driscoll, T. A. Hydrodynamic stability without eigenvalues. *Science* **261,** 578–584 (1993).

49. Farrell, B. F. & Ioannou, P. J. Generalized stability theory. Part I: Autonomous operators. *Journal of Atmospheric Sciences* **53,** 2025–2040 (1996).

50. Diaconescu, E. P. & Laprise, R. Singular vectors in atmospheric sciences: A review. *Earth-Sci. Rev.* **113,** 161–175. doi:10.1016/j.earscirev.2012.05.005 (2012).

51. Farrell, B. Modal and Non-Modal Baroclinic Waves. *J. Atmos. Sci.* **41,** 668–673. doi:10.1175/1520-0469(1984)041<0668:MANMBW>2.0.CO;2 (1984).

52. Farrell, B. Transient Growth of Damped Baroclinic Waves. *J. Atmos. Sci.* **42,** 2718–2727. doi:10.1175/1520-0469(1985)042<2718:TGODBW>2.0.CO;2 (1985).

53. Raghav, M. S., Jose, S., Apte, A. & Govindarajan, R. Effects of equatorially-confined shear flow on MRG and Rossby waves. *Dynam. Atmos. Oceans* **100,** 101331. doi:10.1016/j.dynatmoce.2022.101331 (2022). Corrigendum to "Effects of equatorially-confined shear flow on MRG and Rossby waves" [Dyn. Atmos. Oceans 100 (2022) 101331]. *Dynam. Atmos. Oceans,* 101499. doi:10.1016/j.dynatmoce.2024.101499 (2024).

54. Raghav, M. S., Jose, S., Apte, A. & Govindarajan, R. Corrigendum to "Effects of equatorially-confined shear flow on MRG and Rossby waves" [Dyn. Atmos. Oceans 100 (2022) 101331]. *Dynam. Atmos. Oceans,* 101499. doi:10.1016/j.dynatmoce.2024.101499 (2024).

55. Kiladis, G. N., Wheeler, M. C., Haertel, P. T., Straub, K. H. & Roundy, P. E. Convectively coupled equatorial waves. *Rev. Geophys.* **47.** doi:10.1029/2008RG000266 (2009).

56. Lindzen, R. S. & Matsuno, T. On the nature of large scale wave disturbances in the equatorial lower stratosphere. *Journal of the Meteorological Society of Japan. Ser. II* **46,** 215–220 (1968).

57. Cho, H.-K., Bowman, K. P. & North, G. R. Equatorial Waves Including the Madden–Julian Oscillation in TRMM Rainfall and OLR Data. *J. Clim.* **17,** 4387–4406. doi:10.1175/3215.1 (2004).

58. Dias, J. & Kiladis, G. N. Influence of the basic state zonal flow on convectively coupled equatorial waves. *Geophys. Res. Lett.* **41,** 6904–6913. doi:10.1002/2014GL061476 (2014).

59. Bühler, O. *Waves and Mean Flows* doi:10.1017/CBO9781107478701 (Cambridge University Press, Cambridge, UK, 2014).

60. Bennett, J. R. & Young, J. A. The influence of latitudinal wind shear upon large-scale wave propagation into the tropics. *Mon. Weather Rev.* **99,** 202–214. doi:10.1175/1520-0493(1971)099<0202:TIOLWS>2.3.CO;2 (1971).

61. Fulton, S. R. & Schubert, W. H. Vertical normal mode transforms: Theory and application. *Monthly weather review* **113,** 647–658 (1985).

62. Salby, M. L. & Garcia, R. R. Transient response to localized episodic heating in the tropics. Part I: Excitation and short-time near-field behavior. *J. Atmos. Sci.* **44,** 458–498. doi:10.1175/1520-0469(1987)044<0458:TRTLEH>2.0.CO;2 (1987).

63. Gill, A. E. *Atmosphere-Ocean Dynamics* (Academic Press, San Diego, USA, 1982).

64. Clift, P. D. & Plumb, R. A. *The Asian Monsoon: Causes, History and Effects* doi:10.1017/CBO9780511535833 (Cambridge University Press, Cambridge, UK, 2008).

65. Holton, J. R. *An Introduction to Dynamic Meteorology* (Elsevier Academic Press, Oxford, UK, 2004).

66. Koornwinder, T. H., Wong, R., Koekoek, R. & Swarttouw, R. F. in *NIST Handbook of Mathematical Functions* (eds Olver, F. W. J., Lozier, D. W., Boisvert, R. F. & Clark, C. W.) 435–484 (Cambridge University Press, Cambridge, UK, 2010).

67. Killworth, P. D. Barotropic and baroclinic instability in rotating stratified fluids. *Dynamics of Atmospheres and Oceans* **4,** 143–184 (1980).

68. Charney, J. G. The dynamics of long waves in a baroclinic westerly current. *J. Meteorol.* **4,** 135–162. doi:10.1175/1520-0469(1947)004<0136:TDOLWI>2.0.CO;2 (1947).

69. Eady, E. T. Long Waves and Cyclone Waves. *Tellus* **1,** 33–52. doi:10.3402/tellusa.v1i3.8507 (1949).

70. Gill, A. E. Some simple solutions for heat-induced tropical circulation. *Q. J. R. Meteorol. Society.* **106,** 447–462. doi:10.1002/qj.49710644905 (1980).

71. Lau, K.-M. Oscillations in a Simple Equatorial Climate System. *J. Atmos. Sci.* **38,** 248–261. doi:10.1175/1520-0469(1981)038<0248:OIASEC>2.0.CO;2 (1981).

72. Lim, H. & Chang, C.-P. Dynamics of Teleconnections and Walker Circulations Forced by Equatorial Heating. *J. Atmos. Sci.* **40,** 1897–1915. doi:10.1175/1520-0469(1983)040<1897:DOTAWC>2.0.CO;2 (1983).

73. Lau, K.-M. & Lim, H. On the Dynamics of Equatorial Forcing of Climate Teleconnections. *J. Atmos. Sci.* **41,** 161–176. doi:10.1175/1520-0469(1984)041<0161:OTDOEF>2.0.CO;2 (1984).

74. Chao, W. C. On the Origin of the Tropical Intraseasonal Oscillation. *J. Atmos. Sci.* **44,** 1940–1949. doi:10.1175/1520-0469(1987)044<1940:OTOOTT>2.0.CO;2 (1987).

75. Lau, K.-M. & Peng, L. Origin of Low-Frequency (Intraseasonal) Oscillations in the Tropical Atmosphere. Part I: Basic Theory. *J. Atmos. Sci.* **44,** 950–972. doi:10.1175/1520-0469(1987)044<0950:OOLFOI>2.0.CO;2 (1987).

76. Schmid, P. J. Nonmodal stability theory. *Annu. Rev. Fluid Mech.* **39,** 129–162 (2007).

77. Orr, W. *The stability or instability of the steady motions of a perfect liquid and of a viscous liquid. Part II: A viscous liquid* in *Proceedings of the Royal Irish Academy. Section A: Mathematical and Physical Sciences* **27** (1907), 69–138.

78. Landahl, M. A note on an algebraic instability of inviscid parallel shear flows. *Journal of Fluid Mechanics* **98,** 243–251 (1980).

79. Andersson, P., Berggren, M. & Henningson, D. S. Optimal disturbances and bypass transition in boundary layers. *Physics of Fluids* **11,** 134–150 (1999).

80. Schmid, P. J. & Henningson, D. S. *Stability and Transition in Shear Flows* doi:10.1007/978-1-4613-0185-1 (Springer-Verlag, New York, 2001).

81. Jose, S., Kuzhimparampil, V., Pier, B. & Govindarajan, R. Algebraic disturbances and their consequences in rotating channel flow transition. *Phys. Rev. Fluids* **2,** 083901. doi:10.1103/PhysRevFluids.2.083901 (2017).

82. Jose, S. Regenerative Orr mechanism yielding large non-modal perturbation energy growth in a viscosity stratified plane shear flow. *Int. J. Multiph. Flow* **181,** 105001. doi:10.1016/j.ijmultiphaseflow.2024.105001 (2024).

83. Pedlosky, J. *Geophysical fluid dynamics* (Springer Science & Business Media, 2013).

84. Salmon, R. *Lectures on geophysical fluid dynamics* (Oxford University Press, 1998).

85. Holton, J. R. & Lindzen, R. S. An updated theory for the quasi-biennial cycle of the tropical stratosphere. *Journal of Atmospheric Sciences* **29,** 1076–1080 (1972).

86. Baldwin, M. P., Gray, L., Dunkerton, T., Hamilton, K., Haynes, P., Randel, W., Holton, J., Alexander, M., Hirota, I., Horinouchi, T., *et al.* The quasi-biennial oscillation. *Reviews of Geophysics* **39,** 179–229 (2001).

87. Sukhatme, J. & Smith, L. M. Local and nonlocal dispersive turbulence. *Physics of Fluids* **21** (2009).

88. O'Gorman, P. A. & Schneider, T. Recovery of atmospheric flow statistics in a general circulation model without nonlinear eddy-eddy interactions. *Geophysical Research Letters* **34** (2007).

89. Ravichandran, S., Meiburg, E. & Govindarajan, R. Mammatus cloud formation by settling and evaporation. *J. Fluid Mech.* **899.** doi:10.1017/jfm.2020.439 (2020).

90. Canuto, C., Hussaini, M. Y., Quarteroni, A. & Zang, T. A. *Spectral Methods: Fundamentals in Single Domains* doi:10.1007/978-3-540-30726-6 (Springer, Berlin, Germany, 2007).

91. Trefethen, L. N. *Spectral Methods in MATLAB* doi:10.1137/1.9780898719598 (Society for Industrial and Applied Mathematics, Philadelphia, USA, 2000).

92. Boyd, J. P. *Chebyshev and Fourier Spectral Methods* (Dover, New York, USA, 2001).

93. Vinokur, M. On one-dimensional stretching functions for finite-difference calculations. *J. Comput. Phys.* **50,** 215–234. doi:10.1016/0021-9991(83)90065-7 (1983).

94. Govindarajan, R. Effect of miscibility on the linear instability of two-fluid channel flow. *Int. J. Multiph. Flow* **30,** 1177–1192. doi:10.1016/j.ijmultiphaseflow.2004.06.006 (Oct. 2004).

95. Satoh, M. *Atmospheric circulation dynamics and general circulation models* (Springer Science & Business Media, 2013).

96. Schaeffer, N. Efficient spherical harmonic transforms aimed at pseudospectral numerical simulations. *Geochemistry, Geophysics, Geosystems* **14,** 751–758 (2013).

97. Teukolsky, S. A., Flannery, B. P., Press, W. & Vetterling, W. Numerical recipes in C. *SMR* **693,** 59–70 (1992).